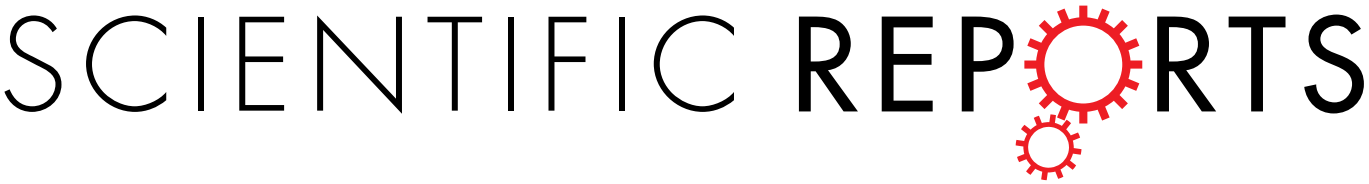

OPEN

Sedimentary record from Patagonia, southern Chile supports cosmic-impact triggering of biomass burning, climate change, and megafaunal extinctions at 12.8 ka

Received: 27 March 2018
Accepted: 19 December 2018
Published online: 13 March 2019

Mario Pino[1,2], Ana M. Abarzúa[1,2], Giselle Astorga[1,2], Alejandra Martel-Cea[1,2], Nathalie Cossio-Montecinos[1], R. Ximena Navarro[3], Maria Paz Lira[4], Rafael Labarca[1,2], Malcolm A. LeCompte[5], Victor Adedeji[6], Christopher R. Moore[7], Ted E. Bunch[8], Charles Mooney[9], Wendy S. Wolbach[10], Allen West[11] & James P. Kennett[12]

The Younger Dryas (YD) impact hypothesis posits that fragments of a large, disintegrating asteroid/comet struck North America, South America, Europe, and western Asia ~12,800 years ago. Multiple airbursts/impacts produced the YD boundary layer (YDB), depositing peak concentrations of platinum, high-temperature spherules, meltglass, and nanodiamonds, forming an isochronous datum at >50 sites across ~50 million km² of Earth's surface. This proposed event triggered extensive biomass burning, brief impact winter, YD climate change, and contributed to extinctions of late Pleistocene megafauna. In the most extensive investigation south of the equator, we report on a ~12,800-year-old sequence at Pilauco, Chile (~40°S), that exhibits peak YD boundary concentrations of platinum, gold, high-temperature iron- and chromium-rich spherules, and native iron particles rarely found in nature. A major peak in charcoal abundance marks an intense biomass-burning episode, synchronous with dramatic changes in vegetation, including a high-disturbance regime, seasonality in precipitation, and warmer conditions. This is anti-phased with northern-hemispheric cooling at the YD onset, whose rapidity suggests atmospheric linkage. The sudden disappearance of megafaunal remains and dung fungi in the YDB layer at Pilauco correlates with megafaunal extinctions across the Americas. The Pilauco record appears consistent with YDB impact evidence found at sites on four continents.

The YDB impact hypothesis posits that the hemisphere-wide debris field of a large, fragmenting asteroid/comet struck Earth and caused brief "impact winter" conditions[1–3]. In turn, this triggered major shifts in continental

[1]Instituto de Ciencias de la Tierra, Universidad Austral de Chile, Valdivia, Chile. [2]Transdiciplinary Center for Quaternary Research (TAQUACH), Universidad Austral de Chile, Valdivia, Chile. [3]Departamento de Antropología, Universidad Católica de Temuco, Temuco, Chile. [4]Laboratorio Pilauco, Universidad Austral de Chile, Valdivia, Chile. [5]Elizabeth City State University, Center of Excellence in Remote Sensing Education and Research, Elizabeth City, NC, 27909, USA. [6]Department of Natural Sciences, Elizabeth City State University, Elizabeth City, NC, 27909, USA. [7]Savannah River Archaeological Research Program, South Carolina Institute of Archaeology and Anthropology, University of South Carolina, Columbia, South Carolina, 29208, USA. [8]Geology Program, School of Earth Science and Environmental Sustainability, Northern Arizona University, Flagstaff, AZ, 86011, USA. [9]Analytical Instrumentation Facility, North Carolina State University, Raleigh, NC, 27695, USA. [10]Department of Chemistry, DePaul University, Chicago, IL, 60614, USA. [11]Comet Research Group, Prescott, AZ, 86301, USA. [12]Department of Earth Science and Marine Science Institute, University of California, Santa Barbara, CA, 93106, USA. Correspondence and requests for materials should be addressed to A.W. (email: CometResearchGroup@gmail.com)

drainage patterns, dramatically changed oceanic circulation, and caused abrupt global climate changes (temperature and precipitation) marked by the Younger Dryas (YD) climatic episode in the Northern Hemisphere[4]. The airburst/impacts are proposed to have caused significant environmental changes, including widespread biomass burning, anomalously abrupt shifts in plant and animal distributions, human cultural changes and population declines, and broad extinctions within the iconic late Pleistocene megafauna[1]. Studies of the Younger Dryas boundary (YDB) layer report peak abundances of a diverse suite of proposed cosmic impact-related proxies at more than 50 sites, located mostly within the Northern Hemisphere, but with two previous sites in the Southern Hemisphere (Venezuela[5,6] and Antarctica[7]). These include peak abundances of high-temperature high-iron (Fe) spherules, glassy silica-rich spherules, high-temperature meltglass, nanodiamonds, platinum (Pt), iridium (Ir), osmium (Os), and/or other impact-related proxies (for references, cf. Supplementary Table A2 in Wolbach *et al*.[3]). The YDB layer is also often marked by abundance peaks in biomass-burning proxies, including charcoal, aciniform carbon/soot, carbon spherules, glasslike carbon and/or combustion aerosols[1–3,8–12]. This entire suite of proxies at the YD onset is argued to represent one of the largest known biomass-burning peaks of the late Quaternary[2,3].

First proposed in 2007[1], the YDB impact hypothesis is still controversial a decade later because a number of independent studies have raised questions about the proposed YDB impact event. (1) The authors of several studies[13–15] have argued that dating accuracy and precision are insufficient to determine whether YDB proxies are coeval across the many sites. (2) Five of 13 independent studies were unable to confirm the presence of peaks in YDB magnetic spherules (see Supplementary Information, "Previously reported evidence of YDB magnetic spherules" for details). (3) Three studies[13–15] noted that sediment sampling at YDB sites is typically discontinuous, except at and around the YDB layer, where sampling spanned at most a few thousand years, making it difficult to know whether the "impact assemblage" of indicators is unique to the YDB (Supplementary Table S1). The same concern applies to this study in which we sampled continuously at high resolution for ~300 years across the YDB layer and sporadically before and after, totalling ~17,000 years. (4) In one study[13], it was argued that the proposed YDB impact mechanism of a fragmented comet is so rare as to be statistically implausible. (5) Several investigators[15–18] proposed that the rate and timing of megafaunal extinctions were not simultaneous but varied across the continents, with a large percentage of them occurring prior to the YDB. (6) Another study[19] concluded that a major peak in wildfire activity preceded the YD onset by several hundred years and did not correlate with the YD onset. (7) It was argued in several studies[13,15,18] that individual "impact indicators" are also produced by non-impact processes, thus not requiring an impact. Finally, (8) another study[16] argued that YD climate change had little effect on people and their animal prey across the central portion of the US. For a limited number of selected contributions relevant to this hypothesis, see Supplementary Table A3 of Wolbach *et al*.[3]

Proponents[1,10,20,21] of the YDB impact hypothesis concede that individual proxies might have formed through alternative processes, but argue that coeval abundance peaks for the *entire suite* of proxies in the same stratum is unique to cosmic impact events. For example, the same suite of proxies has been found in the well-known Cretaceous-Tertiary (K-T) boundary layer[22,23] (~65.5 million years ago), forming a global datum layer. Similarly, the 780,000-year-old Australasian impact event dispersed small amounts of microscopic spherules and impact glass across ~30% of the planet's surface, forming the largest known impact strewnfield[24], for which no physical crater has been found. As with the K-T and Australasian impact events, the YDB layer contains a suite of impact proxies within a datum layer that can also be used for global correlation and dating. Impact proponents argue that the YDB datum layer is precisely equivalent in age to the onset of the YD cooling episode recorded in the Greenland ice sheet and in many other stratigraphic sections in the Northern Hemisphere[4]. Regardless of differing hypotheses about the YDB suite's origin, this layer forms a valuable datum for global correlation and dating.

An important new development includes the discovery by Kjaer *et al*.[25] of a giant, 31-km-wide, possible YDB-aged impact crater under the Hiawatha Glacier in northwestern Greenland, calculated to have been produced by a 1.5-km-wide impactor. This is the 25th largest known terrestrial crater, the largest in the last ~5 million years (52-km-wide Kara-Kul crater in Tajikistan), and the second largest in the last ~35.3 million years (40-km-wide Chesapeake Bay in Virginia, USA). Impact proxies include high-temperature spherules, meltglass, amorphous carbon, and elevated concentrations of Ni, Co, Cr, PGEs (e.g., Pt, Ir, and Os), and Au[25], all of which are also elevated at YDB sites on four continents.

Kjaer *et al*.[25] conclude that the potential age range of the impact event spans the YD onset, although the crater is as yet undated. The potential for a YDB age is based on several lines of evidence: (1) Post-YDB annual ice layers are present from the Younger Dryas (12,800 to 11,700 cal BP) through the Holocene (11,700 cal BP to modern times), but undisturbed pre-YDB ice layers are missing. However, four widely distributed, distinctive, radar-reflecting, pre-YDB ice layers, including the youngest that spans the Bølling-Allerød (14,700 to 12,800 cal BP), are missing within the crater and within 100 km around it, consistent with having been disrupted by the impact event. (2) There is evidence of hydrothermal activity within the crater beneath the overlying 930-meter-thick ice sheet, as would be expected from residual heat generated by a young impact. If such activity had been caused by an impact event, it would be short-lived because the continuing melting of ice cover over the crater would efficiently dissipate the heat. Therefore, ongoing hydrothermal activity is consistent with a very young age for the crater. (3) The subglacial crater rim and basin appear relatively fresh and minimally eroded, consistent with a young crater[25]. If the crater were very old, the rim is expected to be much more subdued, due to the erosive effects of glacial ice movements, as is apparent with many once-subglacial Canadian crater rims that were flattened by movement of the Laurentide Ice Sheet. (4) Kjaer *et al*.[25] report PGE anomalies in the crater derived from an ET impact event. This is similar to the results of Petaev *et al*.[26], who analyzed Greenland ice and report an abundance peak in Pt spanning 21 years from 12,836–12,815 cal BP. They attributed this to multiple injections of Pt from a large extraterrestrial impact event, possibly now identified with the Hiawatha Crater. Kjaer *et al*.[25] conclude that such a massive impact event "very likely had significant environmental consequences in the

Northern Hemisphere and possibly globally." If so, this impact event may have triggered climate change in southern Chile, which we explore in this contribution.

The Chilean Council of National Monuments has protected the unique Pilauco site as an important paleontological and archaeological resource because of its rich and abundant assemblage of extinct South American Pleistocene mammals and cultural remains. Prior descriptions of the stratigraphy, biostratigraphy, and chronology of this well-exposed sedimentary sequence[27–34] provide the foundation for our investigations, and the high sedimentation rate offers high chronological resolution. Previous radiocarbon dating (9 dates[27]) has shown that the sequence includes the estimated age span of the YDB impact event (~12,835 to 12,735 cal BP)[35]. In this study, we conducted time series material analyses across the sedimentary sequence to determine changes in concentrations of Pt, palladium (Pd), high-temperature magnetic spherules, charcoal, plant macrofossils, pollen, and dung fungal spores (*Sporormiella* spp.). Also, the Pilauco stratigraphic sequence has provided an unprecedented opportunity to compare the regional megafaunal extinctions at high resolution with similar coeval extinctions in the Northern Hemisphere. We have also undertaken quantitative pollen and seed analyses across the boundary layer for paleoclimatic and paleo-environmental assessments and for comparison with YD climatic change as determined from sequences in the Northern Hemisphere.

The Pilauco site is the most extensively investigated YDB sequence south of the equator, but is also at high southern latitudes (~40°S) more than 6000 km farther south than the closest well-studied YDB site in Venezuela[5]. Identification of this YDB datum enables precise correlation between identical chronostratigraphic intervals in the Northern Hemisphere, including those at high latitudes.

It is important to note that the main objective of this contribution is to test the YDB hypothesis and to document and discuss the wide range of evidence found within the Pilauco sedimentary section in southern Chile (Figs 1 and 2). In this study, we sought to determine whether the evidence at Pilauco is consistent or inconsistent with the YDB impact hypothesis and to explore the potential consequences of the proposed impact event.

Section 1: Study Site

Setting. The Pilauco site is located ~40 km west of Lakes Puyehue and Rupanco[36] in southern Chile within the city of Osorno, northwestern Patagonia, at ~30 m above sea level (a.s.l.) (40°34′S, 73°06′W) (Fig. 1). The site presently lies in the northern part of the temperate zone of the Southern Hemisphere and annual precipitation derived from the prevailing westerly winds totals ~1330 mm, which occurs mainly during the austral fall and winter months. The mean annual temperature is 11.4 °C[37]. For details about Pilauco's paleoclimate and biota, see Supplementary Information, S2.

Stratigraphy and Sedimentology. The first excavations at the Pilauco site in 2007 followed the discovery there of a rich assemblage of mammalian fossils. To facilitate archaeological and paleontological investigations, the site was divided into a horizontal grid composed of 1-m^2 elements, and the vertical sedimentary sequence was subdivided into lithostratigraphic units designated PB-6 through PB-9 (Supplementary Fig. S1).

During the last interglacial (~130,000 years ago), the Osorno area experienced intense volcanic activity from the Andean arc located ~100 km to the east (Fig. 1a). This volcanic activity deposited a series of volcanoclastic flows (50-m minimum thickness) at Secuencia San Pablo[38], which form the hills north of Osorno and the lowermost unit at the Pilauco site. Consequently, all strata sampled at Pilauco contain abundant multi-cm-sized clasts of volcanic basalt and tuff.

The basal unit of the Pilauco stratigraphic sequence (PB-6) is an unconsolidated sedimentary bed containing abundant well-rounded pebbles and boulders. (For further details on Pilauco sedimentary stratigraphy, see Supplementary Information, S3, Supplementary Tables S2 and S3). The next higher unit (PB-7) is an organic-rich sand composed of isolated, poorly sorted colluvial volcanoclastics that contain most of the extinct megafauna remains and lithic artifacts. Unit PB-8 is composed of organic-rich mudstone separated by thin, muddy laminae, similar to unit PB-7, although it contains fewer mammal fossils and lithic artifacts than the unit PB-7 below it. Unit PB-8 also contains the youngest horse coprolite found at the site[28,39]. At Pilauco, the key stratigraphic feature is the PB-8/PB-9 boundary that marks major environmental and sedimentological changes, and is inferred from radiocarbon dating to be the YDB layer. Immediately above the YDB in unit PB-9 there is a large accumulation of wood fragments, frequently found along an undulating contact that defines a sharp lithological change (Supplementary Figs S2, S3, S4 and S5). Overall, unit PB-9 is a relatively fine-grained, black, organic-rich peat.

The charcoal-rich, peaty matrix of unit PB-9 is argued to be analogous to the "black mat" found at ~30% of the 12,800-year-old YDB sites on four continents[1,3]. The term "black mat" applies to dark, organic-rich deposits, as well as to some marls and diatomites that are white or gray, rather than black[40]. Haynes[40] concluded that these mats are complex pedological features derived from two major processes: first, from deposition of organic-rich material, e.g., as in wetlands (29 of the 70 sites)[40–42], and second, from soil formation possibly due to weathering of stable, organic-rich landscapes (41 of the 70 sites; see Table 2 of Haynes[40]). The classic black mat in its "type" area (the Upper San Pedro Valley of Arizona, including the Clovis site at Murray Springs) is a wetland deposit resulting from wetter conditions that occurred at and after the YD onset[40–42]. Several studies report that the local black mat is frequently older or younger than the YD onset[40–42], but they most commonly date to the YD chronozone between ~12,800 and ~11,700 cal BP[40,41]. Most classic black mats in the United States do not contain much charcoal[40,43], but it is sometimes abundant immediately below the black mat[40], where the YDB layer typically is found[1,3] Across Northern Europe, layers analogous to black mats in the United States are typically rich in charcoal[1].

Wolbach *et al.*[3] summarized previous studies (their Table A2) showing that 24 of 27 YDB sites with black mats also display peaks in YDB proxies (e.g., magnetic spherules, carbon spherules, high-temperature meltglass, and/or nanodiamonds). The authors of these studies argued that the presence of these YDB proxies suggests, but is

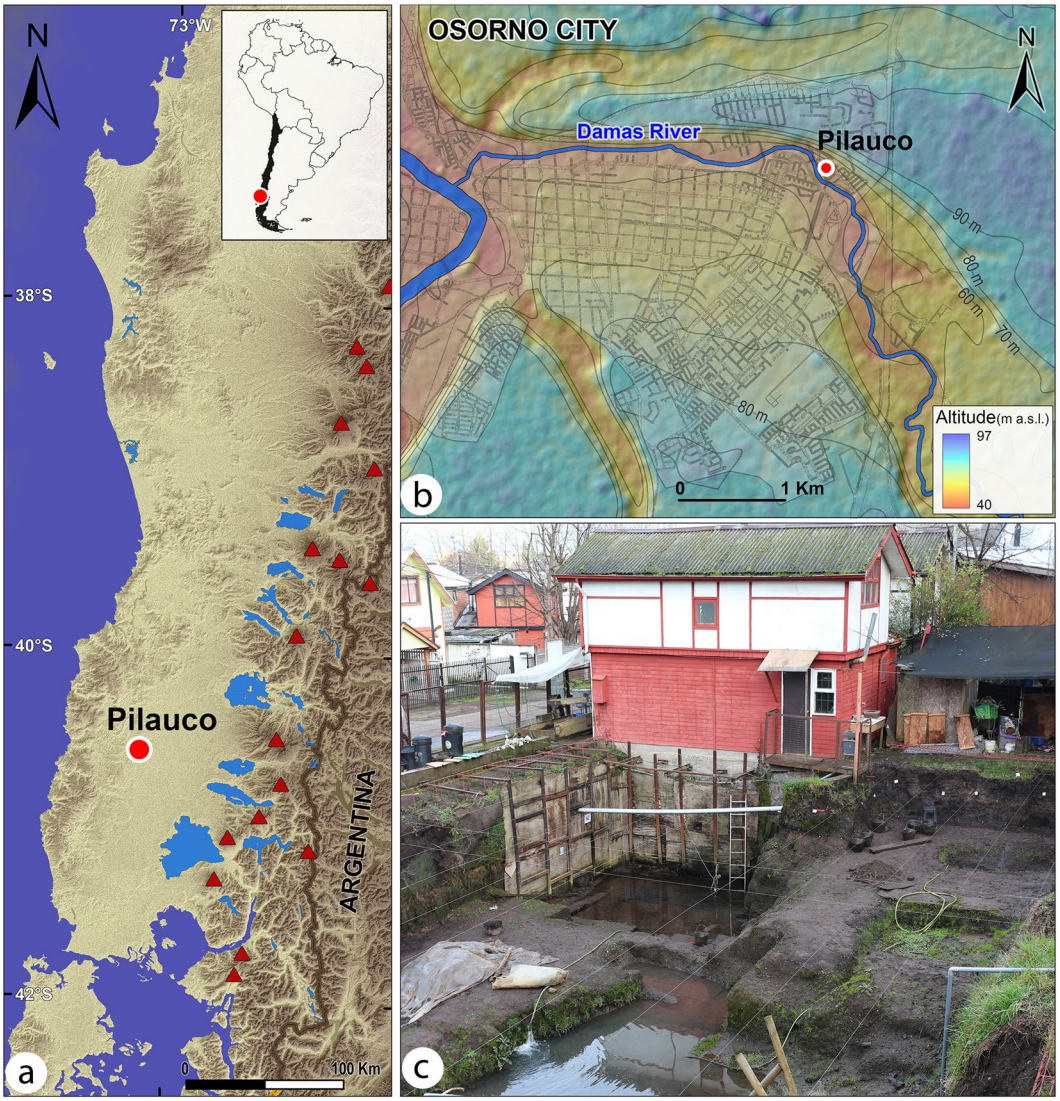

Figure 1. Site location. (**a**) Shaded elevation map of parts of Chile and Argentina showing regional setting of the Pilauco site; red triangles represent Andean volcanoes. Base map: ASTER GDEM is a product of NASA and METI; U.S. Geological Survey data release, 10.5067/ASTER/ASTGTM.002. Image modified with Adobe Photoshop CC2014 (https://www.adobe.com/products/photoshop.html). (**b**) Site location within the city of Osorno. Dataset for base map: ©JAXA/METI (Japan Aerospace Exploration Agency/Ministry of Economy, Trade, and Industry), 2017, 10.5067/Z97HFCNKR6VA. Both images were modified with Adobe Photoshop CC2014 (https://www.adobe.com/products/photoshop.html) and Adobe Illustrator (https://www.adobe.com/products/illustrator.html). (**c**) Photograph of the protected Pilauco site excavations.

not conclusive of a relationship among the YDB impact event, an intense episode of biomass burning, and the 12,800-year-old black mat.

After the black mat's discovery at Pilauco, several stratigraphic sections on the west wall of the excavations were sampled for different environmental and potential impact-related proxies. Grid 8AD samples were examined for seeds, magnetic spherules, and Pt concentrations (Supplementary Fig. S2). Samples from grid 10AD were examined for charcoal and pollen concentrations (Fig. 2), and grid 14AD was sampled for radiocarbon dating and *Sporormiella* spp. spores (Supplementary Fig. S3). All grids were examined for megafaunal remains, wood fragments, and lithic artifacts[28]. The potential presence at Pilauco of meltglass, carbon spherules, glasslike carbon, and other reported YDB proxies has yet to be investigated. Experiments are underway to investigate the presence of nanodiamonds and aciniform carbon/soot that often are associated with cosmic impact events[1,3,11]. In the Methods section below those workers responsible for sample collection and testing are indicated.

Section 2: Chronology

In developing an age-height model (Fig. 3), we used Bayesian analysis based on the protocol given in Kennett *et al.*[35]. This age-height model allows us to infer the following Bayesian age spans and deposition rates for the sedimentary profile in grid 8AD. PB-6: this unit contains wood fragments with a youngest calibrated radiocarbon age of 17,233 ± 103 cal yr BP (Supplementary Tables S4 and S5). Bayesian analysis indicates the boundary of PB-6

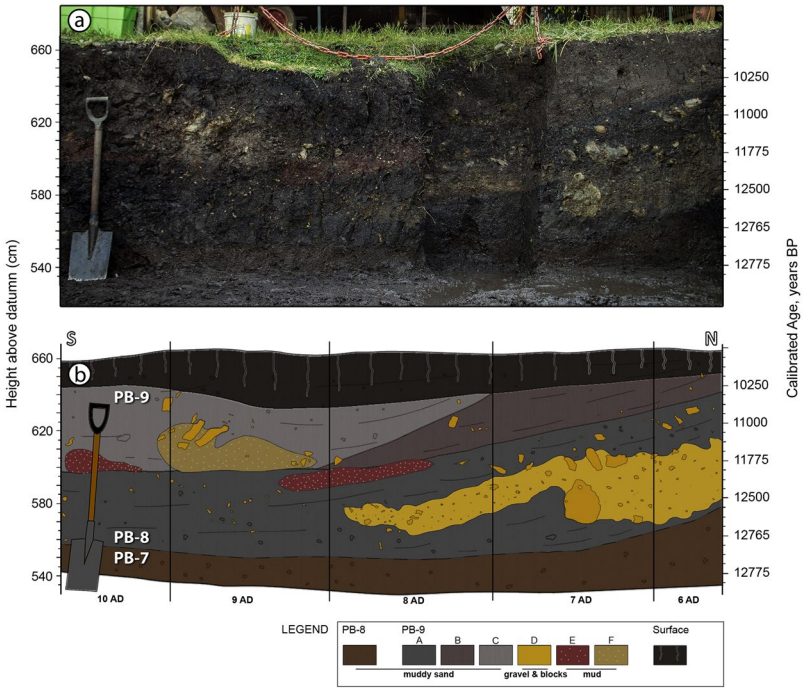

Figure 2. Stratigraphic section of the west wall. (**a**) West wall photograph. (**b**) Corresponding profile of grids 6AD to 10AD. These profiles show the abrupt contact between units PB-8 and PB-9, which dips ~15° to the south near the southern hill (grids 6AD to 7AD). Legend defines subunits. A young organic soil caps the sequence. See Supplementary Tables S2 and S3 for further details.

(~325 cm) dates to ~16,260 ± 260 cal yr BP with a terminal deposition rate of 19 yr cm^{-1}, the slowest rate observed in the profile. PB-7: the age span of this unit is ~16,260 ± 260 (at ~325 cm) to 15,200 ± 240 cal yr BP (405 cm) with an average deposition rate of 13 yr cm^{-1}. PB-8: the age span of this unit is 15,200 ± 240 cal yr BP (405 cm) to 12,770 ± 160 cal yr BP (550 cm, representing the YDB layer) for an average deposition rate of ~17 yr cm^{-1}. The sedimentation rate across the PB-8/PB-9 boundary is ~5 cm in ~2.5 years, a very rapid rate of ~0.5 yr cm^{-1}, the fastest observed in the sequence. This unit represents a continuous record that allows high-resolution investigations such as ours. PB-9: this unit ranges in age from ~12,770 ± 160 (550 cm) to 10,250 ± 150 (640 cm) with an average deposition rate of ~28 yr cm^{-1}.

Results and Discussion

Section 3: Spherulitic sedimentary particles. At Pilauco, we identified several discrete groups of rounded micro-particles (Supplementary Table S6) that include, (1) melted Fe- and Si-rich spherule, (2) melted chromium (Cr)-rich spherules, (3) melted Si-rich volcanic spherules, (4) non-melted authigenic framboids, (5) melted anthropogenic spherules, and (6) non-melted detrital grains that resemble spherules.

Group 1: YDB spherules. Previous studies[1,10,20,44–46] have identified distinctive crystalline textures on Fe-rich YDB spherule surfaces, indicative of high-temperature melting at >1450 °C followed by rapid quenching. In grid 8A at Pilauco, an abundance peak in melted, textured YDB spherules was observed only in samples between 580 and 550 cm (Fig. 4a,d), and was not found in other samples. The highest measured concentration of impact-related spherules at Pilauco is ~520/kg (Fig. 4a) at 552 cm in Grid 8AD (Fig. 4d). The average size of these spherules is ~45 µm with a range of ~95 to ~10 µm (Fig. 5 and Supplementary Fig. S6).

Eleven SEM-EDS analyses show that Group 1 spherules are distinctive in that they contain only two oxides: FeO, averaging 93.7 wt.% (range: 100 to 86.6 wt.%) with a small percentage of SiO_2 (Supplementary Table S7). High formation temperatures for these spherules are indicated by the presence of FeO (melting point: ~1450 °C), SiO_2 (melting point: ~1750 °C) and a lack of low-temperature volatiles such as Na_2O and K_2O, which vaporize at lower temperatures. The presence of titanium in some of Pilauco's YDB spherules is consistent with melting of titanomagnetite grains as has been previously reported[44,47]. We infer that some Group 1 spherules formed from the melting of magnetite and titanomagnetite grains that are common in the Pilauco bulk sediments.

Group 1 spherules found at Pilauco are unusual in that they exhibit considerable variation in composition and oxygen fugacity, ranging from oxygen-reduced, dendritic, Fe-rich spherules to fully oxidized Fe-oxide spherules that are found in very close proximity to one another. Four Group 1 spherules (Fig. 5a,b,e,and f), for example, were formed from highly reduced melt with a low oxygen fugacity (*f*O2) along the Fe-wüstite buffer (IW) (Supplementary Table S7). These spherules are not composed of typical terrestrial Fe_2O_3 (hematite; Fe:O ratio of ~70:30) or Fe_3O_4 (magnetite; Fe:O ratio of ~72:28), but rather of FeO (wüstite; Fe:O ratio of ~78:22 to ~81:19).

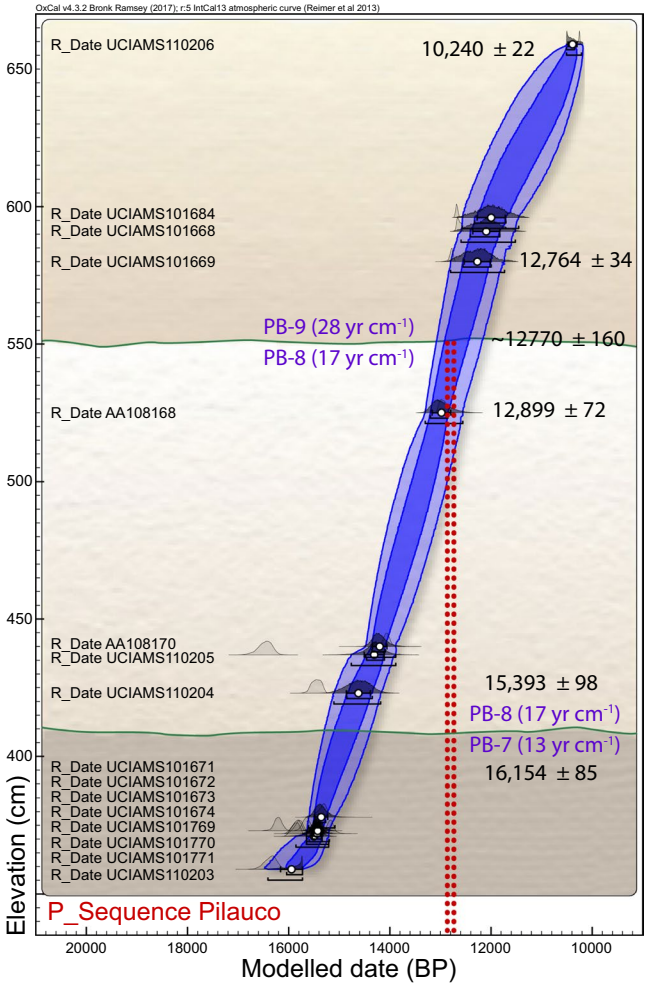

Figure 3. Bayesian age-height model based on 16 radiocarbon dates from grid 14AD (Supplementary Fig. S1 and Table S5). Green lines represent the stratigraphic boundaries PB-7/PB-8 and PB-8/PB-9; the latter has a Bayesian-calculated age of 12,770 ± 160 cal BP. Inferred depositional rates in yr cm^{-1} are in parentheses. Vertical red dotted lines represent age range of 12,835–12,735 cal BP for the proposed YDB impact event[35]. Red dotted lines overlap the PB-8/PB-9 boundary, consistent with the age of the YDB cosmic impact event. Produced with OxCal v. 4.3.2, SHCal13 calibration curve for the Southern Hemisphere.

This composition rarely occurs under normal terrestrial conditions (e.g., from volcanism or anthropogenesis), but is common in meteorites and impact melts having much lower oxygen percentages. In addition, some non-spherulitic magnetic grains extracted from the YDB layer (552 cm) are composed of highly reduced native Fe at 97% Fe (Fig. 6, Supplementary Fig. S7) and/or reduced magnetite as FeO (Supplementary Fig. S8). Similar low-oxygen melted minerals were observed in spherules and meltglass from the YDB layer at Abu Hureyra, Syria and in meltglass from the Trinity atomic bomb test site at Alamogordo, New Mexico[20].

By plotting the SEM-EDS results of Pilauco Group 1 high-temperature Fe-rich spherules in ternary diagrams (Fig. 7), comparisons can be made to other known spherule types. Group 1 spherules are dissimilar in composition to known anthropogenic spherules that are produced primarily by coal-fired power plants, and are typically enriched in CaO, MnO, and low-temperature Na_2O[20,46] (Fig. 7a). Group 1 spherules are also dissimilar to known volcanic spherules (Fig. 7b), which are typically more highly enriched in CaO, MnO, as well as low-temperature Na_2O[20,46]. Additionally, the presence of rapidly quenched Fe crystals (Fig. 7a), requiring high temperatures >1450 °C, rules out an authigenic origin because, by definition, such spherules are unmelted.

The ternary diagrams also indicate that Group 1 spherules do not have typical meteoritic compositions because most stony micrometeorites (96% of all micrometeorites) have MgO concentrations >10 wt.%[20,46] whereas Group 1 spherules contain no detectable MgO. In addition, Group 1 spherules are not Fe-rich micrometeorites ablated from typical Fe meteorites (~4% of meteorites) because such meteorites typically have high-Ni concentrations (averaging 9.0 wt.%, n = 76; maximum = 42.6 wt.%[48]) whereas Group 1 spherules contain no detectable Ni. Pilauco's Group 1 spherules, however, could have been ablated from a low-Ni, low-MgO impactor. In addition, Group 1 spherules are geochemically similar to spherules produced during extraterrestrial impact events that melted and ejected target rocks (Fig. 7d). Impact-related spherules from a number of confirmed

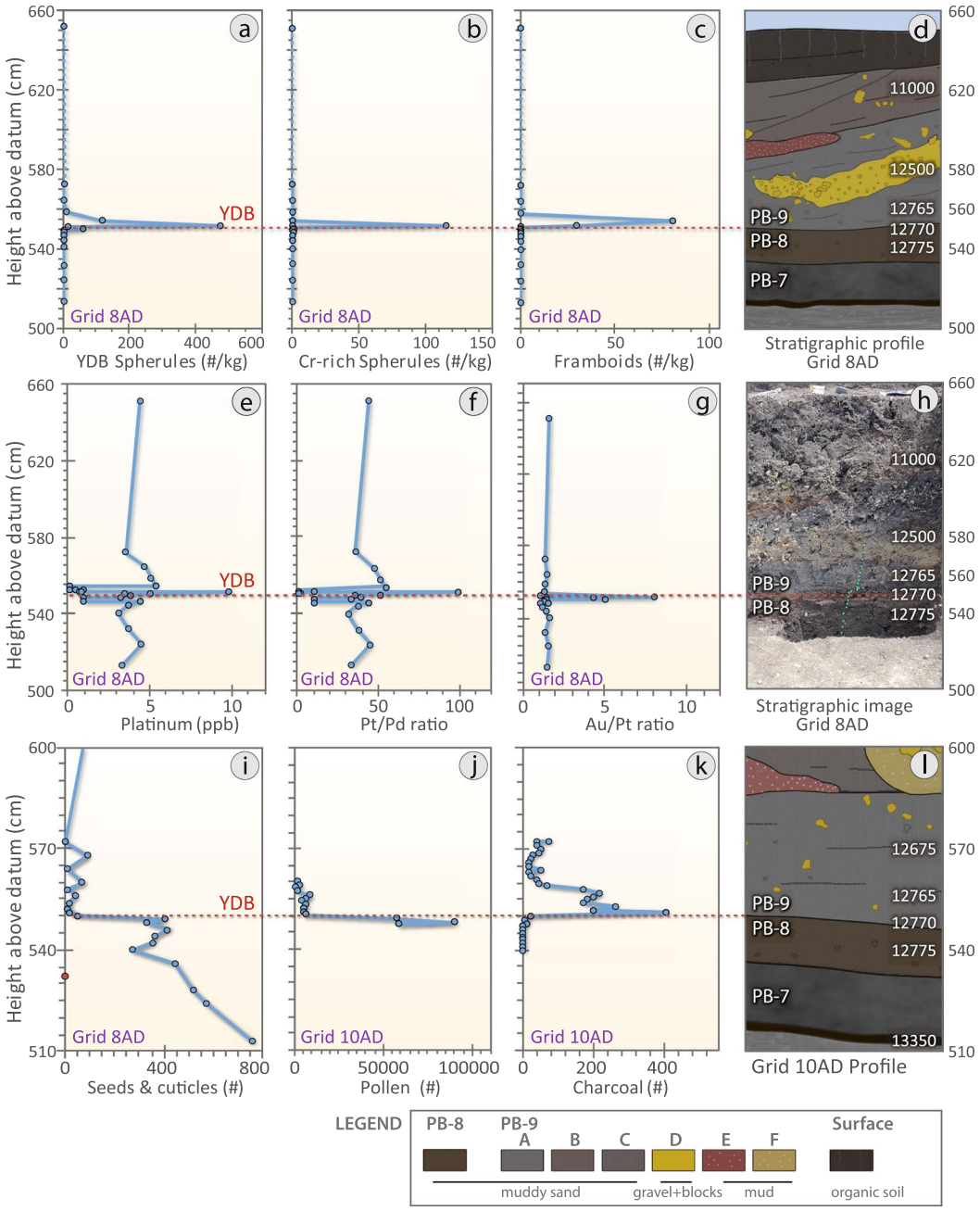

Figure 4. Changes in impact-related and environmental proxies at the PB-8/PB-9 boundary (YDB), showing peak concentrations of high-temperature impact spherules, framboids, and elemental proxies, including Pt, along with changes in charcoal and plant macrofossil abundances. (**a**) Group 1: high-temperature, Fe- and Si-rich impact spherules exhibit a peak abundance of ~520/kg at ~552 cm; (**b**) Group 2: Cr-rich spherules have a peak abundance of ~115/kg at ~552 cm; (**c**) Group 4: authigenic framboids have a peak abundance of ~80/kg at ~554 cm. (**d**) Stratigraphic profile of grid 8AD. Age of PB-8/PB-9 boundary is 12,770 ± 160 cal yr BP. (**e**) Pt abundance peak of 9.9 ppb in the YDB layer at 551 cm coincident with the boundary of units PB-8 and PB-9. (**f**) Anomalous Pt/Pd ratios are restricted to the PB-8/PB-9 boundary suggesting the influx of non-local Pt at the YDB. (**g**) Anomalous Au/Pt ratios are also restricted to the PB-8/PB-9 boundary suggesting the influx of non-local Au at higher concentrations than those of the non-local Pt. (**h**) Photograph of sampling section in grid 8AD. Green pins mark sampling levels. (**i**) Abundance record of seeds showing the major decline at the YDB layer. (**j**) Pollen concentrations showing the abrupt decline in the YDB layer. (**k**) Abrupt increase in charcoal peaking at the YDB layer with continuing high concentrations in the overlying ~10 cm. (**l**) Stratigraphic profile for grid 10AD. Group 3 volcanic spherules were found in low concentrations throughout the profile in grid 8AD (not plotted here; see Supplementary Fig. S11a). Group 5 anthropogenic spherules were restricted to surface sediments in grid 8AD (not plotted here; see Supplementary Fig. S11b). Group 6 rounded detrital grains (not plotted) are common throughout the entire profile. Legend is the same as in Fig. 2.

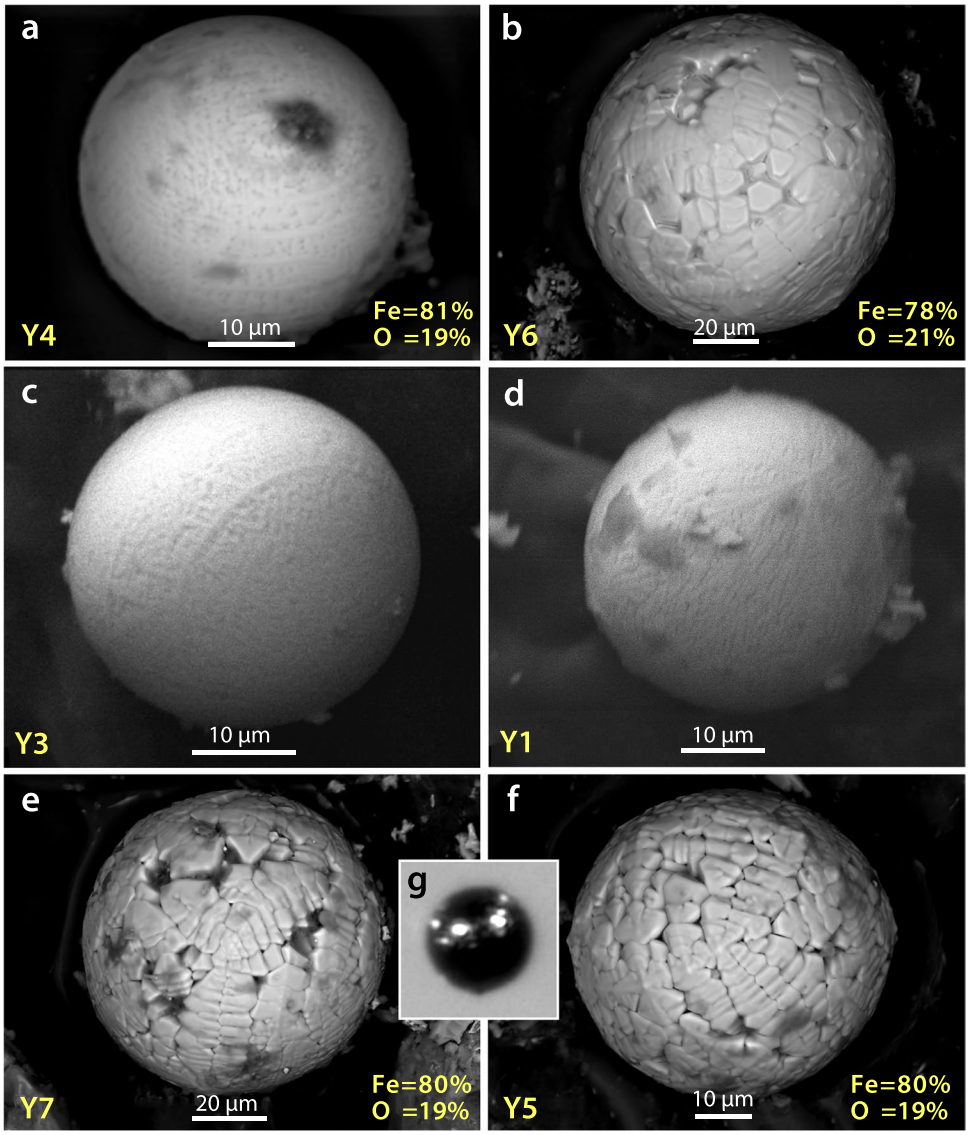

Figure 5. Group 1 SEM Images: High-temperature Fe-rich impact-related spherules. (**a**–**f**) High-temperature impact spherules have distinctive dendritic surface texturing indicative of rapid quenching from melt temperatures above ~1450 °C. SEM-EDS analyses for each spherule are in Supplementary Table S7. Elemental composition of spherule in (**b**) is in Supplementary Fig. S6. (**g**) Photomicrograph of high-temperature impact-related spherule illustrating the difficulty in distinguishing these from framboids (Fig. 11a) and detrital grains (Fig. 11c). Note percentages of Fe and O at lower right of some images. The composition of these spheroids is FeO (wüstite), a highly reduced mineral that almost never occurs under natural terrestrial conditions, but is common in meteorites and materials produced during impact events under oxygen-deficient conditions.

sources fall into two distinct geochemical groups, one that is Fe-rich and the other Si-rich; the compositions of the YDB spherules from Pilauco only overlap with those of the former.

Group 2: Chromium-rich spherules. A second group of spherules was also found only in the 12,800-yr-old layer at Pilauco (552 cm). This group shows a concentration of ~115 spherules/kg ranging from ~45 to ~42 µm in diameter with an average of ~43 µm (Figs 4b and 8a,b; Supplementary Table S6). Group 2 is differentiated from Group 1 spherules by the presence of Cr oxide (Cr_2O_3) that averages 6.2 wt.% (range: 3.9 to 13.3 wt.%) (Supplementary Table S7). Approximately half of these Cr-rich spherules contain TiO_2 (average: 6.1 wt.%; range of 8.6 to 0.0 wt.%), and no other Pilauco spherules observed outside of the 12,800-yr-old layer contain any detectable Cr_2O_3.

In exploring the source of the Cr-rich spherules, we determined that all 23 sediment samples from 651 to 513 cm contain variable amounts of Cr-rich vesicular basalt fragments that are up to several cm in diameter. In one sample, the basaltic matrix is composed of aluminosilicate glass (Al: 2.3 wt.%; Si: 19.1 wt.%; Mg: 8.1 wt.%; and Ca: 8.6 wt.%) (Supplementary Fig. S9a). Although the bulk sediment contains no detectable Cr, those basaltic fragment examined contain numerous Cr-magnetite inclusions (Cr: 10.1 wt.%; Fe: 74.8 wt.%; Si: 5.5 wt.%;

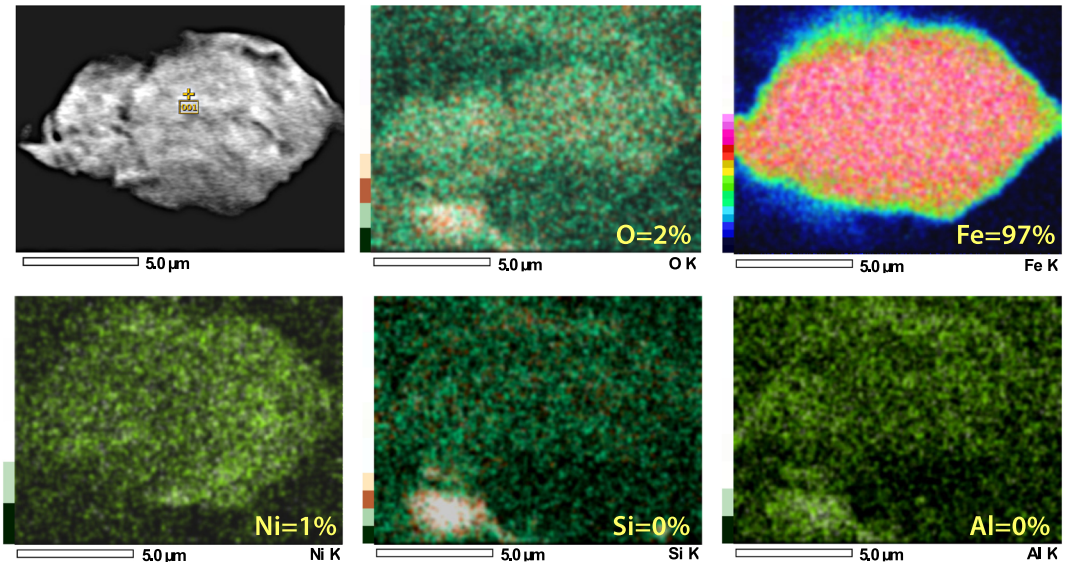

Figure 6. SEM-EDS elemental map of YDB magnetic grain. Upper left, SEM image of magnetic grain. SEM-EDS elemental map and separate spot analysis (yellow cross on upper left image) show that this highly reduced grain is composed of ~97% Fe, 2% O, and ~1% Ni, suggesting a possible extraterrestrial origin. Si and Al were undetectable in the grain itself but were detected in surface debris shown by the whiter-colored areas in the two lower right images. Elemental composition is provided in Supplementary Fig. S7.

and Al: 2.6 wt.%) (Fig. 8c,d; Supplementary Figs S9b and S10) that most likely crystalized as the lava cooled. These non-spherulitic inclusions contain nearly identical relative concentrations of Cr and Fe as those found in the Cr-rich spherules of Group 2 (Cr: 10.1 wt.%; Fe: 74.8 wt.%; Si: 5.5 wt.%; and Al: 2.6 wt.%) (Supplementary Table S7) suggesting that the Cr-rich spherules formed from the melting of local Cr-rich basaltic material.

The Cr-rich spherules from Pilauco contain an average of 6.05 wt.% Cr_2O_3 (max: 8.58 wt.%), and are unlike any known volcanic spherules, including those from two Peruvian volcanoes (Huainaputina and Ubinas) that contain an average of only 0.05 wt.% Cr_2O_3 (range of 0.00 wt.% to 0.73 wt.%)[49]. Similarly, there are no known volcanic spherules reported in the literature that contain more than ~1.1 wt.% Cr_2O_3[49], which is much less than the minimum of 3.9 wt.% found in the Cr-rich spherules from Pilauco. Group 2 spherules also contain high concentrations of Fe unlike other known volcanic spherules, which are typically composed of FeO averaging 12.2 wt.%, SiO_2 averaging 50.9 wt.%, Al_2O_3 averaging 18.5 wt.%, and CaO averaging 10.0 wt.%. The maximum amount of Fe reported in volcanic spherules is 35.5 wt.%, compared to the minimum amount of 74.3 wt.% in Pilauco's Cr-rich spherules.

After a volcanic eruption, Cr-magnetite inclusions can form from supergene or hypogene processes (deposition or enrichment of mineral deposits by solutions moving downward through magmatic rocks)[50] at ambient temperatures of far less than that of molten basalt[51] (~1300 °C). Much higher temperatures of ~1670 °C to 2160 °C, are required to re-melt these Cr-rich inclusions[52,53] to form spherules. Because this range exceeds known temperatures of erupting magma, the melted Cr-rich spherules at Pilauco almost certainly were produced by some post-eruptive, non-volcanic process. The high temperatures required to produce the Cr-rich spherules are limited to only a few processes, such as anthropogenesis, lightning, and cosmic impact[20]. Anthropogenesis seems unlikely because we found no similar Cr-rich spherules at the surface in industrial-age sediments, but only at a depth of ~100 cm (height of 552 cm) in the ~12,800-year-old YDB layer. Lightning strikes are also an unlikely source because such spherules should therefore be a common occurrence in all strata, but instead, are restricted only to the 12,800-year-old YDB layer. This leaves cosmic impact as the most likely origin.

Group 3: Ca- and Si-rich basaltic volcanic spherules. A third group of spherules are Ca- and Si-rich relative to Group 1 and 2 spherules and are randomly distributed at low concentrations (0 to ~10 spherules/kg) in the five sedimentary samples analyzed from Pilauco (Fig. 9a,b, Supplementary Fig. S11a). None were found in the YDB layer. These spherules contain a range of ~61 to 17 wt.% SiO_2 along with highly variable concentrations of Na_2O, MgO, SO_3, and CaO (Supplementary Table S7). These compositions closely match those of the vesicular basalt fragments found in Pilauco sequences (Supplementary Fig. S5a), suggesting they are of volcanic origin.

Volcanic spherules like those of Group 3 are produced during eruptions of low-viscosity magmas when micro-droplets form that have the same composition as the melt[54]. Spherules from low-energy eruptions do not fall far beyond the base of volcanoes, which includes the foothills of the Andes near Pilauco. Volcanic eruptions capable of distributing tephra across wide areas are violent, explosive events driven by high gas pressures[55], and these energetic eruptions produce tephra shards that are angular rather than rounded. For instance, the largest known eruption of the last 5 million years, the 75,000-year-old Toba-lake eruption distributed tephra up to 2500 km from the caldera, but did not produce any known spherules[55]. Hence, it is unlikely that volcanism can account for spherules in the YDB layer at Pilauco (Group 1) as well as those found at other YDB sites on other

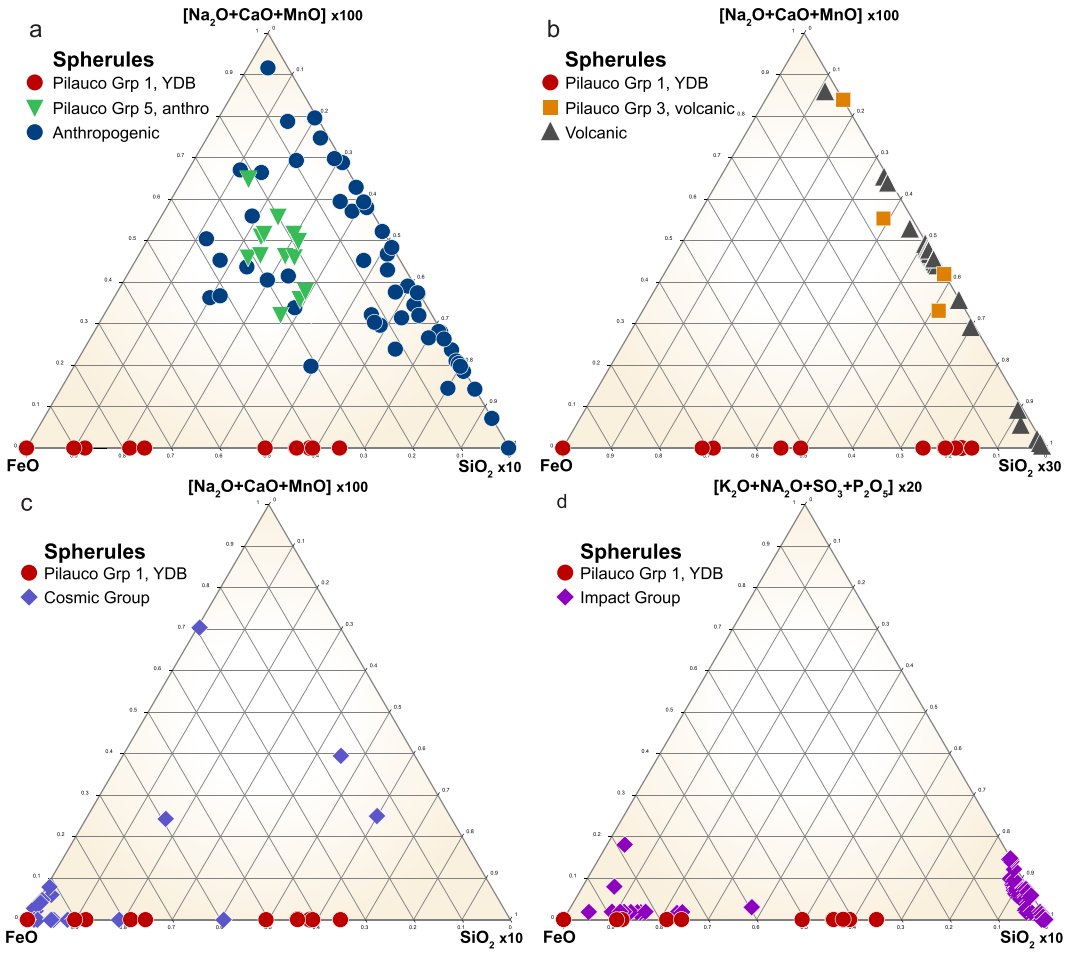

Figure 7. Ternary diagrams comparing compositions of spherules from the Pilauco site with other known types of spherules described in the literature[20,44,46,65]. (**a**) Group 1 high-temperature Fe-rich spherules (red dots) are compositionally unlike known anthropogenic spherules (blue dots) and unlike Group 5 anthropogenic spherules (green triangles) found at the surface of the profile in grid 8AD. (**b**) Group 1 spherules are compositionally different from known volcanic spherules (black triangles), which are geochemically similar to Group 3 Pilauco spherules (orange squares) thought to be volcanic in origin. (**c**) Group 1 spherules are geochemically similar to some cosmic spherules (blue diamonds) indicating that some YDB layer spherules at Pilauco might be cosmic in origin. (**d**) Group 1 spherules also are compositionally similar to spherules produced as ejecta during known cosmic impact events. Comparative data of non-Pilauco material are from Table 5 in the supplementary materials of Bunch *et al.*[20].

continents[20,46]. Furthermore, there are no reported examples of unequivocal volcanic spherules that contain 85 wt.% to 100 wt.% FeO as found in the Group 1 YDB spherules from Pilauco and from other YDB sites. Magma can contain Fe-rich crystals that can crystallize from the melt slowly over time, but there is no known mechanism by which YDB-like spherules containing >85 wt.% FeO can form from erupting magma composed of no more than ~13 wt.% Fe.

Group 4: Authigenic framboidal spherules. A peak in spherulitic framboids (~80/kg) occurs at a height of 554 cm, ~2 cm higher than the high-temperature YDB spherules found at 552 cm (Fig. 4c). These spherules are predominantly composed of hundreds of unmelted, cube-like, pyrite crystals (FeS_2) that formed slowly under anoxic conditions rather than instantaneously as with melted impact-related spherules[46]. Even though framboids are not directly related to the impact event, they are commonly associated with high-temperature impact-related spherules in the YDB layer at other sites[10,20,44,46], possibly because of post-YDB environmental disruption.

Group 5: Anthropogenic spherules. Spherules in Group 5 were found only in surface, industrial-age sediment samples at a height of 651 cm with an abundance of ~440 spherules/kg (Fig. 10, Supplementary Fig. S11b). Because these spherules are dendritic-textured, and hence morphologically similar to impact-related spherules of Group 1, they can only be differentiated geochemically by using SEM-EDS. The composition of these spherules closely matches known anthropogenic spherules (Fig. 7a), which are typically produced in large quantities by industrial processes, often from the burning of coal and combustion-related melting of included magnetite

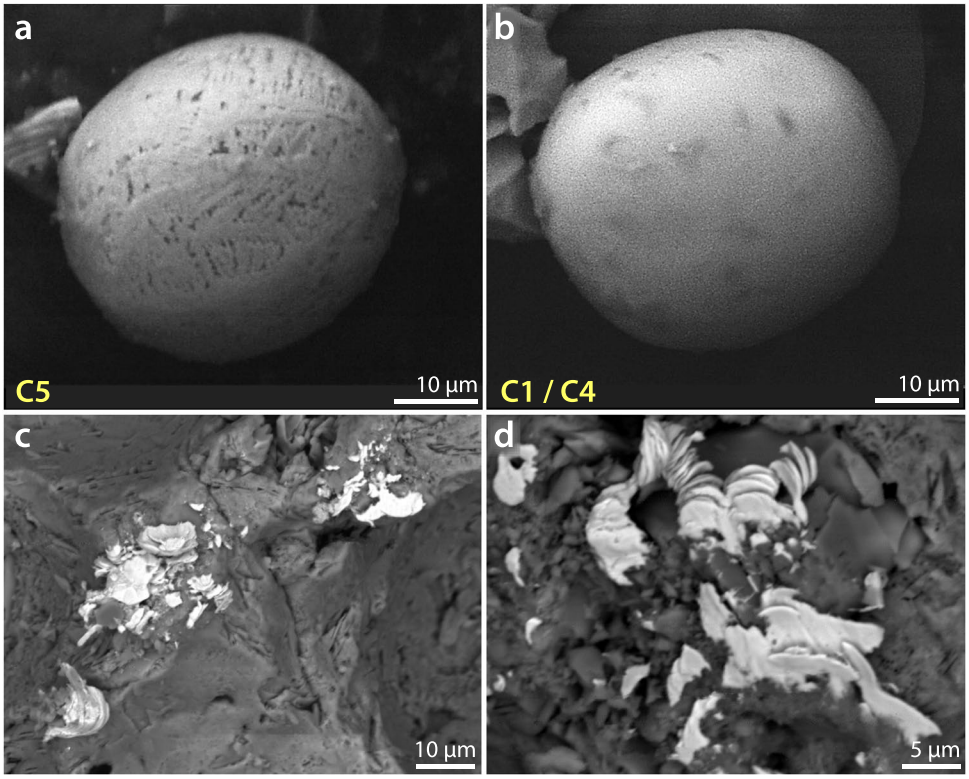

Figure 8. Group 2: Cr-rich spherules from Pilauco. Micrographs (**a**,**b**) show Cr-rich ovoidal spherules with SEM-EDS compositions matching Cr-magnetite inclusions that are commonly found in basaltic glass distributed randomly throughout the Pilauco profile. The spherule in (**a**) displays distinctive dendritic texturing indicative of melting and rapid quenching at temperatures above ~1670 °C, the melting point of Cr-magnetite. SEM-EDS compositional data for the spherules shown in Supplementary Table S7. (**c**,**d**) Typical Cr-magnetite inclusions in basaltic glass from Pilauco at a height of 513 cm that are commonly found in all samples throughout the profile. Scalloped stack of individual Cr-rich inclusions most likely resulted from supergene or hypogene processes (deposition or enrichment of mineral deposits by solutions moving downward through magmatic rocks).

grains[56]. Known anthropogenic spherules contain uniquely distinctive concentrations of MnO, MgO, CaO, and Al_2O_3, typically at $\leq$1 wt.%[20], as we observe in Group 5 spherules from Pilauco. Puffer[57] examined spherules from a wide variety of settings and concluded that anthropogenic spherules frequently contain 0.4–0.8 wt.% Mn, which is commonly used in the smelting of ferromanganese alloys. These values are similar to the range of 0.2 wt.% to 0.9 wt.% (average: 0.3 wt.%) for MnO in Group 5 spherules from surface samples at Pilauco.

Group 6: Rounded detrital grains. Throughout the Pilauco section, we observed detrital titanomagnetite grains (Fig. 11c–e) that when rounded and smoothed by abrasion can be easily mistaken for impact-related spherules when using reflected-light microscopy. The difficulty in differentiating spherule groups is evident in the photomicrographs of impact-related spherules (Fig. 5g), framboids (Fig. 11b), and detrital grains (Fig. 11e).

Summary of independent YDB spherule investigations. This paper describes in detail multiple types of spherulitic objects including authigenic, volcanic, detrital, framboidal, and YDB spherules, and Supplementary Table S8 summarizes a number of the unique and distinguishing characteristics of each type. Numerous other investigations[1,10,20,44,46] have shown that these various particles cannot be differentiated using reflected-light microscopy, but require the use of SEM-EDS as originally specified by Firestone *et al.* (page 17–18 of their Supporting Information)[1]. Of 13 subsequent independent studies, all claimed to have followed the Firestone protocol (details of studies in Supplementary Information, S1), but only eight studies correctly performed SEM-EDS analyses, and all eight confirmed the results of Firestone *et al.*[1]. Five of the 13 studies[15,43,58–60] reported that "YDB spherules" are distributed in non-YDB layers throughout the sediment investigated, and therefore, cannot be impact-related. However, those five studies either did not conduct SEM-EDS at all or did not correctly differentiate YDB spherules from non-YDB spherulitic objects, such as volcanic spherules, framboids, and detrital grains. These disparate results, some from studies using the same sedimentary profiles, clearly emphasize the necessity of performing SEM-EDS analyses.

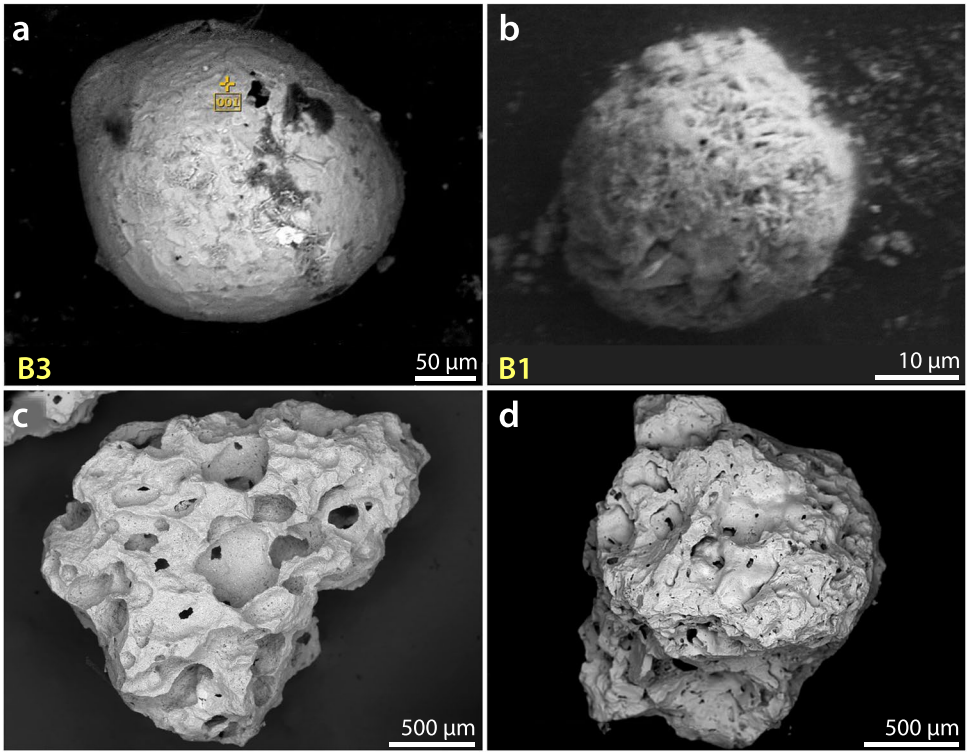

Figure 9. Ca- and Si-rich basaltic volcanic spherules and basaltic glass fragments from Pilauco. (**a**,**b**) Group 3 volcanic spherules contain SiO_2 at >17 wt.% and SO_3 at >1 wt.%, but lack Cr_2O_3. Compositions are listed in Supplementary Table S7. (**c**,**d**) Vesicular basaltic glass fragments from a height of 548 cm that are commonly found in all samples from the Pilauco profile. These fragments of basaltic glass contain Cr-rich inclusions and are geochemically similar to the Group 3 volcanic spherules in (**a**,**b**).

Section 4: Extraterrestrial platinum (Pt). The Pt-group elements (Pt, Ir, and Os) are common constituents of meteoritic and cometary material and are often used as indicators of extraterrestrial impact events. In their study of the YDB event, Petaev *et al.*[26] identified a conspicuous peak in Pt abundance at the onset of YD climate change in a Greenland ice core (Greenland Ice Sheet Project 2). These authors attributed a decades-long episode of Pt deposition to a cosmic impact event that resulted in "multiple injections of Pt-rich dust into the stratosphere[26]". The existence of such an impact proxy at the YD onset was predicted for Greenland ice core records at the time the YDB hypothesis was first proposed[1]. Since that initial discovery of a YDB Pt peak in Greenland, several more investigations have found elevated concentrations of Pt, and other Pt-group elements (PGEs), and high-temperature PGE-rich spherules, marking the YD onset within 28 widely separated sediment sequences across North America, Europe, and Asia[45,47,61–64] (Fig. 12). Prior to the present investigation, no YDB-age enrichments in Pt have been reported for YDB sites in South America.

At Pilauco we measured Pt, Pd, and gold (Au) concentrations in 17 samples, plus eight duplicates, using fire-assay and inductively-coupled-plasma mass spectrometry (ICP-MS). The results show that one significant Pt peak (Fig. 4e) in grid 8AD (Fig. 4h) reached 9.9 ppb at 551 cm (Supplementary Table S9). This value, the highest concentration in the record, is more than 3 × higher than the average background values of 2.7 ppb (range: 0.1 to 5.4 ppb) and closely corresponds with the peak in high-temperature YDB impact spherules. Two other aliquots of the same sample contained 0.7 and 0.8 ppb of Pt, values that are below background levels for unknown reasons. Perhaps the rapid deposition diluted Pt in the sediment and/or the absence of high-concentration Pt nuggets reduced the average concentrations[1,3,45,65]. Similarly, both Pd and Au reach large abundance peaks at 551 cm (Supplementary Fig. S12a,b).

After normalizing Pt to Pd, we found that the Pt/Pd ratios are 2× higher than background ratios (Fig. 4f) in the YDB layer, but not in samples from above or below it. Similarly, Au/Pt ratios are 5× higher than background ratios (Fig. 4g), and these ratios fall within the range of elevated values reported from other YDB sites[45]. The background values of Pt in Pilauco sediments are higher than those for all other Pt-rich YDB sites[45], probably due to the influence of Pt-rich basalts from nearby Andean volcanoes. In the YDB layer, however, the Pt/Pd and Au/Pt ratios are significantly higher than those of the local basalt, strongly suggesting an influx of nonlocal Pt, Pd, and Au ~12,800 years ago superimposed on higher-than-normal background concentrations of volcanic Pt.

The Pilauco results for Pt and Pd are similar to those reported by Moore *et al.*[45] for 13 YDB sites across North America. Those workers interpreted the high concentrations of Pt and Pd as resulting from the influx of impact-related material from a nonlocal source. To possibly explain the high concentration of Pt, Pd, and Au in the YDB layer at Pilauco, we have considered the following four alternate explanations:

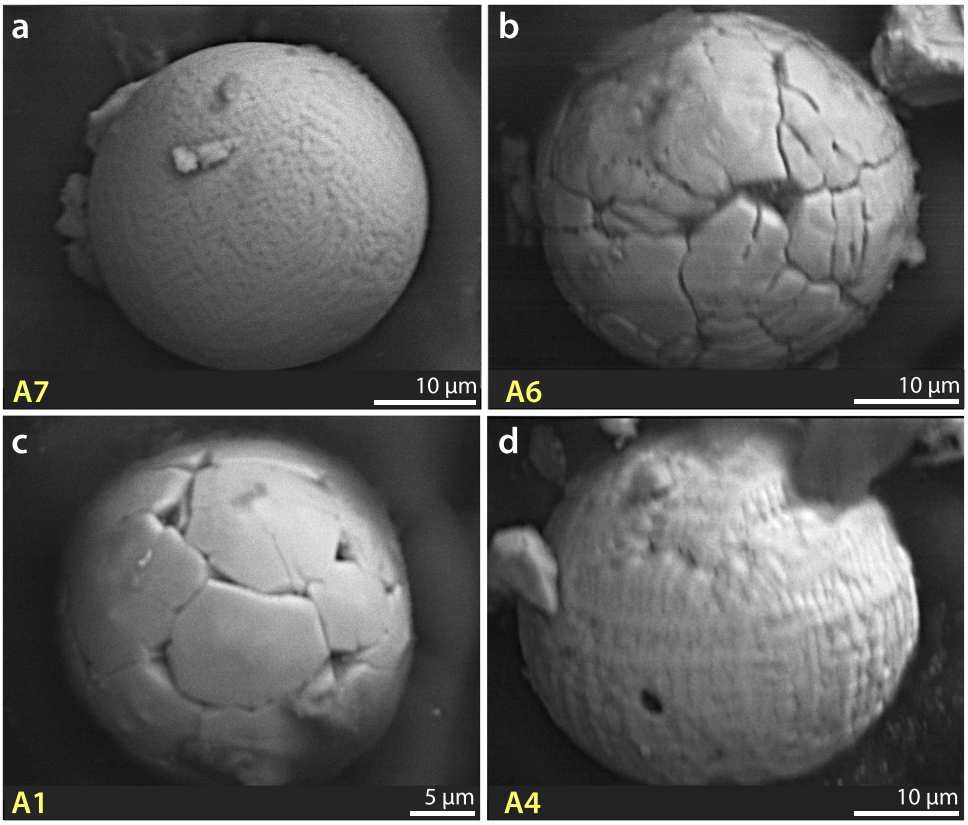

Figure 10. Group 5: Anthropogenic spherules. (**a**–**d**) SEM images of anthropogenic spherules found only in surface sediments at Pilauco. They are morphologically similar to Group 1 impact-related spherules, but SEM-EDS analyses show that these spherules are geochemically dissimilar to all other groups at Pilauco. Ternary diagram in Fig. 7a demonstrates geochemical similarity of them to known anthropogenic spherules.

Volcanic. Are the enrichments volcanic in origin, especially since Andean basalt at Pilauco already contains high concentrations of Pt? This explanation is unlikely, however, because the Pt/Pd and Au/Pt ratios in the YDB layer are substantially different from those in the layers above and below it. This most likely indicates that the enrichment peaks are not concentrations of volcanic PGEs, but rather, resulted from the influx of Pt, Pd, and Au from some other source than the local Andean volcanoes.

Lag deposit. Are the enrichments in Pt, Pd, and Au possibly represent a lag deposit, formed from aeolian and/or fluvial action? This explanation is unlikely, however, because typical lag deposits do not contain high-temperature Fe- and Cr-rich spherules[1].

Cosmic flux of micrometeorites. Did slow sedimentation rates cause higher concentrations of micrometeorites enriched in Pt and Pd? The sedimentation rate across the YDB layer, however, is 0.5 yr cm^{-1}, which is among the fastest in the record thus eliminating this as a possibility.

Coincidence. Is the co-occurrence of Pt, Pd, and Au simply coincidental? If so, peaks in Pt and magnetic spherules should co-occur at random in non-YDB layers. However, no such synchronous, co-occurrence has ever been found outside of the YDB layer at Pilauco or at any other YDB site worldwide or in any other non-YDB stratigraphic layer.

Cosmic impact. Finally, the PGE enrichment could have resulted from the influx of nonlocal, impact-related Pt, Pd, and Au, all of which are enriched above local background levels. This is the only explanation consistent with the evidence from known cosmic impact sites and is favored for the Pilauco YDB layer. Although this evidence is not conclusive of a YDB impact event, the age for the YDB layer at Pilauco is coeval with ages for those layers found on other continents, supporting the YDB cosmic impact hypothesis.

Section 5: Biomass Burning. A history of biomass burning at Pilauco was first determined by Abarzúa and Lobos[32] from the quantitative analysis of micro-charcoal particles (<150 um) collected in grid 14AD. Charcoal is almost absent in the interval from ~16,000 to 12,800 cal BP, indicative of low fire activity in a pre-YDB interval that was marked by a cold, relatively wet climate as determined by pollen assemblage analysis. Then, beginning at ~12,800 cal BP and continuing for several hundred years, there was a major increase in charcoal abundance that indicates an anomalous episode of biomass burning (Fig. 13).

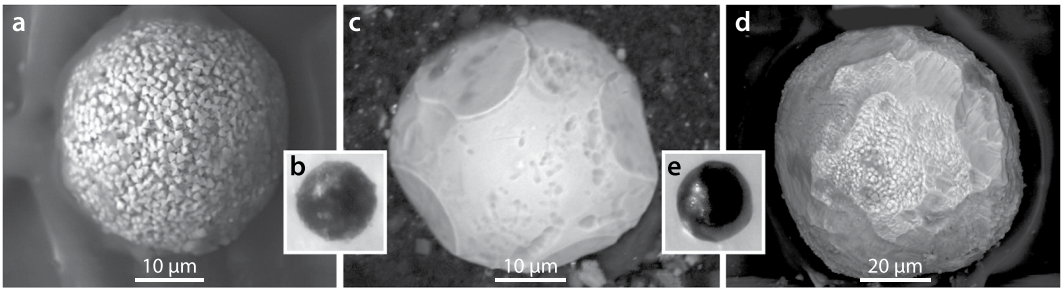

Figure 11. Group 4: Authigenic pyritic framboids and detrital magnetite. (**a**) SEM image of a framboid that contains Fe, sulphur, and oxygen and is composed of distinctive, unmelted cube-like crystals that formed slowly over time. (**b**) Photomicrograph of a framboid showing how difficult it is to distinguish these from YDB spherules (Fig. 5g) and detrital grains (**e**) using reflected-light microscopy. (**c**,**d**) Sub-rounded detrital grains rich in TiO_2 (average: ~36 wt.%) and FeO (average: 64 wt.%). (**e**) Photomicrograph of detrital grain showing its similarity to YDB spherules (Fig. 5g) and framboids (**b**) emphasizing the need to use SEM-EDS analysis.

To further investigate the biomass-burning history at Pilauco, we used macroscopic charcoal concentrations (>125 um) from grid 10AD (Fig. 4l). This analysis showed low charcoal concentrations in the upper part of unit PB-8 (Fig. 4k), which pre-dates the YDB layer. Above the YDB layer, there are peak concentrations of charcoal at the base of unit PB-9, immediately following the ~12,800-year-old stratum, which is also marked by high concentrations of Pt and high-temperature impact-related spherules. Following this major peak, charcoal concentrations decline, but values remain higher than in the underlying unit PB-8. This charcoal peak is the highest in the sequence analysed and indicates an anomalously large biomass-burning episode beginning near the onset of YD climate change at ~12,800 cal BP. This biomass-burning episode appears to have contributed to significant vegetational shifts in the temperate rainforest of the Chilean Lake District[66].

Marlon *et al.*[19] argued against a peak in biomass burning at the YD onset across North America, but their conclusion was challenged by Wolbach *et al.*[3], who analyzed 152 YDB charcoal records from four continents, including 28 lake sequences from nine countries across South America (five lakes are in Chile). Wolbach *et al.*[2] argued that an anomalous episode of biomass burning occurred that is also supported by unusually large concentrations of ammonium, nitrate, formate, oxalate, and acetate in three high-resolution Greenland ice cores[67–71]. This biomass-burning peak is one of the highest of the last ~120,000 years and began precisely at the YD onset. In addition, these biomass-burning proxies are coeval with a large impact-related abundance peak in Pt[26]. In support of an association between increased biomass burning and the YDB event, Wolbach *et al.*[3] reported in their Appendix Table A2 that the peak concentrations of YDB spherules, meltglass, and nanodiamonds are coeval with YDB biomass-burning proxies on three continents, including charcoal (23 of 32 terrestrial sites; 4 of 4 lakes), aciniform carbon/soot (7 of 14 terrestrial sites; 0 of 1 lakes), and wildfire-related carbon spherules (22 of 32 terrestrial sites; 2 of 4 lakes). Moreover, the Bayesian-modeled ages for these sites overlap the proposed age range of the YDB event between 12,835 and 12,735 cal BP.[35] Furthermore, Wolbach *et al.*[2,3] argued that abundant soot and combustion chemicals from such widespread biomass burning might have initiated an "impact winter," as proposed for the K-T impact event[72,73], although disputed by some[74]. At the YDB, this, in turn, is proposed to have contributed to YD climate change and to megafaunal extinctions across large parts of the planet. Using the evidence presented by Wolbach *et al.*[2,3] as a guide, we observe that the YDB peak in biomass burning at Pilauco is consistent with subsequent post-YDB-impact environmental perturbations, but of course, does not prove by itself that an impact occurred. The Pilauco record is consistent with regional wildfire activity, indicating that anomalous YDB-age biomass burning reached into high latitudes of the Southern Hemisphere.

Section 6: Plant remains and pollen. *Fruits, Seeds, and Leaf Cuticle Record.* We recovered and analysed ~4,800 carpological (reproductive) structures (e.g., fruits, seeds, and capsules) from grid 8AD between 572 and 524 cm, allowing us to infer the local pre- and post-YD vegetational history (Figs 4i and 13; Supplementary Table S10). Samples from unit PB-8 below the YDB layer contain consistently abundant carpological structures with up to 573 specimens per sample (mean 370 ± 156 SD). Leaf cuticles of evergreen tree species are common below the YDB, as represented by two pioneering trees from the Proteaceae family (*Lomatia hirsuta* and *Embothrium coccineum*) and *Amomyrtus meli*, a tree from the Myrtaceae family that requires wet soil for proper growth. Additionally, other pioneering evergreen tree species such as *Aristotelia chilensis*, *Maytenus boaria*, and the endemic conifer, *Prumnopitys andina*, are represented in the seeds record from Pilauco, together with the herbaceous species *Montia fontana* and *Gunnera tinctoria* and several varieties from the Ranunculaceae, Cyperaceae, and Plantaginaceae families.

The seeds and cuticles from nearly all of these pre-YDB plants essentially disappear from the record after the sharply defined PB-8/PB-9 boundary (Fig. 13), representing both a major decrease in abundance and diversity of plant materials and a pronounced shift in the taxonomic composition of plant assemblages. Carpological structures are ~7× less abundant above the YDB layer and remain low throughout unit PB-9, ranging from 0 to 93 specimens per sample (mean 30 ± 34 SD).

To investigate whether the decline in abundance of carpological structures reflects a decline in the local vegetation or whether the absence of plant remains is an artifact of the sampling methodology, we used a negative binomial generalized linear model (GLM) regression (see Methods). Results from the GLM analysis indicate that

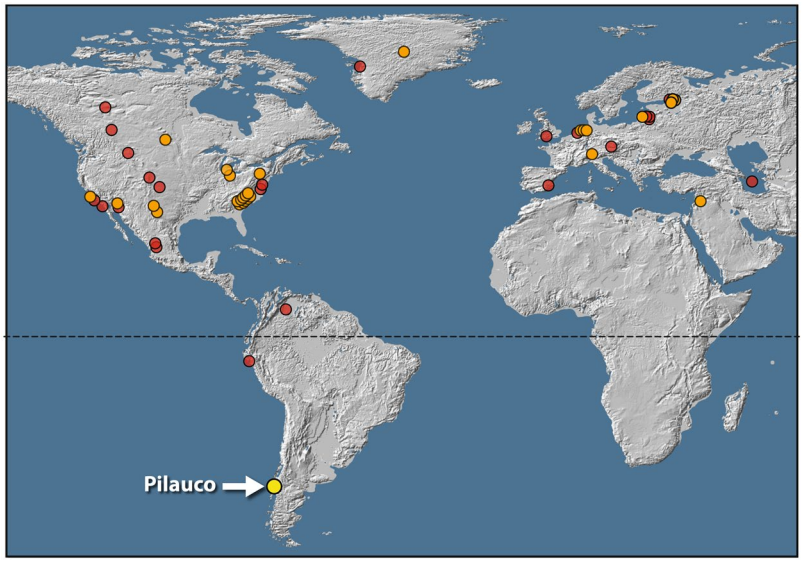

Figure 12. Location map showing 53 YDB sites. Orange dots represent 28 sites with peaks in both platinum (Pt) and other impact proxies such as high-temperature Fe-rich spherules. Red dots represent 24 sites with impact proxies but lacking Pt measurements. Yellow dot indicates the Pilauco site. North and Central America, n = 30 sites; South America, n = 3; Greenland, n = 2; Europe, n = 16; and Asia, n = 2. Map source: USGS, Sioux Falls, accessed October 17, 2011; and Japan ASTER Program (2003), ASTER Global Digital Elevation Map, GDEM-10 km-BW, accessed October, 2017 from https://asterweb.jpl.nasa.gov/gdem.asp, 10.5067/ASTER/ASTGTM.002. Modified with Adobe Photoshop CC2014 (adobe.com/products/photoshop.html).

the major, abrupt drop in seed abundance between units PB-8 and PB-9 is statistically significant, and hence, is unlikely to have resulted from taphonomic factors such as variable transport, preservation, deposition, and/or sampling protocol[75,76] (Supplementary Table S11).

Pollen Record. Similar to the carpological record, pollen concentrations remain consistently high up to the YDB layer, after which there is a dramatic and immediate decrease in abundance and diversity (species richness and Shannon index), along with a significant shift in taxonomic composition (vegetation turnover index) (Figs 4j and 13; Supplementary Table S12). A summary of the vegetation history and environmental/climatic interpretations for Pilauco and other regional sites is presented in Supplementary Table S13.

As with the fossil seeds, pollen assemblages below the YDB layer are diverse and abundant with the taxonomic composition indicating moderately dense, mostly non-arboreal vegetation dominated by Poaceae (grasses). This average assemblage is represented by a wide variety of North Patagonian taxa that decline after the YDB (Post-Pre YDB Ratio <1), including Myrtaceae (trees, 14.8%), *Nothofagus dombeyi*-type (trees, 2.3%), *Podocarpus nubigena* (conifer, 0.3%), *Pilgerodendron/Fitzroya* (conifers, 1.6%), *Tepualia stipularis* (tree, 1.1%), and *Raukaua latervirens* (vine, 1.8%). This pollen zone also includes other important plants: *Maytenus* sp. (tree, 10.8%), Cyperaceae (herbs, 2.5%), and the aquatic fern *Isoetes sp*. (0.6%). (Fig. 13; Supplementary Table S12). This assemblage is made up of mostly hygrophilous (i.e., preferring wetlands and moist environments), cold-resistant plants and trees characteristic of the North Patagonian forest, marked by cooler temperatures and relatively high rainfall/humidity[32,77–83].

At the YDB layer (PB-8/PB-9 boundary), the percentage of non-arboreal vegetation increased sharply from ~45% to ~85% of pollen (grid 14AD; Fig. 13), representing the largest change exhibited in the pollen record from Pilauco. Many of the previously dominant taxa characteristic of the North Patagonian forest disappeared or decreased from pre-YDB levels (lower Shannon index and species richness) with a remarkable shift in vegetation turnover index from 0 to 0.4 (Fig. 13; Supplementary Table S12).

The average assemblage that increase after the YDB (post-YDB to pre-YDB Ratio >1) include the dominant taxon Poaceae from 31% to 36.7%, *Aristotelia chilensis* (tree, 8.6%), *Saxegothaea conspicua* (conifer, 5.4%), *Prumnopitys andina* (conifer, 2.5%), *Weinmannia trichosperma* (tree, 4%), *Aextoxicon punctatum* (tree, 3.6%), *Drimys winteri* (tree, 0.93%), *Eucryphia cordifolia* (tree, 0.9%), Asteraceae (herbs, 8.4%), aquatic taxa (16.4%) and ferns (17.5%) (Fig. 13; Supplementary Table S12). This post-YDB assemblage is consistently associated with an abundance of macroscopic and microscopic charcoal that indicates a general increase in wildfire frequency.

Although the carpological and pollen record at Pilauco spans only a few hundred years, numerous regional studies[66,80–82,84] provide a solid context for the climatic interpretation of this major shift in vegetation. Despite pollen concentrations that decrease dramatically after the YDB (10× from 68,811 to 6,372 grains/cc), pollen is sufficiently abundant and diverse in the post-YDB sequence for the interpretation of broad environmental trends, especially when evaluated in the context of previous regional records. At the YD onset, drier conditions are indicated by the disappearance of aquatic ferns (*Isoetes* sp.; grids 10AD and 14AD), following their persistent presence throughout the pre-YDB sequence. These changes were also accompanied by increased biomass burning fostered by the onset of a marked seasonality of rainfall and warmer conditions. Furthermore, beginning at

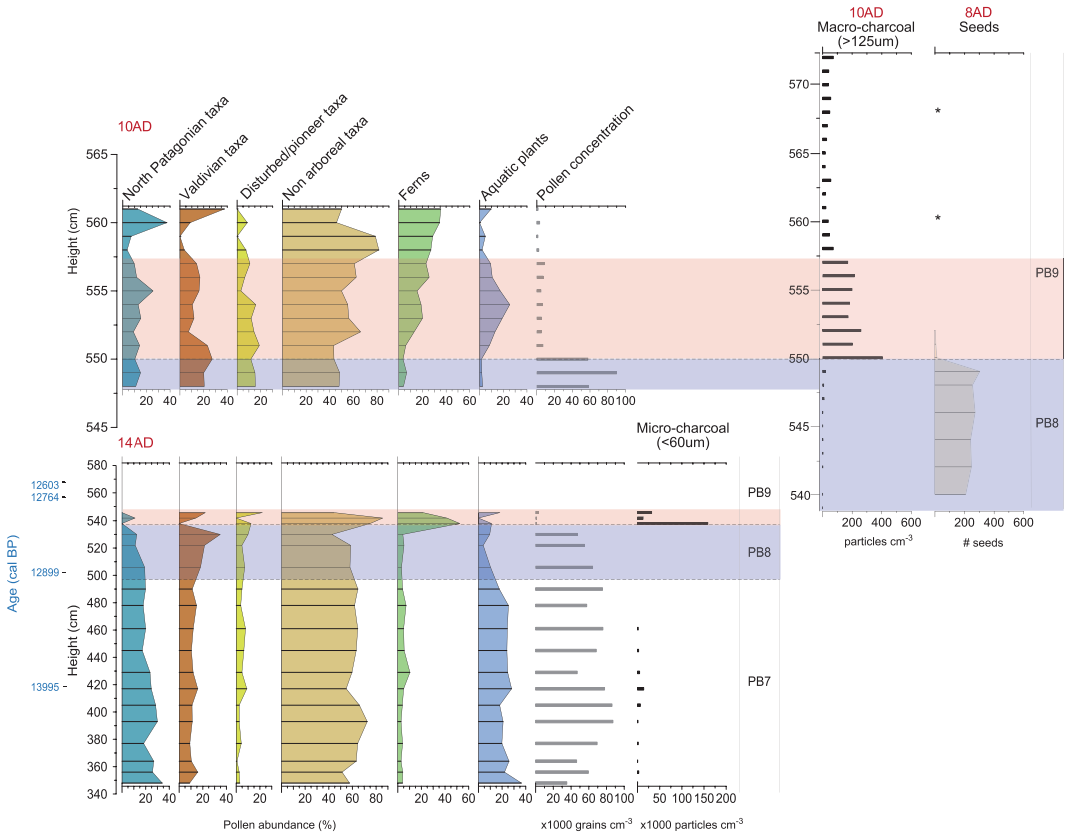

Figure 13. Records of pollen, seeds, and charcoal. (**a**) Pollen from grid 10AD, (**b**) pollen and charcoal from grid 14AD, (**c**) charcoal record from grid 10AD, (**d**) seed record collected in grid 8AD. Blue bands represent pre-YDB sediments (PB-8) and light red bands are post-YDB (PB-9) sediments. Non-arboreal taxa made up most of the local vegetation (40% to 85%). Below the YDB layer, North Patagonian taxa were dominant reflecting cooler, wetter climatic conditions. Coincident with the YDB, the North Patagonian forest elements were replaced by those of the Valdivian rainforest, marking a major shift to somewhat drier, warmer climate. Disturbed/pioneer taxa and ferns also show a dramatic increase at the beginning of the YDB layer associated with major fire regime.

the YDB layer the vegetation records show a distinct upward increase (from 5 to 20%) of pioneering/colonizing taxa indicative of more disturbed open habitats (Fig. 13)[32,77–83]. These taxa appear to have colonized the area in response to the abrupt onset of alternating seasonal drying and precipitation (humidity) that also promoted an increase in biomass burning. All of these factors indicate that the post-YDB vegetation at Pilauco is closely affiliated with the more northern Valdivian rainforest that favors seasonally drier and warmer conditions. As such, the vegetation history at Pilauco records a sudden shift at the YDB from cooler, wetter conditions characteristic of the North Patagonian forest to seasonally drier and warmer conditions of the Valdivian rainforest. Coinciding with the termination of the Antarctic Cold Reversal, this shift in vegetation at the YDB continued for at least 100 years, suggesting persistent post-YDB climate change and a disturbed landscape.

The plant and charcoal records from Pilauco are complex, but crucial for understanding regional climate change, and so, we summarize our findings here. Although most investigations in the Lake District, Chiloe Island, and Pilauco show variability among sites before, during, and after the YD Chronozone, essentially the same forest/climate succession and environmental disruption is evident among all the records across the YD boundary (e.g. Moreno *et al.*[84], and see Supplementary Information, S2 "Background: Paleoclimate and Biota", and Supplementary Table S13 for a list of investigations in the area). More research is necessary to confirm the presence of impact-related evidence at other sites in southern Chile.

Section 7: Climate change at the YDB. The high-resolution climatic record at Pilauco allows us to test the correlation of local climate at ~12,800 cal BP with similar changes across a much wider area. The result is a novel synthesis showing the onset of abrupt, coeval, pan-hemispheric climatic change. This is suggestive, but not conclusive of causation by a cosmic impact event at the YD onset, which may be represented by the recently discovered Hiawatha Crater in Greenland[25].

In southern Chile located between 40° and 44°S, colder-to-warmer and wetter-to-drier climate change at the beginning of the YD at ~12.8 ka, as discussed in the section above, has previously been documented for several sediment sections[66,80,81,84]. This change is associated with the termination of the Antarctic Cold Reversal episode, anti-phased with the shift in the Northern Hemisphere from the warm Bølling-Allerød to the colder YD. The Pilauco record shows that this climate shift occurred very rapidly within just a few years or less, based

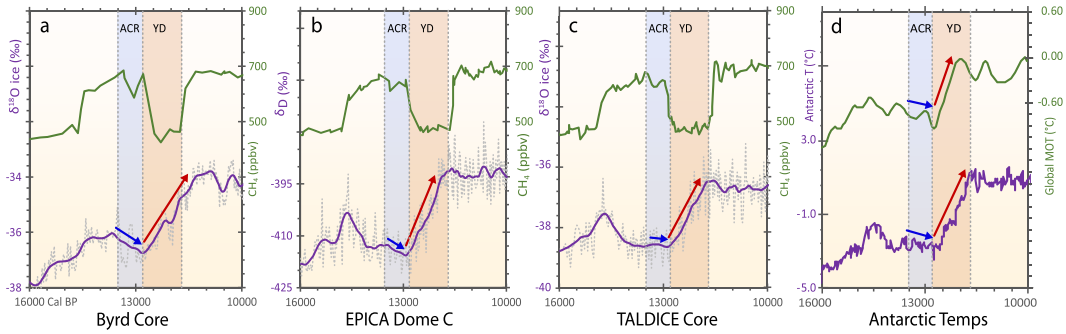

Figure 14. Antarctic climate record exhibiting warming trend at ~12,800 cal BP. Changes in methane (CH_4) concentrations are used to identify and correlate climate change boundaries representing the Antarctic Cold Reversal and the Younger Dryas. Climatic history is reflected by changes in $\delta^{18}O$ and δD values, which are proxies for temperature, with lower values indicating cooler climate. (**a**) Byrd core in West Antarctica; (**b**) EPICA Dome C near the center of East Antarctica; (**c**) TALDICE core from Talos Dome in southern East Antarctica; (**d**) green upper curve represents global mean ocean temperature from WAIS divide near Byrd in West Antarctica. Purple lower curve represents atmospheric temperatures reconstructed from CO_2 record at EPICA Dome C[140]. Blue vertical bar represents cooler climate during the Antarctic Cold Reversal, anti-phased with the warm Bølling-Allerød episode in the Northern Hemisphere. Orange vertical bar represents warmer climate in Antarctic coeval with Younger Dryas cooling in the Northern Hemisphere. Blue and red arrows indicate colder or warmer temperature changes, respectively, across the Antarctic Cold Reversal and the Younger Dryas.

on sedimentary deposition rates. It appears that the abrupt changes in southern Chilean vegetation (cool/wet North Patagonia forest to warmer/drier Valdivian rainforest), marking the YD onset and the termination of the Antarctic Cold Reversal, were caused by the abrupt southward shift of the southern westerly wind belt towards the Southern Ocean and Antarctica[66,80,81,84].

The changes in Southern Chilean climate at the YD onset are broadly similar to other changes described at high southern latitudes. Evidence includes well-dated $\delta^{18}O$ and δD proxy climate records in Antarctic ice cores (Byrd Station[85]; EPICA Dome C[86,87]; and TALDICE[88,89]), as well as Vostok[90]; EPICA Dome ML[91,92]; and Taylor Dome[93]. This change is confirmed by a reconstruction of Antarctic atmospheric temperatures at EPICA Dome C[86,87]. As at Pilauco, these records exhibit an abrupt cold-to-warm climate shift at ~12.8 ka, representing the end of the Antarctic Cold Reversal (Fig. 14).

The cold-to-warm climatic shift recorded in the YDB layer in southern Chile sharply contrasts with the warm-to-cold shift that sometimes occurred at the YD onset in the Northern Hemisphere[94–96]. This differing climatic response between the Southern and Northern Hemispheres at the YD onset appears to have been prompted by two synergistic processes[97] associated with anti-phased, bipolar, climate shift (meridional seesaw effect)[94–96], resulting in immediate corresponding climate responses via the atmosphere, rather than slower responses through oceanic processes. Possible contributing mechanisms include dramatic outburst flooding from destabilized ice sheets and proglacial lakes at the YD onset in the Northern Hemisphere[4,98–101] that injected massive quantities of meltwater and ice into the adjacent Arctic and North Atlantic Oceans, thus reducing sea surface salinities and expanding sea-ice across the Arctic and high latitudes of the North Atlantic. This, in turn, strongly reduced North Atlantic meridional overturning circulation and curtailed production of North Atlantic Intermediate Waters, further strengthening cooling and sea-ice expansion in the Northern Hemisphere. This major change in circulation in the Northern Hemisphere helped to stimulate Antarctic deep-water production in the Southern Hemisphere and its northward expansion in the world's oceans. The abrupt YD cooling episode in the Northern Hemisphere, in turn, prompted changes in global atmospheric telecommunication represented by a sequence of southward shifts in the zonal wind systems in response to the changes in sea-surface temperature gradients.

The Inter Tropical Convergence Zone (ITCZ) is a belt of low pressure which circles the Earth, generally where the trade winds of the Northern and Southern Hemispheres come together near the equator. During climatic transitions of the late Quaternary, tight coupling is known to have existed between the southern margin of the ITCZ and the southern westerly winds[97,102,103]. At the onset of the YD, the ITCZ was pushed southwards farther into the Southern Hemisphere, and this, in turn, resulted in extreme southward displacement of the southern westerlies[97], as reflected in southern Chilean sequences, including Pilauco. This is an important process, because changes in the latitudinal position and strength of the southern westerlies strongly affect ocean circulation in the Southern Hemisphere and strengthen warming south of 35°S[97], including the Southern Ocean and Antarctica. At the onset of the YD, this was reflected by a reduction in sea ice extent and increased wind-driven upwelling and ocean overturning[97]. In turn, this led to the increased release of carbon from the deep ocean, to outgassing of CO_2 into the atmosphere due to Southern Ocean upwelling, and to a rise in atmospheric pCO_2. It is also possible that these changes led to increased production of Antarctic Bottom Water at the YD onset, coeval with a major decrease in North Atlantic meridional overturning circulation (the ocean conveyor).

The YD onset is also dramatically and enigmatically marked by an abrupt rise in mean ocean temperatures in both hemispheres that continued for ~700 years[104] (Fig. 14d). This unprecedented ocean warming episode required massive oceanic energy uptake of ~10^{21} joules per year, representing the fastest and strongest global

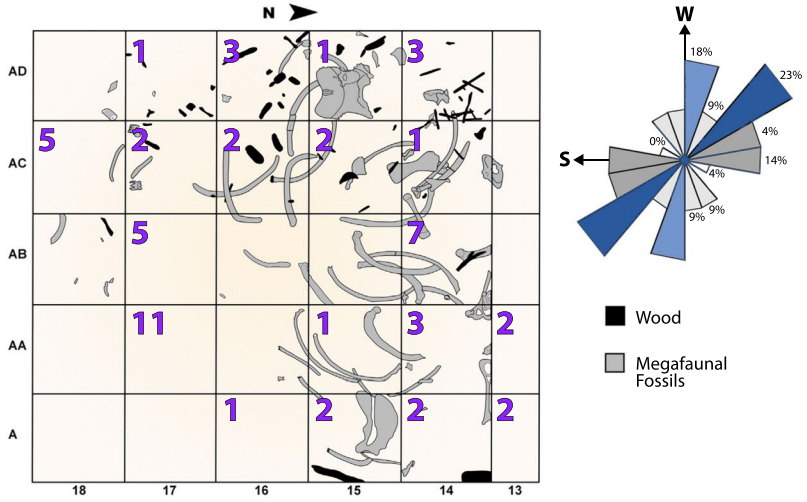

Figure 15. Grid map of megafaunal (proboscidean) bone and human lithic distributions. Bones (gray) mapped during the excavation are oriented to the SW-NE (23%) and SSW-NNE. Orientation of the proboscidean bones suggests the animals died *in situ*. Carnivores were possibly responsible for alteration and/or removal of some bones. Purple numbers represent the quantity of human lithics found in each grid. There is no current evidence that humans modified the bones, although the presence of numerous closely associated lithics suggests significant human interaction with the extinct proboscidean remains.

ocean warming episode of at least the last 22,000 years, the limit of the record investigated[104] and surpassing modern multi-decadal warming trends recorded from 1971 to 2005[104]. The rapidity and magnitude of this ocean warming episode during the early and middle YD is difficult to explain[104], but may be related to the impact into the Greenland ice sheet that created the Hiawatha crater[25], possibly at ~12,800 cal BP. This warming trend is just one of multiple extreme characteristics marking the YD episode. It is possible that the warming at high southern latitudes, resulting from the southward shift of the southern westerly winds and the South Pacific Tropical High, contributed to the major increase in heat transfer necessary to significantly warm the deep Southern Ocean, which in turn, would have reduced sea ice extent, as well as stimulated ocean turnover and production of deep waters. The loci of Antarctic deep water production likely shifted to the north in the warmer, ice-free, open Southern Ocean, where the production of warmer deep waters would have been dominated by open-ocean convection processes[105]. This shift would have enhanced heat transfer to the deep Southern Ocean, especially in absence of North Atlantic Deep Water formation, and may help explain the major, highly unusual rapid increase in mean ocean water temperatures for 700 years during the early and middle YD[104].

The evidence suggests that a seemingly enigmatic chain of interconnected oceanic and atmospheric circulation changes caused the YD climatic episode to be expressed simultaneously in both the Northern and Southern Hemispheres. These changes were marked by anomalous timing and by the character and magnitude of changes in continental meltwater plumbing, accompanied by major shifts in atmospheric and oceanic circulation. We posit that the YDB cosmic impact event, possibly resulting in the Hiawatha Crater, triggered these processes and that they appear less enigmatic in the context of a cosmic impact triggering mechanism.

The boundary between the warm Bølling-Allerød climatic episode (14,500 to 12,800 cal BP) and the subsequent cold YD episode in the Northern Hemisphere precisely correlates with anti-phased climate change in the Southern Hemisphere. This boundary in the Southern Hemisphere, as well documented at Pilauco, represents a useful isochronous datum for intercontinental correlation and dating of deglacial sequences[35]. The YDB datum layer, regardless of its origin, allows precise interhemispheric correlation of climate change at ~12,800 cal BP.

Section 8: Human-megafaunal interactions at Pilauco. Five of the 40 1-m^2 excavated grids produced 140 human lithics, including unifacial artifacts, flakes, and small pieces of debitage[34], the latter accounting for the highest percentage (75%) with cores and edge-trimmed artifacts representing 12% and 13% of the total, respectively (Fig. 15). Most artifacts and flakes were found in unit PB-7 between a height of 361 and 424 cm in grids adjacent to or including bones of gomphotheres (elephant-like proboscideans) (cf. *Notiomastodon platensis*). Obsidian and dacitic glass micro-debitage are also found in these same areas. Concentrations of aphanitic and vitreous lithic materials also coincide with areas containing abundant ribs and long bones of gomphotheres[27,34]. Investigators also found a human footprint associated with the megafaunal remains in unit PB-7[30] and a manually perforated seed that was most likely used as an ornament[27]. For more on human-related lithics, see Supplementary Information, S4.

Lithics produced by the first human settlers at Pilauco are only found in close association with megafaunal remains. This observed connection suggests that humans were exploiting extinct megafauna through scavenging and/or hunting. No human artifacts were found after the extinction of the megafauna at the YDB layer and PB-8/PB-9 boundary. This absence of remains suggests that humans either abandoned the area after the megafaunal

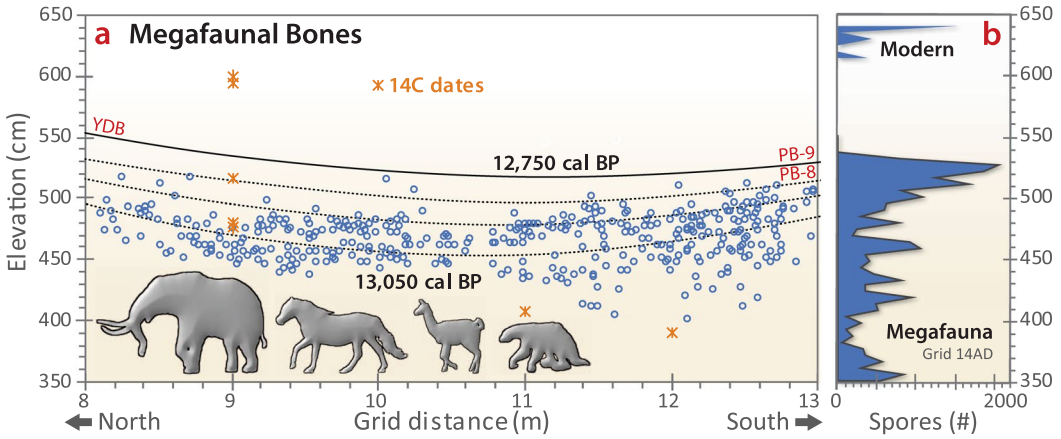

Figure 16. Stratigraphic distribution of megafaunal bones and *Sporormiella* spp. dung fungi spores. (**a**) Fifty-year-spaced isochrons for several grids across the excavation site are based on a Bayesian age-height model. The ~12,750-year isochron represents the YDB layer at the boundary between units PB-8 and PB-9. Extinct megafaunal remains were found below that isochron, with only non-extinct taxa found above. Data on stratigraphic locations of megafaunal remains are from Recabarren *et al.*[121]; Pino *et al.*[27]; and Labarca *et al.*[29]. (**b**) Biostratigraphy of *Sporormiella* spp. spores: A major peak in *Sporormiella* spp. concentration is shown at the YDB layer and immediately below after which *Sporormiella* spp. abruptly disappears from the record for hundreds of years. *Sporormiella* spp. in sediments from the uppermost part of the section are inferred to be associated with extant megafauna such as the guanaco (Camelidae) and huemul (Cervidae).

extinctions and/or experienced a regional population decline and/or reorganization, similar to that proposed for North America[106].

Section 9: Spores of *Sporormiella* spp. (dung fungi). The Pilauco site is best known for its late Pleistocene megafaunal fossil assemblage that exhibits extinctions of a number of these taxa[27]. To enhance our biostratigraphic investigation of the Pilauco megafauna and their extinctions, we quantified the vertical distribution in these sediments of coprophilous fungi spores (e.g., *Sporormiella* spp., *Sordaria* spp., and *Posospora* spp.). These spores are commonly found in the faeces of livestock, such as cows and horses, as well as in that of extinct megaherbivores such as mammoths, ground sloths, and horses[13,107]. Experimental research with modern bison populations demonstrates that *Sporormiella* spp. spore concentrations are a reliable local-scale proxy of megaherbivore population sizes[108] and are widely used in studies of extinct megafauna[109,110]. The correlation between extinct megaherbivore dung and *Sporormiella* spp. spores was established after the discovery of a layer of fossilized mammoth dung in Bechan Cave, Utah[109,110]. Variations in abundance of these coprophilous fungi in Pleistocene- and Holocene-aged sediments are considered to be directly proportional to the local abundance of megaherbivores, and thus to provide a reliable indicator of the presence, relative abundance, decline, and extinction of megafauna populations on several continents[108–115].

At Pilauco, the sediment layers below the YDB (units PB-7 and PB-8) contain persistent but variable concentrations of *Sporormiella* spp. spores in association with common megafaunal bones (Fig. 16a). Maximum concentrations of *Sporormiella* spp. spores were found in the lower part of unit PB-7 (1,540 spores cm^{-3}) at ~16,500 cal BP (Fig. 16b) and in the upper part of unit PB-8 (1,800 spores cm^{-3}), which is immediately below the YDB layer (PB-8/PB-9 boundary). Above this boundary, *Sporormiella* spp. spores abruptly disappear from the record, indicating a major megafaunal population decline or extinction. Spores reappear in much lower numbers hundreds of years later near the top of unit PB-9 most likely caused by an inferred influx of modern herbivorous fauna such as *Lama guanicoe*, *Hippocamelus bisulcus*, and *Pudu puda*.

The large peak of *Sporormiella* spp. spores, followed by their abrupt disappearance, suggests that extinct megafaunal populations were large and robust just prior to the YD onset, after which they abruptly disappeared. This suggests a possible causal connection between the megafaunal extinction and the cosmic-impact event. Records of dung fungi from North America appear more equivocal (e.g., Gill *et al.*[108] and references therein) with limited regional megafaunal extirpations and possibly even extinctions underway prior to the YD onset.

Section 10: Megafaunal Extinctions. *Megafaunal extinction record in southern South America.* Prior to the Pleistocene, several confirmed impact events are known to have been associated with megafaunal extinctions across South America (Supplementary Information, S5), although it should be noted that not all known impacts caused extinctions. For the late Pleistocene extinctions, the extent and magnitude are not particularly well known but are the subject of continuing investigations[116–119]. Altogether, South America lost more Pleistocene genera (~52) and species (~66) than North America, Europe, or Asia and it is also known that the majority of these extinctions occurred during a relatively brief interval close in age to the Allerød/YD boundary. Villavicencio[119], for example, suggested that >80% of South American mammals over 44 kg became extinct close to the onset of the YD, although several studies have reported that members of some extinct species lingered on for several thousand years before finally becoming extinct[17,117,118]. For the southern Patagonian region, radiocarbon ages

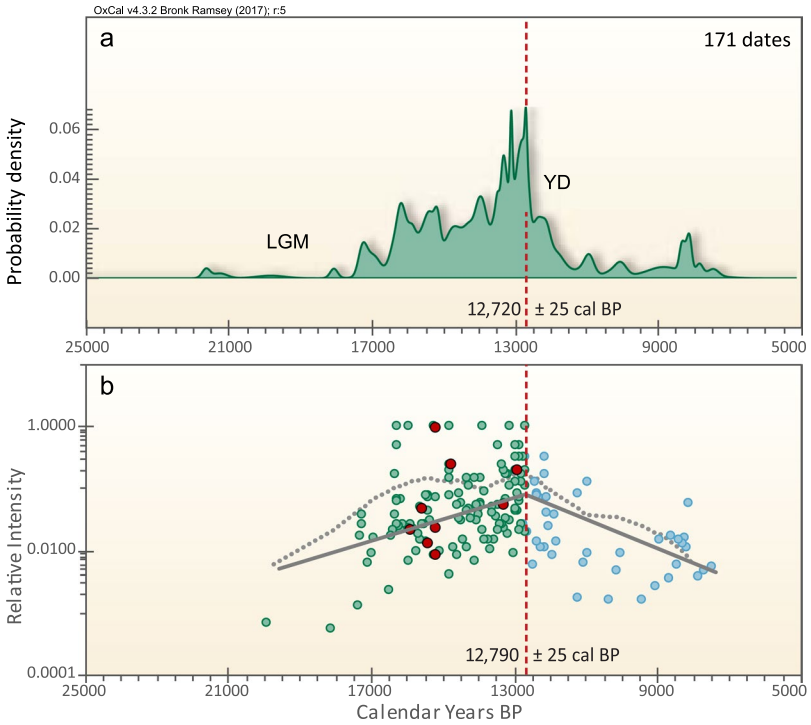

Figure 17. Statistical analyses of megafaunal radiocarbon dates. (**a**) Summed probability for 171 previously reported radiocarbon dates on megafaunal remains mostly from southern Chile and Argentina. The highest peak in stacked radiocarbon dates occurs at ~12,720 ± 25 cal BP, immediately below the YDB impact layer. (**b**) Spacing analysis of the same 171 radiocarbon dates, clustering at ~12,790 ± 25 cal BP. Gray trend line represents a linear regression, and the light gray dotted line represents lowess smoothing of the data. Green circles are pre-YDB in age and blue circles are post-YDB. Both trend lines indicate a general increase in numbers of radiocarbon dates from ~16,000 to ~12,800 cal BP, followed by a conspicuous decline in the number of dates, which is inferred to represent a major decline in megafaunal populations. The large peak in both plots at ~12,800 cal BP appears to be the time at which the YDB cosmic impact abruptly triggered large megafauna declines, including extinctions and extirpations of many taxa, later followed by full extinction of the remaining taxa.

of five megafaunal taxa, with relatively continuous biostratigraphic records, suggest an end-extinction close to ~12,500 cal BP, which is a few hundred years younger than the YD onset[120]. At Pilauco, we investigated how the extinction record compares with that for the rest of southern South America, as well as that for North America.

Megafaunal extinctions at Pilauco. Pino *et al.*[27] reported 112 bones, representing a minimum of eight extinct megafaunal taxa (Figs 15 and 16a), including the gomphothere (cf. *Notiomastodon platensis*), American horse (*Equus* (*Amerhippus*) *andium*), one sloth (*Xenarthra* indet.), and one camelid (cf. *Hemiauchenia paradoxa*)[27,29,31,33,121]. Most of these megafaunal bones were found in unit PB-7, while the overlying unit PB-8, immediately below the YDB layer, contains only extinct horse remains. For example, a coprolite from an extinct horse was found in unit PB-8 a few cm below the YDB layer and has a calibrated age range of 13,065–12,749 cal BP (mean age of 12,907 ± 158 cal BP; 11,004 ± 186 ^{14}C years BP)[27].

Distinctly fewer megafaunal bones occur in the uppermost levels of unit PB-8 (Fig. 16a), which at face value, suggests a decline in megafauna populations during the ~100-yr interval prior to the YD onset at ~12,750 cal BP. Concentrations of *Sporormiella* spp. spores, however, show no comparable decline (Fig. 16b), but instead exhibit the highest spore concentrations in the record before disappearing at ~12,750 cal BP, as has been found at other sites across the Americas[110]. This result suggests that extinct megafauna remained continuously abundant at Pilauco right up to their local extinction, coincident with the YD onset (Fig. 17). Villavicencio *et al.*[119] reported that 93% of the dates on megafaunal remains (n = 62 of 67) are either older than or fall within the age range of the YDB impact event at 95% certainty (12,835 to 12,735 cal BP[35]). These extinct taxa include ground sloth (Mylodontidae), American horse (Equidae), saber-toothed cat (Felidae), jaguar (Felidae), bear (Ursidae), fox (Canidae), and several camelids.

Megafaunal extinctions across southern South America. We analyzed 171 previously reported radiocarbon dates of extinct late Pleistocene megafaunal fossils from across southern Chile and Argentina using two statistical techniques, summed probability analysis[106] and spacing analysis[122]. Both techniques assume that the number of radiocarbon dates increases or decreases in direct correlation with increases or decreases in size of extinct megafaunal populations. This assumption is diminished due to biases in sample collection, sample size, preservation of megafaunal remains, and variability in the accuracy and precision of the radiocarbon dates[106]. Despite

the potential biases and inaccuracies, these two statistical methods are generally accepted as providing accurate first-order approximations of long-term changes in megafaunal population sizes[106,122]. To avoid any bias due to the use of different calibration curves, we used original radiocarbon dates and calibrated them using the same southern hemispheric calibration curve, SHIntCal13, within the OxCal program version 4.3.2.

The first method, summed probability analysis, is a Bayesian analytical technique that involves calibrating megafaunal radiocarbon dates and stacking the probability ranges using the SUM algorithm in the OxCal program. Major peaks and troughs in the trends are inferred to be directly proportional to changes in megafaunal population densities[106]. The advantage of this technique is that it utilizes the entire range of uncertainties for the calibrated dates. The 171 dates from Chile and Argentina are from remains of the extinct armadillo (superorder: Xenarthra; n = 11), horse (family: Equidae; n = 27), jaguar (family: Felidae; n = 6), guanaco (family: Camelidae; n = 15), mostly mastodon-like gomphothere (order: Proboscidea: n = 11), a rhinoceros-like species (suborder: Toxodonta; n = 4), saber toothed cat (genera: Smilodon; n = 5), short-face bear (family: Ursidae; n = 1), and sloth (families: mostly Mylodontidae and Megatheriidae; n = 91).

Our results suggest that population sizes of the extinct megafauna broadly increased after ~18 ka during the Last Glacial Maximum (LGM) and continued to increase throughout the Antarctic Cold Reversal, even though temperatures were colder and seemingly less hospitable. Both the LGM and the Antarctic Cold Reversal were as cold or colder than the YD episode in the Northern Hemisphere (Fig. 17a). Megafauna populations continued with a large, conspicuous increase until ~12,720 ± 25 cal BP, when population levels abruptly plummeted by ~60% within less than a few centuries, marking the largest drop in ~22,000 years, the limit of the record. The age of the main population peak closely matches that for South American populations reported by Surovell *et al.*[122], and the population decline overlaps with the YD onset at ~12,800 cal BP[35]. Following the onset of YD climate change, the reported ages of extinct megafauna indicate that some taxa persisted at very low population levels until becoming extinct during the YD interval and early Holocene.

We also used spacing analysis for the same 171 radiocarbon dates, following the analytical method of Surovell *et al.*[122]. This second technique compiles the statistically inverted gaps or time lags between consecutive dates and infers the sizes of extinct megafaunal populations based on the assumption that wider gaps between successive dates indicate smaller populations and vice versa. The disadvantage of this approach is that it uses only mean calibrated ages without considering their inherent uncertainties. Spacing analysis shows that megafaunal populations peaked at ~12,810 to 12,780 cal BP (Fig. 17b) followed by a large abrupt decline in their populations beginning at or near the YD onset. Subsequently, small populations of some taxa persisted, also to decline and become extinct during the YD and early Holocene. These data closely match the results of the summed probability analysis, and overlap with the age range of 12,835 to 12,735 cal BP for the proposed YDB impact event.

The megafaunal extinctions were clustered at the end of the Pleistocene across several continents, although the overall pattern was complex[17,112,122]. At Pilauco, the record shows that the local extinctions coincide with the YDB layer. However, elsewhere across southern South America, there are questions whether some megafauna became extinct prior to the YD onset and whether others became extinct later in the early Holocene. In any event, the evidence at Pilauco is consistent with the hypothesis that the proposed YDB impact event contributed to the South American megafaunal extinctions.

Section 11: Impact scenario. The YDB impact event is argued to be the product of an astronomical environment that is discussed in detail in Wolbach *et al.*[2] Summarizing that discussion, astronomical discoveries over the last few decades show that mass distribution of comets appears to be disproportionately large for bodies with diameters near and up to 300 km, representing a greater hazard for Earth impacts. A 250-km comet with typical density of 0.5 g/cm^3 has 1000 times the mass of the entire current near-Earth asteroid system, so that Earth impacts from cometary material are more likely than from a similar-sized asteroid[2]. These large bodies drift into the near-Earth environment quite frequently in geological timescales, and in fact, the broad remains of two such bodies are present in the inner Solar System today. One of them, the Taurid Complex, is composed of debris from an ~100-km-wide comet that arrived at least 20,000 to 30,000 years ago from the centaur system of large comets and then, further disintegrated hierarchically in a short-period, Earth-crossing orbit[123,124]. There is a reasonable probability of one or more encounters within the last 13,000 years with debris swarms from the Taurid Complex or other large fragmented comets, and such an encounter would be hemispheric in scope, lasting for only a few hours. The resulting debris field would be a mixture of dust and larger fragments, potentially equivalent to the impact of ~1000 to 10,000 destructive airbursts, such as occurred in Tunguska, Siberia in 1908[125]. If such an event occurred at the YD onset, larger objects in the debris swarm could have created craters on land, struck the world's ice sheets, and/or impacted the world's oceans, creating severe biotic and climatic disturbances[126].

Section 12: Conclusions. The main objective of this study was to test the YDB impact hypothesis by analyzing a wide range of data from the Pilauco site in southern Chile. The following conclusions show that our data and interpretations are consistent with the YDB impact hypothesis and we found no evidence that refutes the hypothesis.

(1) At Pilauco, ~12,800-year-old peaks in high-temperature Pt-rich and native-Fe spherules are comparable to similar impact-related evidence found at more than 50 YDB sites in North America, Europe, and western Asia. It appears that the YDB layer at Pilauco is coeval with similar layers found at these sites on several continents and is also possibly related to the proposed YDB impact event.
(2) Identification of the YDB layer at Pilauco greatly expands the proposed YDB proxy field ~6,000 km farther south of the closest well-studied YDB site in Venezuela, and ~12,000 km south of the northernmost YDB site in Canada, a distance equaling ~30% of Earth's circumference.
(3) Cr-rich spherules are found in the YDB layer at Pilauco, but not found at the ~50 other sites on four

continents, suggesting that one or more local impacts/airbursts occurred in the Cr-rich basaltic terrain circa Pilauco.

(4) Unusually high Pt/Pd and Au/Pt ratios suggest the influx of non-local PGE-rich material. The presence of a significant Pt abundance peak in the YDB layer at Pilauco supports the proposition that the proposed YDB impact event was large enough to have distributed impact-related materials across both the Northern and Southern Hemispheres.

(5) The Pilauco charcoal record shows that the largest episode of biomass burning in the sedimentary sequence investigated was coeval with the widespread biomass-burning event at the YD onset, as identified in >150 ice, lake, and terrestrial records from four continents, including lakes in South America.

(6) Pollen, cuticles, and seeds records from Pilauco exhibit a large decline in abundance and diversity, and a major change in taxonomic composition of plants at the YD onset. These changes indicate there was significant environmental disruption at Pilauco, associated with abrupt climate change. Although the change in the abundance/diversity of plant taxa and fire activity recorded at the Pilauco site cannot be solely attributed to an extra-terrestrial impact, all the independent lines of evidence presented in our investigation (spherules, trace elements, fossil plants-animals, etc.) suggest that these changes may have been driven by an extra-terrestrial event.

(7) The YDB layer at Pilauco coincides precisely with the abrupt termination of cooler climate of the Antarctic Cold Reversal across southern South America and Antarctica, immediately followed by the onset of warmer conditions. Through the seesaw effect, this climatic change is anti-phased via atmospheric processes with Northern Hemisphere cooling at the YD onset.

(8) Human artifacts were found at Pilauco only below the YDB layer, suggesting a local population reorganization/decline. They were found only in association with extinct megafauna bones.

(9) At Pilauco, no bones or remains of extinct megafauna were found above the YDB proxy layer. Similarly, the record of *Sporormiella* spp. spores indicates that the local megafauna extinction was coeval with deposition of high concentrations of impact spherules and Pt, suggesting a possible causal connection to the YDB impact event.

In summary, evidence has been found in the Pilauco section that is similar to that found at >50 YDB sites on four continents. This is the first time that extensive YDB evidence has been found at high latitudes in the Southern Hemisphere. The evidence reported in this study appears consistent with the proposed effects of a YDB cosmic impact event that affected both the Northern and Southern Hemispheres.

Section 12: Methods. *Stratigraphic sampling.* A 280-cm-long, 5-cm-wide column was collected from grid 14AD that included units PB-7, PB-8, and PB-9. Later, in 2014, a 34-cm-wide column was collected from grid 10AC to develop a detailed stratigraphic sequence across the PB-8/PB-9 boundary. Grain-size analyses by wet sieving and loss-on-ignition (LOI) were performed at 1-cm intervals along both stratigraphic columns to quantify proportions of gravel, sand, mud, and organic fractions. Sedimentological sampling and analyses were performed at the Universidad Austral de Chile, Valdivia, by co-author M.P. with the assistance of Javiera Barria and Daniel Fritte. Subsequently, co-author M.P.L. developed the stratigraphic profile.

Radiocarbon dates. A total of 36 AMS radiocarbon dates were obtained for this study from bulk sediment, seeds, charcoal, wood, plant remains, bone, teeth, and coprolites (Supplementary Table S4). Samples were acquired in Chile by M.P. with the assistance of Daniel Fritte. Nine radiocarbon dates are from Pino *et al.*[27] and 27 others were obtained for this study. Twelve dates were measured by the NSF-Arizona AMS facility, University of Arizona and 24 are from the W. M. Keck Carbon Cycle Accelerator Mass Spectrometry Laboratory, University of California, Irvine. Samples for radiocarbon dating were collected from excavation grids 6E, 7AC, 7 G, E9, 10AD, 11 H, 12 F, 14AD, 15AC, and 15AD (Supplementary Figs S1–S3). Twenty AMS radiocarbon dates were outside the interval of interest, and the remaining sixteen were used to develop an age-height model (see Methods; Fig. 3; Supplementary Table S5). These dates were calibrated within the OxCal program 4.3.2[127], using the Southern Hemispheric calibration curve, SHIntCal13. Uncertainties were calculated at confidence intervals (CI) of 68% and 95%. The layer dating to ~12,800 cal BP was identified in grid 8AD at a height of ~550 cm above the site datum (elevation, not depth). Because stratigraphic heights varied by centimeters to decimeters in other grids, the YDB layer in all grids is correlated and normalized to 550 cm in grid 8AD, allowing stratigraphic and chronologic comparisons among the various proxies measured in the different grids.

Analyses of high-temperature impact spherules. Twenty-three bulk sediment samples (~1 kg each) from grid 8AD were examined across a 138-cm-thick profile that ranged in height from 651 cm at the surface to 513 cm at its deepest point. Continuous samples were taken between 572 and 524 cm, with one additional discontinuous sample each taken at the top and bottom of the section. Sample thicknesses averaged ~3 cm along the sediment profile. From 552 to 548 cm, samples were 1-cm thick. The four samples collected below and above these were 2-cm thick, and samples at the top and bottom of the profile were 4-cm thick. Samples were collected by M.P. and Daniel Fritte.

To determine the composition of spherules from Pilauco, we used scanning electron microscopy and energy dispersive x-ray spectroscopy (SEM-EDS), and ternary geochemical analyses to compare the YDB spherules from Pilauco to other known types of spherules. David Kimbel in the US extracted the magnetic fractions and Jennifer Zeldin in the US mounted candidate YDB spherules for SEM analyses. M.A.L. and V.A. performed the SEM-EDS analyses using a JEOL JSM 6010PLUS/LA at Elizabeth City State University and a Hitachi S3200N variable pressure scanning electron microscope (VPSEM) at North Carolina State University. All SEM imagery was acquired

at a resolution of 2560 × 1920 pixels. Images were uniformly post-processed for contrast and brightness, if necessary, using Adobe Photoshop CC2014.

Quantification of platinum. We used the methodology described in Moore *et al.*[45]. Sediment samples of approximately 50 grams each were collected by M.P. and Javiera Barria and then sent for analysis by Activation Laboratories (ActLabs), Canada using their "1C-Research" package. The package includes fire-assay (FA) and inductively coupled plasma mass spectrometry (ICP-MS) to measure elemental concentrations of Pt, Pd, and Au. Prior to analysis, each sample was mixed with fire assay fluxes (borax, soda ash, silica, litharge) and silver (Ag) was added as a collector. The mixture was placed in a crucible and preheated to 850 °C, intermediately heated at 950 °C, and finished at 1060 °C for a total of 60 minutes. After the crucibles were removed from the assay furnace, the molten slag was poured into a mold leaving a lead button. The lead button was then preheated to 950 °C to recover the Ag (doré bead) mixed with the extracted Au, Pt and Pd. The Ag doré bead was digested in hot (95 °C) HNO_3+HCl with a special complexing agent to prevent the Au, Pd, and Pt from adsorbing onto the test tube. After cooling for 2 hours, the sample solution was analyzed for Au, Pt, and Pd using a Perkin Elmer Sciex ELAN 9000 ICP-MS. On each tray of 42 samples there were 2 method blanks, 3 sample duplicates, and 2 certified reference materials. The ICP-MS was recalibrated every 45 samples. Smaller sample splits were used for high-chromium and sulfide samples. Measurements are reported in parts per billion (ppb) with a lower limit of detection for Pt of 0.1 ppb. All control testing indicated that the analyses were accurate and replicable.

Analyses of plant remains. The same 138-cm-thick profile examined for the presence of impact spherules in grid 8AD was also investigated for plant remains (fruits, seeds, capsules, cuticles). Sediment samples were collected and analyzed by M.P., Daniel Fritte, and Javiera Barria. The sediment samples were wet sieved through a series of sieves (2 mm to 63 μm) for the separation of gravel, sand, and mud. Next, the fractions were oven-dried at 60 °C, dry weighed, and stored in plastic bags for further examination. The fractions from each sample were examined under a stereomicroscope at 10 × to 40 × magnification for the picking and sorting of reproductive structures (i.e., seeds, fruits and capsules; hereinafter referred to as seeds) and leaf cuticles. Plant remains were analyzed by G.A. at the Universidad Austral de Chile, in Valdivia.

Numerical analyses were performed only on the seed data because of the high fragmentation of cuticle remains and uncertainty in knowing the number of individual leaves from which the cuticle fragments were derived. We tested whether variation of our count response variable (number of seeds) for units PB-8 and PB-9 was affected by different sample sizes (thickness and/or total weight of the sample). To do so, we fitted a Poisson GLM regression, in which the dependent variable is allowed to have a non-normal distribution. This regression holds that any observed response is a linear sum of multiple underlying individual responses. Because we detected over-dispersion (greater than expected variance from the mean), a correction of the standard errors was performed using a quasi-GLM model specifying the mean and variance relationship (i.e., variance given by $\varphi \times \mu$, where μ is the mean and φ the dispersion parameter), following the method of Zuur *et al.*[128]. Finally, we fitted a negative binomial GLM and compared the two approaches by using the log-likelihoods of the negative binomial regression model and a Poisson regression model using the odTest function of the 'pscl' package in R. All analyses were conducted in R[129].

Analyses of pollen. For quantification of pollen grains and spores, we analyzed 13 contiguous samples of 1 cm^3 (548 to 561 cm height) near the PB-8/PB-9 boundary in grid 10AD following the standard palynological procedures outlined by Faegri and Iversen[130]. Pollen samples were analyzed by co-authors, A.M.A. and A.M-C. at the Universidad Austral de Chile in Valdivia. Chemical treatment included deflocculation with 10% KOH, sieving to remove large debris (150 μm), silicate dissolution with 40% hydrofluoric acid (HF), acetolysis with 10% KOH, and concentrated HF and acetolysis. The concentrates were mounted in glycerin and analyzed at 400× and 1000× with a Zeiss microscope. Taxonomical determinations were made based on published descriptions[131], and modern pollen reference collections held at the Palynology and Environmental reconstructions laboratory, Universidad Austral de Chile. From each slide, a minimum of 300 pollen grains from terrestrial taxa were counted, and concentrations were calculated based on *Lycopodium* spores added to the preparations. Percentages of pollen abundances are based on the total sum of pollen. Pollen diagrams and cluster analysis (CONISS) were produced using the software Tilia[132,133].

Analyses of charcoal. To investigate the biomass-burning history of the Pilauco section, we performed macroscopic charcoal analysis on samples from a 38-cm-long profile including the PB-8/PB-9 boundary in grid 10AD, located on the west wall of the site. We analyzed 2 cm^3 of sediment taken at contiguous 1-cm intervals along the complete section. The samples were sieved using the methods outlined by Whitlock and Larsen[134]. The charcoal fractions (>0.125 mm) were counted in gridded Petri dishes under a stereomicroscope and expressed as charcoal concentrations (particles cm^{-3}). Charcoal samples were analyzed by A.M.A. and A.M-C. at the Universidad Austral de Chile in Valdivia.

Analysis of Sporormiella spp. fungi spores. Counts of *Sporormiella* spp. spores were performed in 76 of the pollen preparations[32] from a stratigraphic section in grid 14AD that includes units PB-7, PB-8, and PB-9. A magnification of 400× was used, and added *Lycopodium* spores were used to calculate concentrations. The determination of *Sporormiella* spp., characterised by its sigmoidal germinal opening and dark brown color, was performed using keys, photographs, and morphological descriptions (cf. refs[135–138]). Spores were analyzed by N.C-M. at the Universidad Austral de Chile in Valdivia.

Statistical analyses of megafaunal remains. Spacing analysis was used to investigate the gaps or time lags between consecutive calibrated radiocarbon dates. This technique assumes that mean spacings between calibrated ages are inversely proportional to the size of extinct megafaunal populations (i.e., smaller intervals mean larger populations). To avoid inaccuracies introduced by the use of multiple calibration curves, we did not use calibrated dates from the original studies. Instead, co-author A.W. recalibrated all original radiocarbon dates with the OxCal program, version 4.3.2[127], using SHCal13, the radiocarbon calibration curve for the Southern Hemisphere. After inverting the age intervals to identify the point at which the megafaunal populations began to decrease before full extinction, we used linear regression with breakpoints, estimated through lowess smoothing. The sources of 171 radiocarbon dates are, n = 6 this study; n = 24 from Araújo *et al.*[139], n = 3 from Pino *et al.*[27], n = 47 from Prado *et al.*[140], n = 27 from Surovell *et al.*[122], and n = 64 from Villavicencio *et al.*[119]. Duplicates were eliminated. The dates were ranked in quality from 11 to 17 by the original authors based on multiple factors (e.g., the kind of material dated, the association of the dated material with the taxon or event that was being dated, and the method of dating (AMS or standard)). Dates lower than the rank of 11 were excluded from this study because, as suggested by Barnosky and Lindsey[118], lower-ranked dates are considered to be insufficiently robust. Megafaunal remains were excavated and analyzed under the supervision of M.P. at the Pilauco Lab and at the Universidad Austral de Chile in Valdivia.

Summed probability analyses. We followed the Bayesian technique from Anderson *et al.*[106] that involves calibrating megafaunal radiocarbon dates and stacking the probability ranges using the SUM algorithm in OxCal v. 4.3.2. Major peaks and troughs are inferred to represent changing megafaunal population densities, i.e., greater numbers of dates are inferred to reflect larger populations, with fewer dates indicating smaller populations[106]. The advantage of this technique is that it relies on the entire range of uncertainties for the calibrated dates.

Data Availability

all relevant data are available in this contribution. Sedimentary sample aliquots are available from Mario Pino, email: mariopino@uach.cl.

References

1. Firestone, R. B. *et al.* Evidence for an extraterrestrial impact 12,900 years ago that contributed to the megafaunal extinctions and the Younger Dryas cooling. *Proc Nat Acad Sci* **104**, 16016–16021 (2007).
2. Wolbach, W. S. *et al.* Extraordinary biomass-burning episode and impact winter triggered by the Younger Dryas cosmic impact <12,800 years ago. 1. Ice cores and glaciers. *J Geol* **126**, 165–184 (2018).
3. Wolbach, W. S. *et al.* Extraordinary biomass-burning episode and impact winter triggered by the Younger Dryas cosmic impact <12,800 years ago. 2. Lake, marine, and terrestrial sediments. *J Geol* **126**, 185–205 (2018).
4. Kennett, J., Kennett, D., LeCompte, M. & West, A. In *Potential consequences of the YDB cosmic impact at 12.8 ka*, *in Early human life on the southeastern coastal plain*. (eds Goodyear, A. C. & Moore, A. M.) (University Press of Florida, 2018).
5. Mahaney, W. C. Evidence from the northwestern Venezuelan Andes for extraterrestrial impact: The black mat enigma. *Geomorphology* **116**, 48–57 (2010).
6. Mahaney, W. C., Krinsley, D. & Kalm, V. Evidence for a cosmogenic origin of fired glaciofluvial beds in the northwestern Andes: Correlation with experimentally heated quartz and feldspar. *Sediment Geol* **231**, 31–40 (2010).
7. Mahaney, W. C., Krinsley, D. H., Milner, M. W., Fischer, R. & Langworthy, K. Did the Black-Mat Impact/Airburst Reach the Antarctic? *Evidence from New Mountain Near the Taylor Glacier in the Dry Valley Mountains.* **126**, 285–305 (2018).
8. Kennett, D. J. *et al.* Nanodiamonds in the Younger Dryas boundary sediment layer. *Science* **323**, 94 (2009).
9. Melott, A. L., Thomas, B. C., Dreschhoff, G. & Johnson, C. K. Cometary airbursts and atmospheric chemistry: Tunguska and a candidate Younger Dryas event. *Geology* **38**, 355–358 (2010).
10. Israde-Alcántara, I. *et al.* Evidence from central Mexico supporting the Younger Dryas extraterrestrial impact hypothesis. *Proc Nat Acad Sci* **109**, E738–E747 (2012).
11. Kinzie, C. R. *et al.* Nanodiamond-rich layer across three continents consistent with major cosmic impact at 12,800 cal BP. *J Geol* **122**, 475–506 (2014).
12. LeCompte, M. *et al.* In *Brief Overview of the Younger Dryas Cosmic Impact Datum Layer 12,800 Years Ago and Its Archaeological Utility in Early Human Life on the Southeastern Coastal Plain* (eds Goodyear, A. C. & Moore, A. M.) 155–174 (University Press of Florida, 2018).
13. Boslough, M. *et al.* In *Arguments and evidence against a Younger Dryas impact event in Climates*, *landscapes*, *civilizations*, *Geophysical Monograph Series* Vol. 198 (eds Giosan, L. *et al.*) 13–26 (Am Geophys Union, 2013).
14. Meltzer, D. J., Holliday, V. T., Cannon, M. D. & Miller, D. S. Chronological evidence fails to support claim of an isochronous widespread layer of cosmic impact indicators dated to 12,800 years ago. *Proc Nat Acad Sci* **111**, E2162–E2171 (2014).
15. Holliday, V., Surovell, T. & Johnson, E. A blind test of the Younger Dryas impact hypothesis. *PloS One* **11**, e0155470 (2016).
16. Meltzer, D. J. & Holliday, V. T. Would North American Paleoindians have noticed younger Dryas age climate changes? *J World Prehist* **23**, 1–41 (2010).
17. Stuart, A. J. Late Quaternary megafaunal extinctions on the continents: a short review. *Geol J* **50**, 338–363 (2015).
18. Holliday, V. T., Surovell, T., Meltzer, D. J., Grayson, D. K. & Boslough, M. The Younger Dryas impact hypothesis: a cosmic catastrophe. *J Quat Sci* **29**, 515–530 (2014).
19. Marlon, J. R. *et al.* Wildfire responses to abrupt climate change in North America. *Proc Nat Acad Sci* **106**, 2519–2524 (2009).
20. Bunch, T. E. *et al.* Very high-temperature impact melt products as evidence for cosmic airbursts and impacts 12,900 years ago. *Proc Nat Acad Sci* **109**, E1903–E1912 (2012).
21. Kurbatov, A. V. *et al.* Discovery of a nanodiamond-rich layer in the Greenland ice sheet. *J Glaciol* **56**, 747–757 (2010).
22. Schulte, P. *et al.* The Chicxulub asteroid impact and mass extinction at the Cretaceous-Paleogene boundary. *Science* **327**, 1214–1218 (2010).
23. Adatte, T. *et al.* Late Maastrichtian and K/T paleoenvironment of the easternTethys (Israel): mineralogy, trace and platinum group elements, biostratigraphy and faunal turnovers. *Bulletin de la Société Géologique de France* **176**, 37–55 (2005).
24. Wasson, J. T. Large aerial bursts: an important class of terrestrial accretionary events. *Astrobiology* **3**, 163–179 (2003).
25. Kjær, K. H. *et al.* A large impact crater beneath Hiawatha Glacier in northwest Greenland. *Sci Adv* **4**, https://doi.org/10.1126/sciadv.aar8173%JScienceAdvances (2018).
26. Petaev, M. I., Huang, S., Jacobsen, S. B. & Zindler, A. Large Pt anomaly in the Greenland ice core points to a cataclysm at the onset of Younger Dryas. *Proc Nat Acad Sci* **110**, 12917–12920 (2013).
27. Pino, M., Chávez-Hoffmeister, M., Navarro-Harris, X. & Labarca, R. The late Pleistocene Pilauco site, Osorno, south-central Chile. *Quat Int* **299**, 3–12 (2013).

28. Pino, M., Martel-Cea, A., Vega, R., Fritte, D. & Soto-Bollmann, K. In *Geología y geomorfología del sitio Pilauco in El Sitio Pilauco. Osorno, Patagonia Noroccidental de Chile*. 12–46 (Universidad Austral de Chile Valdivia, Chile, 2016).
29. Labarca, R., Recabarren, O. P., Canales-Brellenthin, P. & Pino, M. The gomphotheres (proboscidea: Gomphotheriidae) from Pilauco site: Scavenging evidence in the Late Pleistocene of the Chilean Patagonia. *Quat Int* **352**, 75–84 (2014).
30. Macias, C. M., Moreno, K. & Pino, M. In *Una icnita humana del Pleistoceno tardío, sitio arqueo-paleontológico Pilauco, Región de Los Lagos, Osorno, Chile in II Simposio Latinoamericano de Icnología*. 43 (2013).
31. Recabarren, O. P., Pino, M. & Alberdi, M. T. La Familia Gomphotheriidae en América del Sur: evidencia de molares al norte de la Patagonia Chilena. *Estud Geol* **70**, e001 (2014).
32. Abarzúa, A. M., Lobos, V. & Martel-Cea, A. In *¡Pequeño testigo de grandes cambios!: polen, semillas y carbones escondidos en Pilauco in El Sitio Pilauco, Osorno, Patagonia Noroccidental de Chile*. (ed. Pino, M.) 112–127 (Universidad Austral de Chile, TAQUACH., 2016).
33. Encina, R. L., Pino, M. & Recabarren, O. Los Lamini (Cetartiodactyla: Camelidae) extintos del yacimiento de Pilauco (Norpatagonia chilena): aspectos taxonómicos y tafonómicos preliminares. *Estud Geol* **69**, 255–269 (2013).
34. Navarro-Harris, X. *et al.* The procurement and use of knappable glassy volcanic raw material from the late Pleistocene Pilauco site, Chilean Northwestern Patagonia. *Geoarchaeology* (in press) (2018).
35. Kennett, J. P. *et al.* Bayesian chronological analyses consistent with synchronous age of 12,835-12,735Cal B.P. for Younger Dryas boundary on four continents. *Proc Nat Acad Sci* **112**, E4344–4353 (2015).
36. Porter, S. C. Pleistocene glaciation in the southern Lake District of Chile. *Quat Res* **16**, 263–292 (1981).
37. Luebert, F. & Pliscoff, P. *Sinopsis bioclimática y vegetacional de Chile*. 316 (Editorial Universitaria, 2006).
38. Perez, Y. *et al. Geología para el ordenamiento territorial: Área de Osorno, Región de los Lagos*., (Servicio Nacional de Geología y Minería., 2003).
39. Boëda, E. *et al.* The late-Pleistocene industries of Piauí, Brazil: new data. *Paleoamerican Odyssey*, 445–465 (2013).
40. Haynes, C. V. Younger Dryas "black mats" and the Rancholabrean termination in North America. *Proc Nat Acad Sci* **105**, 6520–6525 (2008).
41. Quade, J., Forester, R. M., Pratt, W. L. & Carter, C. Black mats, spring-fed streams, and late-glacial-age recharge in the southern Great Basin. *Quat Res* **49**, 129–148 (1998).
42. Harris-Parks, E. The micromorphology of Younger Dryas-aged black mats from Nevada, Arizona, Texas and New Mexico. *Quat Res* **85**, 94–106 (2016).
43. Haynes, C. V. *et al.* TheMurray Springs Clovis site, Pleistocene extinction, and the question of extraterrestrial impact. *Proc Nat Acad Sci* **107**, 4010–4015 (2010).
44. LeCompte, M. A. *et al.* Independent evaluation of conflicting microspherule results from different investigations of the Younger Dryas impact hypothesis. *Proc Nat Acad Sci* **109**, E2960–2969 (2012).
45. Moore, C. R. *et al.* Widespread platinum anomaly documented at the Younger Dryas onset in North American sedimentary sequences. *Sci Rep* **7**, 44031, https://doi.org/10.1038/srep44031 (2017).
46. Wittke, J. H. *et al.* Evidence for deposition of 10 million tonnes of impact spherules across four continents 12,800 y ago. *Proc Nat Acad Sci* **110**, E2088–E2097 (2013).
47. Andronikov, A. V. *et al.* Implications from chemical, structural and mineralogical studies of magnetic microspherules from around the lower Younger Dryas boundary (New Mexico, USA). *Geogr Ann A* **98**, 39–59 (2016).
48. GERM. In *Geochemistry for the Element of Ni (Nickel), Geochemical Earth Reference Model* (ed GERM) (EarthRef.org, 2017).
49. Wright, F. W. & Hodge, P. W. Studies of particles for extraterrestrial origin: 4. *Microscopic spherules from recent volcanic eruptions. J Geophys Res* **70**, 3889–3898 (1965).
50. Deb, M. & Sarkar, S. C. In *Minerals and Allied Natural Resources and their Sustainable Development* 29–139 (Springer, 2017).
51. Rutherford, M. J. & Devine, J. D. III In *Magmatic conditions and processes in the storage zone of the 2004–2006 Mount St. Helens dacite in A volcano rekindled: the renewed eruption of Mount St. Helens, 2004–2006 (Professional Paper 1750)* (eds David, R. S., William, E. S. & Peter, H. S.) Ch. 31, 23 (US Geological Survey, 2008).
52. Kracek, F. C. Melting and transformation temperatures of mineral and allied substances. *Geol Soc Am, Special Papers* **36**, 139–174 (1942).
53. McEwan, N., Courtney, T., Parry, R. A. & Knupfer, P. Chromite—A cost-effective refractory raw material for refractories in various metallurgical applications. *Southern African Pyrometallurgy*, 359–372 (2011).
54. Heiken, G. Morphology and petrography of volcanic ashes. *Geol Soc Am Bull* **83**, 1961–1987 (1972).
55. Smit, J. Meteorite impact, extinctions and the Cretaceous-Tertiary boundary. *Geol Mijnbouw* **69**, 187–204 (1990).
56. Goddu, S. R., Appel, E., Jordanova, D., Wehland, F. & Parts, A. Magnetic properties of road dust from Visakhapatnam (India)—relationship to industrial pollution and road traffic. *Phys Chem Earth BC* **29**, 985–995 (2004).
57. Puffer, J. H., Russell, E. W. B. & Rampino, M. R. Distribution and origin of magnetite spherules in air, waters, and sediments of the greater New York City area and the North Atlantic Ocean. *J Sediment Res* **50** (1980).
58. Pinter, N. *et al.* The Younger Dryas impact hypothesis: A requiem. *Earth Sci Rev* **106**, 247–264 (2011).
59. Surovell, T. A. *et al.* An independent evaluation of the Younger Dryas extraterrestrial impact hypothesis. *Proc Nat Acad Sci* **106**, 18155–18158 (2009).
60. Pigati, J. S. *et al.* Accumulation of impact markers in desert wetlands and implications for the Younger Dryas impact hypothesis. *Proc Nat Acad Sci* **109**, 7208–7212 (2012).
61. Andronikov, A. V. & Andronikova, I. E. Sediments from Around the Lower Younger Dryas Boundary (USA): Implications from LA-ICP-Analysis. *Geogr Ann A* **98**, 221–236 (2016).
62. Andronikov, A. V. *et al.* Geochemical evidence of the presence of volcanic and meteoritic materials in Late Pleistocene lake sediments of Lithuania. *J Quat Int* **386**, 18–29 (2015).
63. Andronikov, A. *et al.* In search for fingerprints of an extraterrestrial event: Trace element characteristics of sediments from the lake Medvedevskoye (Karelian Isthmus, Russia). *Doklady Earth Sciences* **457**, 819–823 (2014).
64. Mahaney, W. C. Cosmic airburst on developing Allerød substrates (soils) in the Western Alps, Mt. Viso area. *Stud Quat* **35**, 1–21 (2018).
65. LeCompte, M. A. *et al.* In *The Bowser Road Mastodon and the Younger Dryas Impact Hypothesis, Appendix 3 in The archaeological Recovery of the* Bowser Road Mastodon, Orange County *NY* (ed. Gramly, R. M.) (Persimmon Press, 2017).
66. Moreno, P. I. *et al.* Radiocarbon chronology of the last glacial maximum and its termination in northwestern Patagonia. *Quat Sci Rev* **122**, 233–249 (2015).
67. Fuhrer, K. & Legrand, M. Continental biogenic species in the Greenland Ice Core Project ice core: Tracing back the biomass history of the North American continent. *J Geophys Res* **102**, 26735–26745 (1997).
68. Legrand, M., De Angelis, M., Staffelbach, T., Neftel, A. & Stauffer, B. Large perturbations of ammonium and organic acids content in the Summit-Greenland ice core. Fingerprint from forest fires? *Geophys Res Lett* **19**, 473–475 (1992).
69. Mayewski, P. A. *et al.* Major features and forcing of high-latitude northern hemisphere atmospheric circulation using a 110,000-year-long glaciochemical series. *J Geophys Res* **102**, 26345–26366 (1997).
70. Mayewski, P. A. *et al.* The atmosphere during the Younger Dryas. *Science* **261**, 195–197 (1993).
71. Fischer, H. *et al.* Millennial changes in North American wildfire and soil activity over the last glacial cycle. *Nat Geosci* **8**, 723 (2015).
72. Anders, E., Wolbach, W. S. & Gilmour, L. Major wildfires at the Cretaceous/Tertiary boundary. **247**, 391–400 (1990).

73. Wolbach, W. S., Lewis, R. S. & Anders, E. J. S. Cretaceous extinctions: evidence for wildfires and search for meteoritic material. **230**, 167–170 (1985).
74. Belcher, C. M., Collinson, M. E., Sweet, A. R., Hildebrand, A. R. & Scott, A. C. Fireball passes and nothing burns—The role of thermal radiation in the Cretaceous-Tertiary event: Evidence from the charcoal record of North America. *J Geol* **31**, 1061–1064 (2003).
75. Ferguson, D. K. The origin of leaf-assemblages—new light on an old problem. *Rev Palaeobot Palynol* **46**, 117–188 (1985).
76. Spicer, R. A. The formation and interpretation of plant fossil assemblages. *Adv Bot Res* **16**, 95–191 (1989).
77. Villagrán, C. Análisis palinológico de los cambios vegetacionales durante el Tardiglacial y Postglacial en Chiloé, Chile. *Rev Chil Hist Nat* **58**, 57–69 (1985).
78. Villagrán, C. Un modelo de la historia de la vegetación de la Cordillera de La Costa de Chile central-sur: la hipótesis glacial de Darwin. *Rev Chil Hist Nat* **74**, 793–803 (2001).
79. Moreno, P. I., Lowell, T. V., Jacobson, G. L. Jr. & Denton, G. H. Abrupt vegetation and climate changes during the last glacial maximumand last termination in the chilean lake district: a case study from canal de la puntilla (41°s). *J Quat Sci* **81**, 285–311 (1999).
80. Moreno, P. I., Abarzúa, A. M. & Villagrán, C. Deglacial and postglacial climate history in east-central Isla Grande de Chiloé, southern Chile (43°S). *Quat Res* **62**, 49–59 (2004).
81. Pesce, O. & Moreno, P. Vegetation, fire and climate change in central-east Isla Grande de Chiloé (43 S) since the Last Glacial Maximum, northwestern Patagonia. *Quat Sci Rev* **90**, 143–157 (2014).
82. Jara, I. A. & Moreno, P. I. Climatic and disturbance influences on the temperate rainforests of northwestern Patagonia (40° S) since <14,500 cal yr BP. *Quat Sci Rev* **90**, 217–228 (2014).
83. Moreno, P. I., Jacobson, G. L., Lowell, T. V. & Denton, G. H. Interhemispheric climate links revealed by late-glacial cooling episode in southern Chile. *Nature* **409**, 804–808 (2001).
84. Moreno, P. I. & Videla, J. Centennial and millennial-scale hydroclimate changes in northwestern Patagonia since 16,000 yr BP. *Quat Sci Rev* **149**, 326–337 (2016).
85. Blunier, T. & Brook, E. J. Timing of millennial-scale climate change in Antarctica and Greenland during the last glacial period. *Science* **291**, 109–112 (2001).
86. Jouzel, J. *et al*. Orbital and millennial Antarctic climate variability over the past 800,000 years. *Science* **317**, 793–796 (2007).
87. Loulergue, L. *et al*. Orbital and millennial-scale features of atmospheric CH4 over the past 800,000 years. *Nature* **453**, 383–386 (2008).
88. Buiron, D., Chappellaz, J., Stenni, B., Frezzotti, M. & Baumgartner, M. TALDICE-1 age scale of the Talos Dome deep ice core, East Antarctica. *Clim Past* **7**, 1–16 (2011).
89. Stenni, B. Expression of the bipolar see-saw in Antarctic climate records during the last deglaciation. *Nat Geosci* **4** (2011).
90. Petit, J.-R. *et al*. Climate and atmospheric history of the past 420,000 years from the Vostok ice core, Antarctica. *Nature* **399**, 429–436 (1999).
91. Members, E. C. (ed EPICA Community Members) (PANGAEA, 2010).
92. Members, E. C. One-to-one coupling of glacial climate variability in Greenland and Antarctica. *Nature* **444**, 195–198 (2006).
93. Grootes, P., Steig, E. & Stuiver, M. The oxygen isotope record from Taylor Dome, Antarctica. *EOS Trans* **76**, S176 (1994).
94. Stocker, T. F. Past and future reorganizations in the climate system. *Quat Sci Rev* **19**, 301–319 (2000).
95. Broecker, W. S. Paleocean circulation during the Last Deglaciation: A bipolar seesaw? *Paleoceanography* **13**, 119–121 (1998).
96. Blunier, T. *et al*. Asynchrony of Antarctic and Greenland climate change during the last glacial period. *Nature* **394**, 739–743 (1998).
97. Denton, G. H. *et al*. The last glacial termination. *Science* **328**, 1652–1656 (2010).
98. Kennett, J. P. & Shackleton, N. J. Laurentide ice sheet meltwater recorded in gulf of Mexico deep-sea cores. *Science* **188**, 147–150 (1975).
99. Teller, J. T., Leverington, D. W. & Mann, J. D. Freshwater outbursts to the oceans from glacial Lake Agassiz and their role in climate change during the last deglaciation. *Quat Sci Rev* **21**, 879–887 (2002).
100. Murton, J. B., Bateman, M. D., Dallimore, S. R., Teller, J. T. & Yang, Z. Identification of Younger Dryas outburst flood path from Lake Agassiz to the Arctic Ocean. *Nature* **464**, 740–743 (2010).
101. Keigwin, L. *et al*. Deglacial floods in the Beaufort Sea preceded Younger Dryas cooling. *Nat Geosci*, 1 (2018).
102. Haug, G. H., Hughen, K. A., Sigman, D. M., Peterson, L. C. & Röhl, U. Southward migration of the intertropical convergence zone through the Holocene. *Science* **293**, 1304–1308 (2001).
103. Mariani, M. Coupling of the Intertropical Convergence Zone and Southern Hemisphere mid-latitude climate during the early to mid-Holocene. *Geology* **45**, 1083–1086 (2017).
104. Bereiter, B., Shackleton, S., Baggenstos, D., Kawamura, K. & Severinghaus, J. Mean global ocean temperatures during the last glacial transition. *Nature* **553**, 39–44 (2018).
105. Purkey, S. G. & Johnson, G. C. Antarctic Bottom Water warming and freshening: Contributions to sea level rise, ocean freshwater budgets, and global heat gain. *J Clim* **26**, 6105–6122 (2013).
106. Anderson, D. G., Goodyear, A. C., Kennett, J. & West, A. Multiple lines of evidence for possible Human population decline/ settlement reorganization during the early Younger Dryas. *Quat Int* **242**, 570–583 (2011).
107. Ahmed, S. I. & Cain, R. Revision of the genera Sporormia and Sporormiella. *Can J Bot* **50**, 419–477 (1972).
108. Gill, J. L. *et al*. Linking abundances of the dung fungus Sporormiella to the density of bison: implications for assessing grazing by megaherbivores in palaeorecords. *J Ecol* **101**, 1125–1136 (2013).
109. Davis, O. K., Agenbroad, L., Martin, P. S. & Mead, J. I. In *The Pleistocene dung blanket of bechan Cave, Utah in Contributions in Quaternary vertebrate paleontology: a volume in memorial to John E. Guilday*. Vol. 8 *Special Publications of* Carnegie Museum. (ed. Dawson, M. R.) 267–282 (Carnegie Museum of Natural History 1984).
110. Davis, O. K. & Shafer, D. S. Sporormiella fungal spores, a palynological means of detecting herbivore density. *Palaeogeogr Palaeoclimatol Palaeoecol* **237**, 40–50 (2006).
111. Etienne, D., Wilhelm, B., Sabatier, P., Reyss, J.-L. & Arnaud, F. Influence of sample location and livestock numbers on Sporormiella concentrations and accumulation rates in surface sediments of Lake Allos, French Alps. *J Paleolimnol* **49**, 117–127 (2013).
112. Koch, P. L. & Barnosky, A. D. Late Quaternary extinctions: state of the debate. *Annu Rev Ecol Evol Syst* **37** (2006).
113. Johnson, C. N., Haberle, S. G., Turney, C. S. M., Kershaw, A. P. & Brook, B. W. Using dung fungi to interpret decline and extinction ofmegaherbivores: problems and solutions. *Quat Sci Rev* **110**, 107–113 (2015).
114. Raczka, M. F., Bush, M. B., Folcik, A. M. & McMichael, C. H. Sporormiella as a tool for detecting the presence of large herbivores in the Neotropics. *Biota Neotropica* **16** (2016).
115. Baker, A. G., Cornelissen, P., Bhagwat, S. A., Vera, F. W. M. & Willis, K. J. Quantification of population sizes of large herbivores and their long-term functional role in ecosystems using dung fungal spores. *Methods Ecol Evol* **7**, 1273–1281 (2016).
116. Brook, B. W. & Barnosky, A. D. In *Quaternary extinctions and their link to climate change in Saving a Million Species* 179–198 (Springer, 2012).
117. Barnosky, A. D., Koch, P. L., Feranec, R. S., Wing, S. L. & Shabel, A. B. Assessing the causes of late Pleistocene extinctions on the continents. *Science* **306**, 70–75 (2004).
118. Barnosky, A. D. & Lindsey, E. L. Timing of Quaternary megafaunal extinction in South America in relation to human arrival and climate change. *Quat Int* **217**, 10–29 (2010).

119. Villavicencio, N. A. Combination of humans, climate, and vegetation change triggered Late Quaternary megafauna extinction in the Última Esperanza region, southern Patagonia, Chile. *Ecography* **39**, 125–140 (2016).
120. Metcalf, J. L. *et al*. Synergistic roles of climate warming and human occupation in Patagonian megafaunal extinctions during the Last Deglaciation. *Sci Adv* **2**, e1501682 (2016).
121. Recabarren, O. P., Pino, M. & Cid, I. A new record of Equus (Mammalia: Equidae) from the Late Pleistocene of central-south Chile. *Rev Chil Hist Nat* **84**, 535–542 (2011).
122. Surovell, T. A., Pelton, S. R., Anderson-Sprecher, R. & Myers, A. D. Test of Martin's overkill hypothesis using radiocarbon dates on extinct megafauna. *Proc Nat Acad Sci* **113**, 886–891 (2016).
123. Clube, S. & Napier, W. The microstructure of terrestrial catastrophism. *Mon Not R Astron Soc* **211**, 953–968 (1984).
124. Steel, D. & Asher, D. The orbital dispersion of the macroscopic Taurid objects. *Mon Not R Astron Soc* **280**, 806–822 (1996).
125. Florenskiy, K. Preliminary results from the 1961 combined Tunguska meteorite expedition *Meteoritica*, 3–37 (1965).
126. Hoyle, F. & Wickramasinghe, C. Comets, ice ages, and ecological catastrophes. *Ap&SS* **53**, 523–526 (1978).
127. Ramsey, C. B. Bayesian Analysis of Radiocarbon Dates. *Radiocarbon* **51**, 337–360 (2009).
128. Zuur, A., Ieno, E., Walker, N., Saveliev, A. & Smith, G. *Mixed effects models and extensions in ecology with R*. (Springer-Verlag, 2009).
129. R: A language and environment for statistical computing. (R Foundation for Statistical Computing, Vienna, Austria, 2017).
130. Faegri, K., Iversen, J., Kaland, P. & Krzywinski, K. *Textbook of pollen analysis*. (Wiley, 1989).
131. Heusser, C. J. *Pollen and spores of Chile: modern types of the Pteridophyta*, *Gymnospermae*, *Angiospermae*. (University of Arizona Press, 1971).
132. Tilia and TGView 2 (Illinois State Museum, Springfield, IL, 2004).
133. Grimm, E. C. & Geosciences. CONISS: a FORTRAN 77 program for stratigraphically constrained cluster analysis by the method of incremental sum of squares. *Comput Geosci* **13**, 13–35 (1987).
134. Whitlock, C. & Larsen, C. In *Charcoal as a fire proxy in Tracking environmental change using lake sediments* Vol. 3 75–97 (Springer, 2002).
135. Aptroot, A. & van Geel, B. Fungi of the colon of the Yukagir Mammoth and from stratigraphically related permafrost samples. *Rev Palaeobot Palynol* **141**, 225–230 (2006).
136. Graf, M. & Chmura, G. L. Development of modern analogues for natural, mowed and grazed grasslands using pollen assemblages and coprophilous fungi. *Rev Palaeobot Palynol* **141**, 139–149 (2006).
137. van Geel, B. *et al*. Palaeo-environmental and dietary analysis of intestinal contents of a mammoth calf (Yamal Peninsula, northwest Siberia). *Quat Sci Rev* **30**, 3935–3946 (2011).
138. Wood, J. R., Wilmshurst, J. M., Worthy, T. H. & Cooper, A. Sporormiella as a proxy for non-mammalian herbivores in island ecosystems. *Quat Sci Rev* **30**, 915–920 (2011).
139. Araujo, B. B., Oliveira-Santos, L. G. R., Lima-Ribeiro, M. S., Diniz-Filho, J. A. F. & Fernandez, F. A. Bigger kill than chill: The uneven roles of humans and climate on late Quaternary megafaunal extinctions. *Quat Int* **431**, 216–222 (2017).
140. Prado, J. L., Martinez-Maza, C. & Alberdi, M. T. Megafauna extinction in South America: a new chronology for the Argentine Pampas. *Palaeogeogr Palaeoclimatol Palaeoecol* **425**, 41–49 (2015).

Acknowledgements

We also acknowledge very useful suggestions from Jon Hagstrum, U.S. Geological Survey, and the valuable assistance of Javiera Barria, Daniel Fritte, Jennifer Zeldin, and David Kimbel. We are very grateful for a grant from James Marvin and 110 Indiegogo crowdfunding donors, who generously helped make this research possible. Also, we gratefully acknowledge funding through an Academic Senate Faculty Research Grant to James Kennett at the University of California Santa Barbara, from Fondo Nacional de Desarrollo Científico y Tecnológico (FONDECYT), Chile through grant # 11140677 to Ana M. Abarzúa, #3170958 to Giselle Astorga and grants #1100555 and #1150738 to Mario Pino Quivira and TAQUACH/Vicerrectoría de Desarrollo, Investigación y Creación Artística (VIDCA), Universidad Austral de Chile.

Author Contributions

M.P., A.M.A. and A.W. conceived the project. M.P., A.M.A., A.W. and J.P.K. wrote most of the manuscript. M.P. and A.M.A. directed most of the fieldwork. M.P., A.M.A., G.A., A.M-C., N.C-M., R.X.N., M.P.L., R.L., M.A.L., V.A., C.R.M., T.E.B., C.M., W.S.W., A.W. and J.P.K. contributed field data, laboratory analyses, data interpretations, and/or relevant sections to the supplemental. All authors reviewed and approved the manuscript.

Additional Information

Supplementary information accompanies this paper at https://doi.org/10.1038/s41598-018-38089-y.

Competing Interests: The authors declare no competing interests.

Publisher's note: Springer Nature remains neutral with regard to jurisdictional claims in published maps and institutional affiliations.

Sedimentary record from Patagonia, southern Chile supports cosmic-impact triggering of biomass burning, climate change, and megafaunal extinctions at 12.8 ka

Mario Pino, Ana M. Abarzúa, Giselle Astorga, Alejandra Martel-Cea, Nathalie Cossio-Montecinos, R. Ximena Navarro, Maria Paz Lira, Rafael Labarca, Malcolm A. LeCompte, Victor Adedeji, Christopher R. Moore, Ted E. Bunch, Charles Mooney, Wendy S. Wolbach, Allen West, James P. Kennett

SUPPLEMENTARY INFORMATION:

Text S1. Previously reported evidence of YDB magnetic spherules.

This study of the Pilauco sedimentary sequence identifies 6 groups of spherulitic particles:

Group 1: Melted YDB impact spherules with dendritic textures and/or vesicles;
Group 2: Melted Cr-rich YDB spherules;
Group 3: Melted glassy volcanic spherules with low-Fe content;
Group 4: Unmelted, authigenic framboids with numerous cube-like crystals, often with high sulfur content;
Group 5: Melted anthropogenic spherules in surface sediments;
Group 6: Unmelted, rounded, detrital grains often with high titanium content and visible facets.

For distinguishing characteristics of each type, see **Table S10**. These spherulitic objects cannot be distinguished from one another using a reflected-light microscope. Instead, they require the use of SEM-EDS and/or a microprobe, as specified by Firestone et al.[1], who wrote on page 17-18 of their Supporting Information: "*spherules were either left whole or sectioned and given a microprobe polish for analysis by laser ablation or x-ray fluorescence (SEM/XRF).*"

Firestone et al.[1] identified YDB peaks in impact-related spherules at 14 sites. Of 13 subsequent independent studies, 8 performed SEM-EDS and/or microprobe analyses and found a significant peak in the YDB, as predicted. The other 5 studies reported that "YDB spherules" are heterogeneously common throughout the sediment, and, therefore, cannot be impact-related. However, those studies either did not perform SEM-EDS analyses or performed them incorrectly, and therefore could not differentiate between anthropogenic, authigenic, volcanic, and impact-related spherules. Instead, they assumed that all spherulitic particles they found were high-temperature, melted "YDB spherules."

Independent studies of YDB magnetic spherules:

Performed SEM-EDS. Baker et al.[2] reported finding a YD-age site in Montana, writing that "*the black mat contains … unrusted iron micro-meteorites [native iron magnetic spherules]. SEM photos of iron micro-meteorites reveal fusion crusts, flow lines, and micro-impact craters--direct evidence for an extraterrestrial origin*."

Performed SEM-EDS, microprobe. At Murray Springs, Arizona, Fayek et al.[3] found that "*impact material contains iron oxide spherules (framboids) in a glassy iron-silica matrix, which is one indicator of a possible meteorite impact. ... Such a high formation temperature is only consistent with impact ... conditions.*" Because the framboids were encased in meltglass, they are inferred to have resulted from a cosmic impact.

Performed SEM-EDS. Ge et al.[4] reported YD-age "*microtektite-like glassy spherules*" from 3 widely separated sites, in France, in the Caspian Sea, and in the Peruvian coastal desert. They state that the evidence "*supports an impact origin from an ejecta plume*."

No SEM-EDS. Surovell et al.[5] were unable to reproduce the spherule data of Firestone et al.[1], and, instead, reported finding YDB spherules heterogeneously distributed throughout the sediment profiles at seven sites. They concluded that YDB spherules are common and not restricted to the YDB layer, and, therefore, cannot be impact-related. Their Methods section states that the group used an updated spherule protocol from Firestone et al.[1] sent by one of the co-authors (A.W.) of this contribution. However, Surovell et al. did not conduct any SEM-EDS analyses of the candidates, as specified in the Firestone et al.[1] protocol. Thus, it is unclear what this group found, but they likely misidentified some detrital grains and/or framboids as "YDB spherules."

Performed SEM-EDS. In 2010, Laub[6] investigated sediment samples from the Hiscock archaeological-paleontological site in western New York state. He reported that "*iron-rich spherules, 50-65 µm in diameter, were found in the Pleistocene horizon*" spanning the YD onset, as reported by Firestone et al.

Performed SEM-EDS. Mahaney et al.[7,8] found in Venezuela "*a mixed assemblage … of Fe spherules*" in a YD-age layer "*with a frequency higher than chance occurrence.*" Mahaney et al.[8] concluded that the "*new evidence … point tentatively to either an asteroid or comet event that reached far into South America*."

Microprobe; no SEM-EDS; flawed analyses. Haynes et al.[9] observed high concentrations of magnetic spherules in the YDB layer at Murray Springs, Arizona, consistent with the observations of Firestone et al.[1] and Fayek et al.[3] They also reported abundant spherules from modern alluvium and rooftops, concluding that their presence refutes the YDB hypothesis. They conducted SEM-EDS/microprobe analyses, but did not differentiate between YDB spherules, anthropogenic spherules, framboids, and detrital grains, and instead, assume that all were "YDB spherules.". Many of these types are nearly ubiquitous in surface sediments.

SEM-EDS; flawed analyses. Pinter et al.[10] reported on two sites in California at which "*magnetic spherules are heterogeneously distributed in sediments*", and concluded that this refuted the YDB impact hypothesis. Although this group acquired SEM images to support their argument, they presented only images of unmelted framboids and unmelted detrital grains and showed no SEM images

of melted, dendritic YDB spherules, thus calling into question their conclusions that they observed abundant "YDB spherules" at all.

Performed SEM-EDS, microprobe. Wu et al.[11] reported YDB spherules from two sites in North America and found evidence of high-temperature melting under low-oxygen conditions, as at Pilauco. They concluded that "*the [Fe-rich] spherules could be generated in a meteorite impact.*"

No SEM-EDS. Pigati et al.[12] confirmed a YDB peak in spherules at Murray Springs, Arizona, as previously reported by Firestone et al.[1] and Fayek et al.[3] They also reported multiple non-YDB spherule peaks at Chilean sites and claimed that this refuted the YDB impact hypothesis. The Chilean sites, however, are known to contain abundant volcanic spherules[13]. Because Pigati et al. did not conduct any SEM-EDS analyses, they assumed that the abundant spherules they found near volcanoes were "YDB spherules", thus calling their conclusions into question.

Performed SEM-EDS. LeCompte et al.[14] compared the results of Firestone et al.[1] and Surovell et al.[5] at two sites: Blackwater Draw, NM and Topper, SC. They reported that their "*spherule abundances are consistent with those of Firestone et al.[1] and inconsistent with the results of Surovell et al.*" They concluded that Surovell et al. were unable to reproduce the results of Firestone et al. "*primarily due to their failure to adhere to the [Firestone] protocol*", mainly by omitting SEM-EDS analyses.

Mixed SEM-EDS. In a blind test, Holliday et al.[15] reported that both participants found "YDB spherules" in non-YDB sections of a sedimentary profile in Texas, but one participant performed no SEM-EDS analyses to confirm that claim. The other participant used SEM EDS to identify found an unpublished peak in spherules in the YDB layer.

Performed SEM-EDS. Andronikov et al.[16] reported peak abundances of spherules in the YDB layer at a site at Blackwater Draw, New Mexico. SEM-EDS analyses showed that some spherules were highly enriched in iridium and platinum. Andronikov et al.[16] stated that "*Our observations confirm those made by Firestone et al.[1] and LeCompte et al.[14]*," but they contradicted the previously reported lack of a spherule peak by Surovell et al.[5]

In summary, the majority of independent studies (8 of 13) that conducted SEM-EDS analyses confirmed the presence of YDB spherules in layers that date to ~12,800 cal BP. The other five studies did not conduct SEM-EDS correctly and could not confirm the presence of YDB spherules.

Text S2. Background: Paleoclimate and Biota.

Pilauco is located in southern Chile between ~38° to 56° S and the region is largely influenced by westerly winds of the Southern Hemisphere. Presently, the region spans three major vegetation zones: (1) from 37º 45' S to 43º 20' S, including Pilauco, where the vegetation corresponds to the Valdivian rainforest that is replaced farther south by; (2) the North Patagonian forest (to 47º 30' S), and then, in turn, by (3) the sub-Antarctic Flora in association with the Magellanic Moorland (to 55º30' S)[17-19]. This meridional zonation in vegetation is largely due to a strong precipitation gradient with annual values ranging from 1500 mm at 38º S to 4500 mm at 47° S. In contrast, the annual atmospheric temperature range over these same latitudes is only 2 °C[20].

During the late Quaternary, the meridional range of these three vegetation provinces was likely affected by multi-millennial changes in the latitudinal position and/or the intensity of the westerly winds, causing significant variations in precipitation and dryness. Additionally, it has been postulated that during the Last Glacial Maximum (LGM; from ~23,000 to 17,500 cal BP[21,22]) the westerly winds may have intensified and expanded towards the equator thus bringing lower temperatures and higher precipitation rates to the Pilauco area[22-25]. Also, there is evidence of altitudinal descent and/or meridional advances in vegetation that occurred after the LGM[23]. This evidence includes presence of the Magellanic Moorland circa Llanquihue (41°S) and Chiloé (42°S) between 17,500 to 16,000 cal BP[22,26-28], and presence of the evergreen tree, *Araucaria araucana* in lowland areas of the Araucanía Region (38º S) between 26,000 and 16,000 cal BP[29].

Several pollen records from northern Patagonia exhibit a vegetation shift, which began at ~17,500 cal BP. This shift was from cool rainforests dominated by cold-resistant *Nothofagus dombeyi*-type and grasslands (Poaceae and Ericaceae) to a warmer thermophilous vegetation. Also, expansions of the Myrtaceae family and the arboreal vine *Hydrangea serratifolia*, at ~16,000 and 14,000 cal BP respectively, reflect this warming trend[30-32]. In the Chiloé area to the south, most early deglacial pollen records are dominated by Magellanic Moorland species that typically reflect cold, wet conditions. Pollen records from Lago Lepué in Chiloé[32] and from the Chilean Lake District[31,33-35] also exhibit increased Podocarpaceae taxa (southern conifers) indicating cooling with increased precipitation until ~13,000 cal BP. Between ~13,000 to 11,600 cal BP most regional pollen records indicate an increased magnitude and seasonality in precipitation. This interval is also marked by increased charcoal concentrations reflecting a significant increase in biomass burning[32,36].

In northwestern Patagonia (38º to 42º S) during the last glacial termination, glaciers occupied both sides of the Andes Cordillera and part of the Intermediate Depression, replacing extensive areas of vegetation[37]. At ~17,500 cal yr BP, the glaciers experienced a rapid recession in lowland areas, and within a thousand years, temperatures increased reaching near-modern values, which promoted the recolonization by vegetation of areas disrupted by glacial activity[30,38]. Beginning at ~14,400 cal BP, multiple regional climate records in lake sediments (~40° S) show that the warm climate became colder during the Antarctic Cold Reversal[39-42], locally known as the Huelmo-Mascardi Cold Reversal[31,43-45].

Text S3. Sedimentology

The earliest sedimentological interpretation of the Pilauco section was that its sandy sediments and gravel were associated with fluvial plain deposits within a former oxbow lake[46]. It was inferred that the gravel was transported as rolling bed load to the south of the old Damas River's main channel and into a swamp. Later, Pino et al.[46] noted that surfaces of the aphanitic basalt boulders and pebbles had no impact marks, contradicting the previous interpretation that there had been high-velocity transport. In the grids excavated after 2013, new stratigraphic observations indicate that in units PB-7 through PB-9 there are no sedimentary structures suggesting fluvial deposition (e.g., imbrication and cross-bedded laminations). Pino et al.[47] performed sand grain-size analysis (mean grain size, sorting, skewness, and

kurtosis) and discriminant analyses on 27 samples from units PB-7 and PB-1, the latter (San Pablo Unit) having been collected from the hill bordering the site to the north. These results indicate that the siliciclastic sediments of both units are indistinguishable. This means that the sediments, dominated by very coarse and coarse sand, were not high-energy river deposits, but instead resulted from colluvial processes (gravitational and/or water transport from the northern hills). The laminar dip in unit PB-9 indicates that the sediment was transported downslope from the north. The textures suggest that, at times, stratigraphic deposition of this unit was primarily driven by gravity (boulders of volcanic tuff in a fine matrix, see **Figure S4**), and at other times by water transport/deposition (probably intense rain) that formed ponds in which laminated sediments accumulated (see **Figure S4**).

River deposits typically exhibit a close relationship between concentrations of gravel and very coarse sand. Linear regression analysis on these parameters revealed no statistically significant relationship between the gravel and very coarse sand fractions. This indicates that the abundance of gravel is not related to colluviation from the nearby San Pablo Unit, and also reinforces the idea that river processes did not deposit unit PB-7.

Colluviation explains the coexistence of a sand matrix, carbon organic matter, and gravel clasts "floating" in a mixture of sand and mud. After deposition of the YDB layer in unit PB-8, the swamp was probably seasonally dry, especially during summers, as indicated by the presence of carabids and dung beetles[48]. In unit PB-9, large amounts of volcanoclastic cobbles and pebbles were deposited during intense erosional processes on the northern hills following forest fires.

The basal unit studied in the Pilauco stratigraphic sequence is PB-6, an unconsolidated sediment containing well-rounded pebbles to boulders of plutonic and volcanic Andean rocks, ranging from 1 to 15 cm in diameter. Unit PB-6 contains ~10% organic matter with ~60% sand (sieved from 2000 to 62.5 μm) and ~30% mud (<62.5 μm) (**Table S2, S3**).

The next higher unit, PB-7, is an organic-rich sand composed of isolated, poorly sorted colluvial volcanoclastics, ranging in size up to 7 cm (percentage not quantified) with the remainder composed of 70.7% sandy matrix (2000 to 62.5 μm), 16.3% mud (<62.5 μm), and 12.9% fine organic material, as determined by loss-on-ignition values. The sediment's color is brownish-black (Munsell scale: 10YR 3/1) (**Table S2, S3**). Unit PB-7 is separated from unit PB-6 by an abrupt and variably inclined boundary, and contains most of the extinct megafauna remains (e.g., fossil remains of the Gomphotheriidae), bones of extant micromammals, numerous vegetal and invertebrate remains, and lithic artifacts.

Unit PB-8 is composed of organic-rich mudstones separated by thin, muddy laminae, similar to unit PB-7. The unit is slightly brown in color (2.5Y 4/2) (**Table S2, S3**). Both units were deposited in a seasonal swamp with colluvial contributions of volcanoclastic sand and gravel. The upper boundary of unit PB-8 dips about 15º to the south near the northern hill (grids 6AD to 7AD) and is nearly horizontal between grids 7AD and 10AD. This unit contains fewer mammal fossils and lithic artifacts than unit PB-7 below it, and although fossil remains of Gomphotheriidae are not recorded in this unit, it contains the youngest horse coprolite found at the site[46,47].

At Pilauco, the key stratigraphic feature is the PB-8/PB-9 boundary, marking major changes in the environment and in sedimentation. Immediately above that boundary there is a large accumulation of wood fragments, frequently found along a sharply defined, undulating contact (**Figure S2, S3, S4**). This boundary marks the sudden onset of higher sedimentation rates and increased transport of sediment as indicated by the presence of large blocks from the northern hills associated with fine sediment laminae, thin lenses, and lag deposits of material sorted by aeolian, fluvial, and other natural processes (**Figure S4**).

Unit PB-9 is largely a relatively fine-grained, black, organic-rich peat (mean matrix color 2.5Y 2/0) (**Figure 2**) that is lithologically and environmentally much more variable than units PB-7 and PB-8. This unit contains numerous southward-dipping lenses with varying concentrations of organic and inorganic material. The peat includes abundant yellow volcanic tufa fragments derived from volcanoclastic layers in the northern hills, as well as decimetric wood and charcoal fragments. Unit PB-9 is composed of a mixture of 74.4% sandy matrix, 16.2% fine mud, and 9.4% fine-grained organic material. The percentage of the fine sediment fraction (<106 μm) doubled above the PB-8/PB-9 boundary from ~30% to ~60% before gradually increasing to ~70% (**Figure S5; Table S2, S3**).

The principal constituent of units PB-6 through PB-9 is sand (>60%) that acts as a matrix (**Table S2, S3**). Textural analysis of sediment samples from the top of unit PB-6 to the top of PB-9 (grid 14AD, 255 samples, 326 to 581 cm altitude) indicates that gravel (mostly volcanoclastic) constitutes between 12 to 22% of the total inorganic sedimentary fraction. Because the samples were only 5 cm wide, the concentrations of gravel are random rather than representative, and so they were not considered in the textural description. The units were subdivided into subunits A through F (**Figure 2**), where A, B and C have sand concentrations of 63%, 58%, and 60%, respectively, and mud concentrations of 37%, 42%, and 40%, respectively (gravel not quantified). These subunits differ mostly in their concentrations of microscopic charcoal. The most conspicuous subunit (D) is siliciclastic, containing the highest concentration of tuff fragments deposited by colluvial processes from the northern hills. The subunit's composition is 15% blocks, 66% gravel, 11% sand, and 8% mud. Lenses E and F are dominated by fine local volcanoclastic material at 88% and 95%, respectively, with the remainder as organic material. Granulometric analyses indicate lens E is composed of 10% sand and 90% mud; lens F is 4% sand and 96% mud (**Table S2, S3**). In these lenses, the dark red and grey colors (10R 3/6 and 5Y 5/1) result from varying degrees of oxidation/reduction of organic matter. A young organic soil caps the sequence.

The percentage of organic matter (~10%) in units PB-7 through PB-9 was calculated by loss-on-ignition. However, this value does not really represent its abundance because the low carbon concentrations of ~0.7 g cm^{-3} (relative to mineral concentrations of 2.6 g cm^{-3}) would be ~3 times greater if volume is considered. Organic matter is estimated to average ~30% by volume, which explains the plastic appearance of these units (**Table S2, S3**).

Text S4. Background on human lithics and artifacts.

At most South American sites older than 11,700 cal BP, the most commonly recorded cultural remains are non-formal lithic materials. Arguments about the earliest age of occupation generally have focused on whether the ages of the sites are correct and whether the cultural remains represent the development of local lithic technologies (cf. references in Bryan and Gruhn[49] and Gnecco and Aceituno[50]). Most of the discussion is centered on the comparison of area lithics with bifacial technology, dating from the Pleistocene-

Holocene boundary[51,52]. However, recent studies provide new evidence of Pleistocene sites dominated by unifacial lithics[53,54]. At Pleistocene settlements across South America, both unifacial and bifacial lithic materials were derived mainly from locally sourced materials[55]. This trend shows a strong shift at the beginning of the Holocene, as in North America, where different styles of points and other bifacial tools, produced from more diverse raw materials, became more frequent in the archaeological record[52]. We infer that the transition from Clovis to Folsom points near the YD onset in North America is similar to the transition that occurred at the same time in South America from the Edge-Trimmed Unifacial Tradition (with few examples of bifacial artifacts) to the well-developed Bifacial Tradition[54].

Text S5. Earlier South American impact events.

In South America, at least two large cosmic impact events are associated with major faunal extinctions, similar to those at ~12.8 ka. The first, the 66-Ma-old K-T impact in Yucatán, triggered the worldwide extinction of ~75% of all extant species[56] and caused abrupt, severe climate change.

During the middle Pliocene, around 3.3 million years ago, a major cosmic event deposited impact-related meltglass across a large part of eastern Argentina[57]. This impact event is associated with significant extinctions of terrestrial fauna in the Pampas region of Argentina, involving ~37% of all genera and ~53% of all species[58]. This event was also coeval with an abrupt change in the deep-sea isotopic record that reflects an abrupt disruption of climate and ocean circulation[57].

Thus, cosmic impacts are known to have previously triggered extinctions and abrupt climate change in South America, similar to those at the YD onset.

SUPPLEMENTARY INFORMATION: Figures

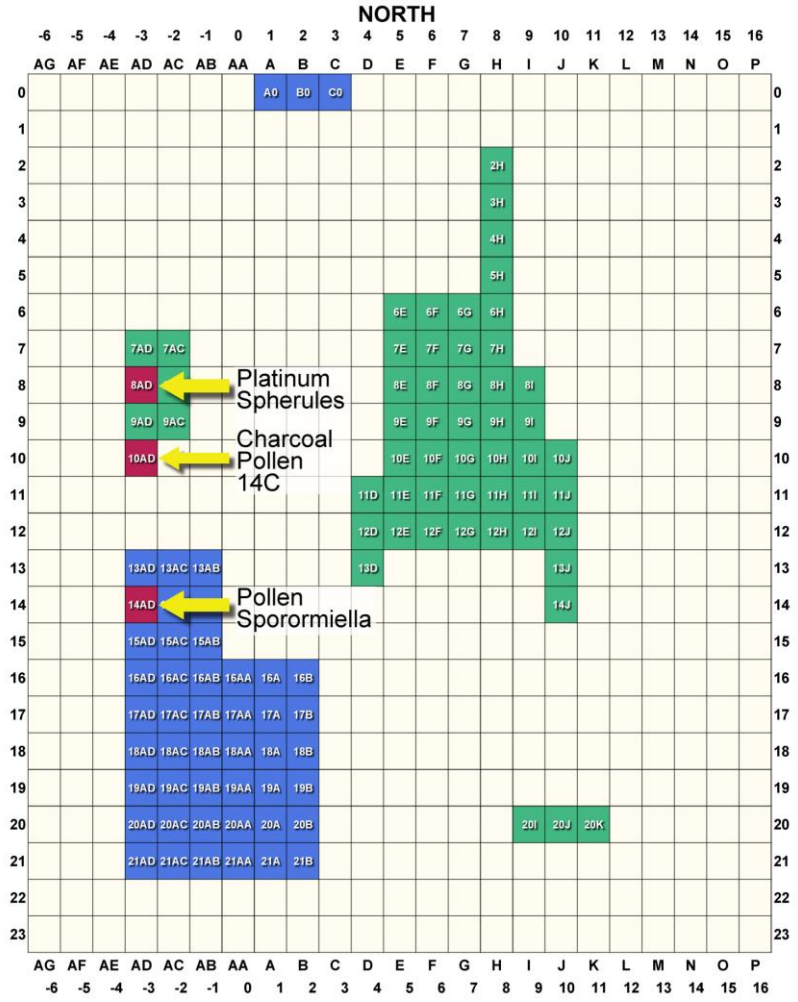

Figure S1. Excavation grids at Pilauco. Blocks in red represent those areas of the excavation that contributed data to this paper. Grid 8AD was investigated for platinum and magnetic spherules; Grid 10AC was sampled for charcoal, pollen, and radiocarbon dating (in this study and previously[46]); and Grid 14AD was investigated for pollen and *Sporormiella* spores.

Figure S2. Sampling location in grid 8AD. Green pins indicate sampling locations.

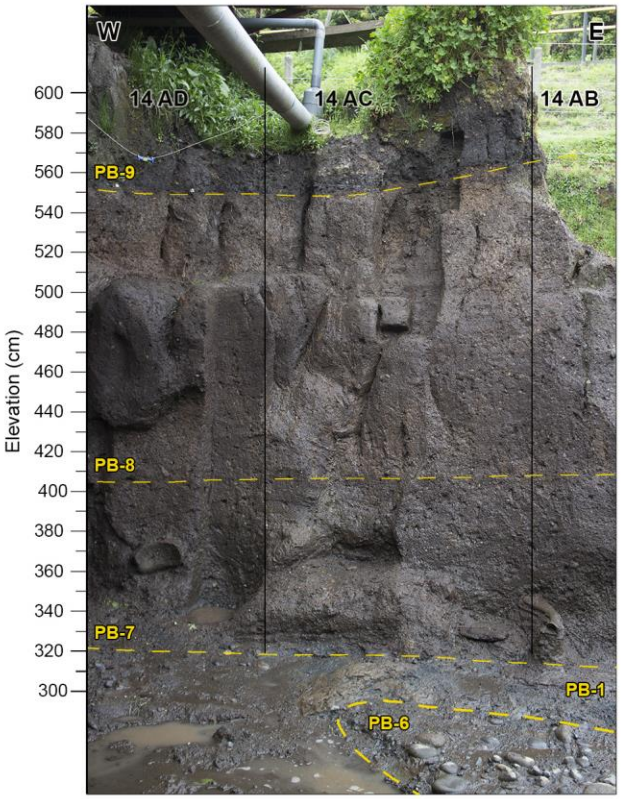

Figure S3. Image of sampling wall for grids 14AD through 14AB.

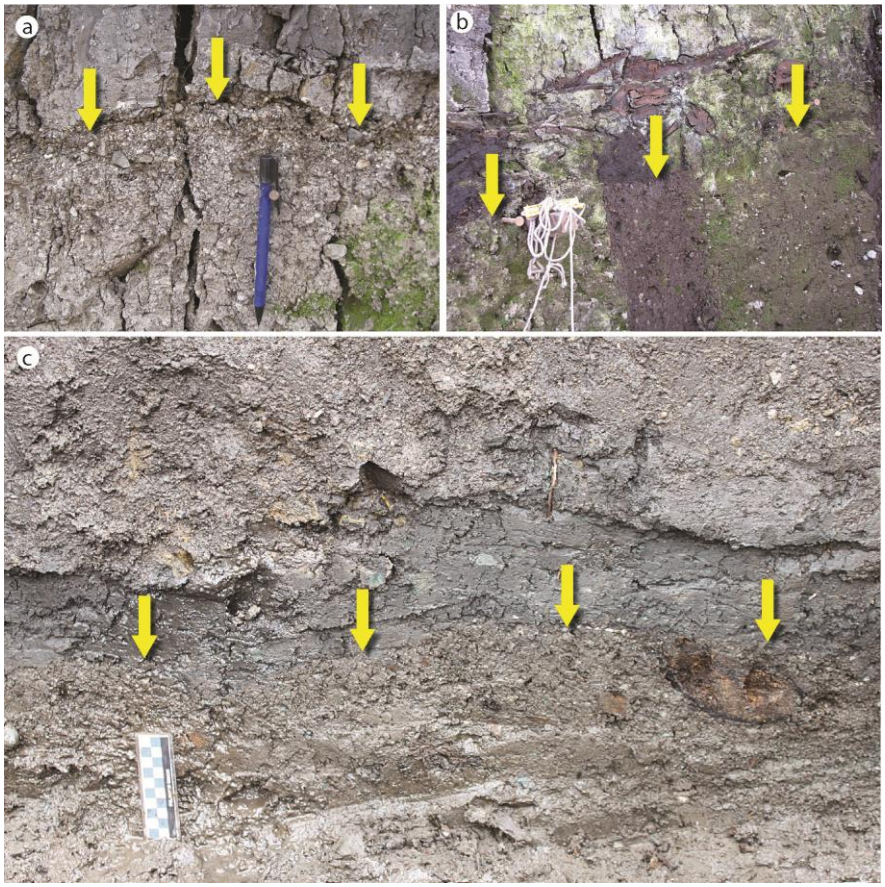

Figure S4. Sediment boundary types. Three types of PB-8/PB9 boundaries marked by yellow arrows. ***a)*** A gravel lag deposit; ***b)*** wood cluster; and ***c)*** sharp, undulating stratigraphic break.

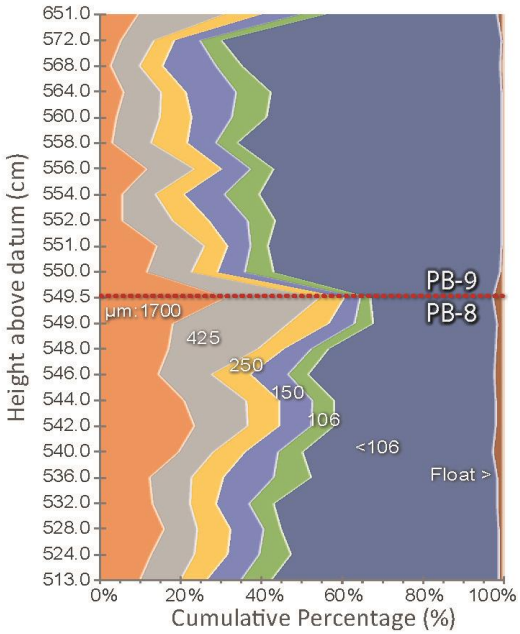

Figure S5. Sediment grain size analysis. The coarseness of sediment increases up to the YDB layer at the PB-8/PB-9 boundary. At that level, the size of the fine fraction <106 µm doubled to ~60% before gradually rising further to ~70%. This shift corresponds to climate change, an increase in biomass burning, and the resulting denuded landscape that, in turn, produced more fine-grained colluvium.

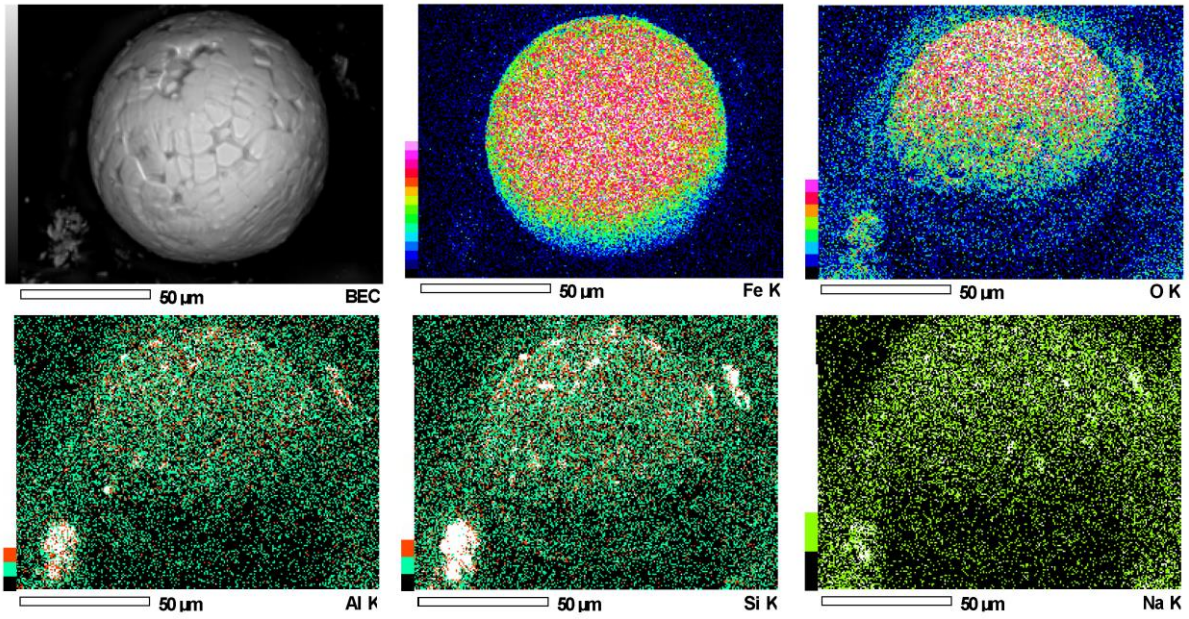

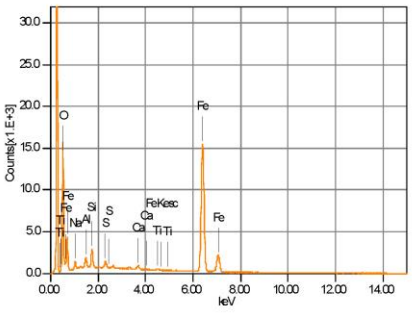

Acquisition Condition

Instrument	: 6510(LA)
Volt	: 20.00 kV
Current	: ---
Process Time	: T3
Live time	: 235.39 sec.
Real Time	: 245.76 sec.
DeadTime	: 3.00 %
Count Rate	: 2668.00 CPS

Formula	mass%	Atom%	Sigma	Net	K ratio	Line
O	25.54	52.11	0.09	38863	0.1488541	K
Na	2.07	2.94	0.10	2395	0.0048855	K
Al	1.06	1.28	0.06	2901	0.0035666	K
Si	2.48	2.88	0.07	8007	0.0110181	K
S	0.87	0.88	0.03	3314	0.0055026	K
Ca	0.56	0.46	0.04	2248	0.0048565	K
Ti	0.35	0.24	0.04	968	0.0027435	K
Fe	67.07	39.20	0.23	104525	0.5127303	K
Total	100.00	100.00				

Figure S6. **SEM-EDS elemental map of YDB spherule Y6.** SEM image of YDB spherule shown in Figure 5b of main manuscript. SEM-EDS chemistry (**Table S7)** shows that spherule is composed of nearly all FeO. It contains only minor amounts of other elements, most of which are probable surface contamination, such as the white areas in lower row of images above.

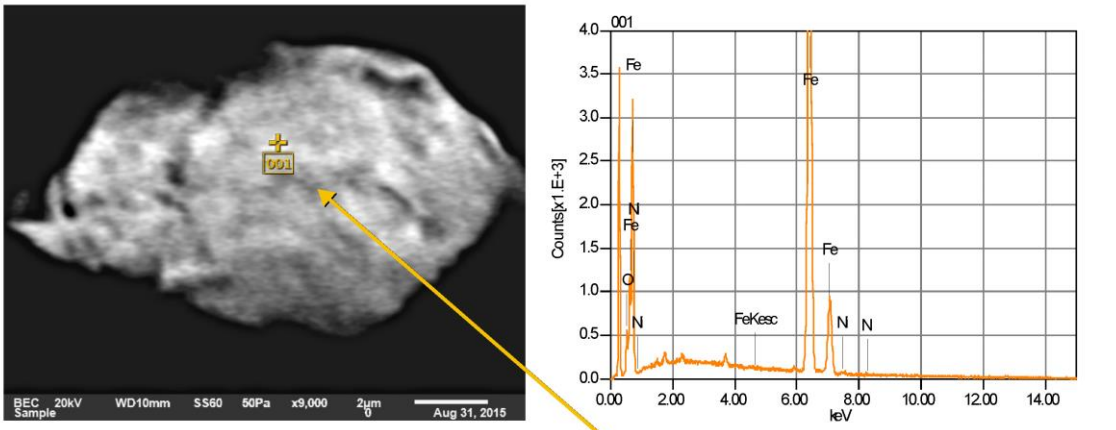

Volt	: 20.00 kV	Acquisition Condition		Formula	mass%	Atom%	Sigma	Net	K ratio	Line
Mag.	: x 9,000	Instrument	: 6510(LA)	O	2.09	6.93	0.02	9997	0.0278372	K
Date 2015/08/31	:	Volt	: 20.00 kV	Fe	97.21	92.43	0.15	479657	1.7105423	K
		Current	: ---	Ni*	0.70	0.64	0.05	2211	0.0110887	K
Pixel	: 640 x 480	Process Time	: T4	Total	100.00	100.00				
		Live time sec.	: 30.00							
		Real Time sec.	: 35.03							

Figure S7. SEM-EDS of 11-μm-long, irregularly-shaped, native iron grain with >97% Fe and ~2% oxygen. Morphology indicates high-temperature melting under reducing conditions. The grain contains a small amount of Ni, possibly of extraterrestrial origin; alternately, the Ni content could have resulted from melting of Ni-bearing magnetite. Either way, this grain is not a product of natural terrestrial processes, but could have been melted at high-temperature during a cosmic impact event. From the 552-cm YDB layer.

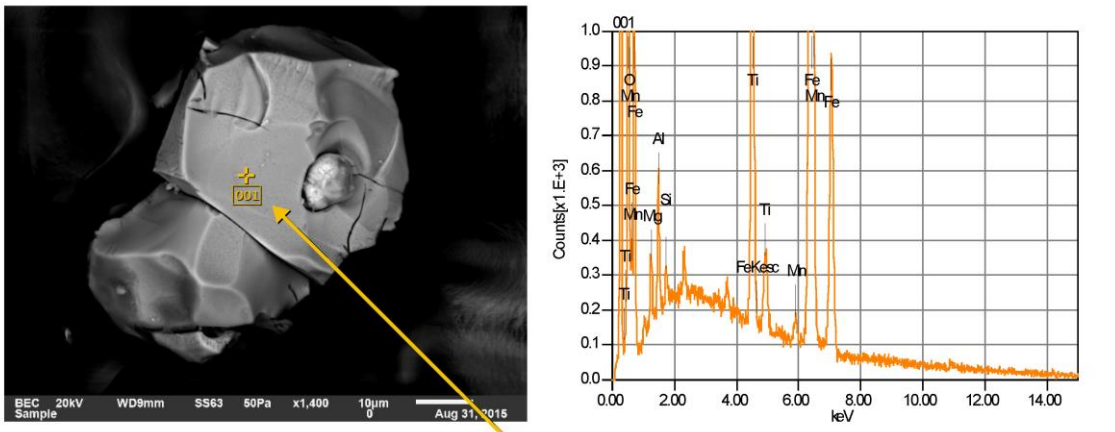

Volt	: 20.00 kV	Acquisition Condition		Formula	mass%	Atom%	Sigma	Net	K ratio	Line
Mag.	: x 1,400	Instrument	: 6510(LA)	O	18.92	43.75	0.04	95472	0.2658468	K
Date 2015/08/31	:	Volt	: 20.00 kV	Mg	0.83	1.26	0.03	6849	0.0062395	K
		Current	: ---	Al	1.13	1.55	0.02	13084	0.0116926	K
Pixel 960	: 1280 x	Process Time	: T4	Si	0.27	0.36	0.02	3730	0.0037317	K
		Live time sec.	: 30.00	Ti	7.71	5.96	0.04	91751	0.1890266	K
				Mn	0.74	0.50	0.03	5599	0.0172636	K
		Real Time sec.	: 35.94	Fe	70.39	46.62	0.11	470146	1.6766249	K
				Total	100.00	100.00				

Figure S8. SEM-EDS of 65-μm-long titano-magnetite grain with a reduced oxygen content of ~19%, Fe content of ~70%, and Ti content of ~8%. From the 552-cm YDB layer.

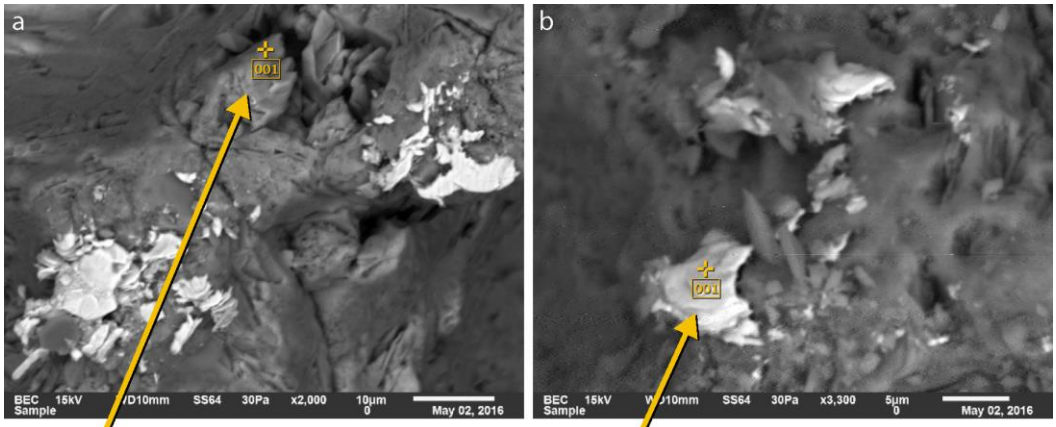

Formula	mass%	Atom%	Sigma	Net	K ratio
C	7.99	13.24	0.02	12603	0.0092396
O	46.66	58.05	0.06	258090	0.6200907
Mg	8.12	6.65	0.03	125121	0.1557184
Al	2.32	1.71	0.02	37930	0.0487914
Si	19.05	13.50	0.06	323857	0.4648675
Ca	8.55	4.24	0.04	91080	0.2707536
Fe	7.31	2.61	0.06	24675	0.1994431
Total	100.00	100.00			

Formula	mass%	Atom%	Sigma	Net	K ratio
O	7.03	19.39	0.05	28720	0.1241079
Al	2.57	4.21	0.05	15491	0.0358409
Si	5.53	8.69	0.06	36898	0.0952589
Cr	10.08	8.56	0.09	28008	0.2774831
Fe	74.79	59.14	0.23	124941	1.8163359
Total	100.00	100.00			

Figure S9. Basaltic matrix and chromium-magnetite inclusions. ***a)*** Spot SEM-EDS at yellow arrow indicates basaltic glass composed mainly of Si, Ca, Mg, Fe, and O. Ca is a typical component in Andean lavas whose origin is the subduction-arc complex along the Pacific coast of South America. The volcanic matrix contains no detectable chromium. ***b)*** Spot SEM-EDS at yellow arrow indicates bright metallic inclusions of chromium magnetite, composed of ~75% iron and ~10% chromium. There is no indication of rapid melting and quenching of these plate-like inclusions. Instead, they crystallized slowly from molten magma.

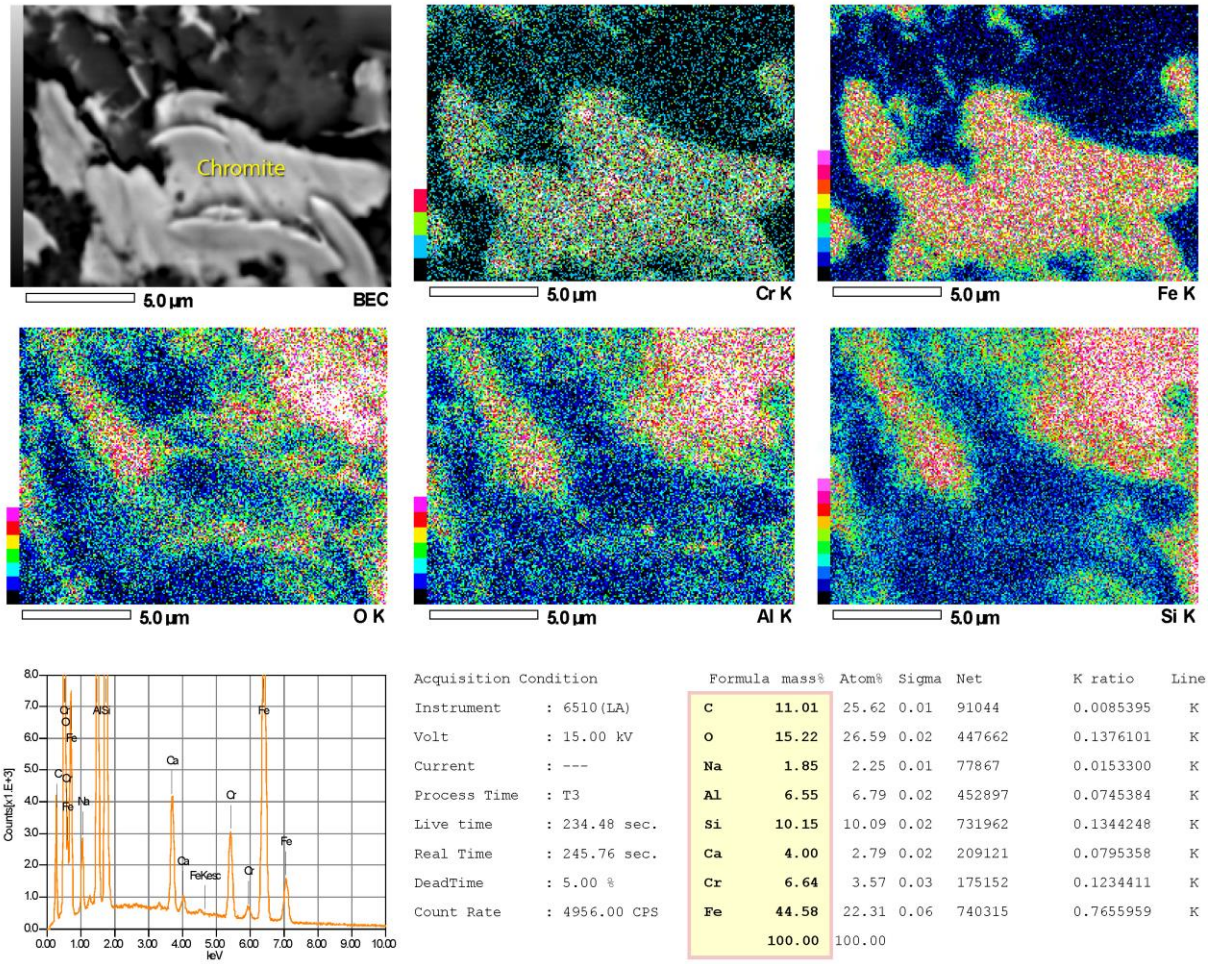

	Formula mass%	Atom%	Sigma	Net	K ratio	Line
C	11.01	25.62	0.01	91044	0.0085395	K
O	15.22	26.59	0.02	447662	0.1376101	K
Na	1.85	2.25	0.01	77867	0.0153300	K
Al	6.55	6.79	0.02	452897	0.0745384	K
Si	10.15	10.09	0.02	731962	0.1344248	K
Ca	4.00	2.79	0.02	209121	0.0795358	K
Cr	6.64	3.57	0.03	175152	0.1234411	K
Fe	44.58	22.31	0.06	740315	0.7655959	K
	100.00	100.00				

Figure S10. SEM-EDS elemental map of chromium magnetite. Analysis shows that bright areas in the upper left panel are metallic inclusions composed almost exclusively of chromium magnetite.

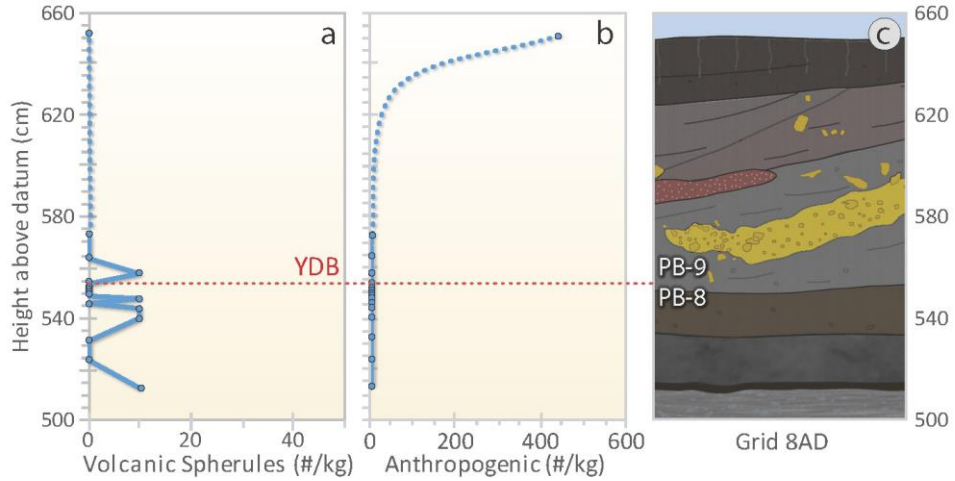

Figure S11. Volcanic and anthropogenic spherules. ***a)*** Volcanic spherules are randomly distributed throughout the profile in low quantities, ranging from 0 to ~10 spherules/kg. None were found in the YDB layer. ***b)*** Anthropogenic spherules are present only at the surface, and not in other samples. ***c)*** Stratigraphic profile of grid 8AD, where volcanic and anthropogenic spherules were collected.

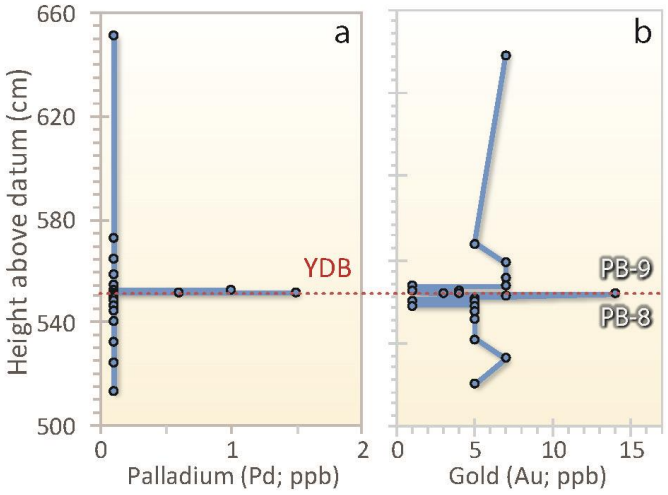

Figure S12. Palladium and gold concentrations. ***a)*** Palladium (Pd) concentrations are anomalously high at the YDB layer. ***b)*** Gold (Au) concentrations are also anomalously high at the YDB layer. The concentrations of Pt, Pd, and Au are much higher than background concentrations, suggesting a non-local source of these elements.

SUPPLEMENTARY INFORMATION: Tables

Table S1. Age span of YDB sequences previously investigated. The time-series samples analyzed from 24 YDB sites have a mean age span of 7,016 calendar years with a maximum span of ~21,375 calendar years. The age of sediment samples at Pilauco span 5,719 calendar years. Sampling in nearly all these studies was discontinuous, except across the YDB layer, leading some to argue that this makes it difficult to determine whether the inferred impact assemblage is unique to the entire record.

Site	Boundary (cal BP)	Boundary (cal BP)	Span (years)
Aalsterhut	12619	12815	196
Abu Hureyra	11316	12917	1601
Arlington Canyon	12613	12835	222
Barber Creek	9770	14995	5225
Big Eddy	11235	14705	3470
Blackville	600	19620	19020
Blackwater Draw	7035	14980	7945
Bull Creek	7110	12890	5780
Daisy Cave	2316	14105	11789
Indian Creek	7690	13290	5600
Lake Cuitzeo	~10000	~21000	~11000
Lake Hind	2730	12745	10015
Lindenmeier	9965	14970	5005
Lingen	12330	13605	1275
Lommel	11660	15390	3730
Melrose	1640	12255	10615
Mucunuque	12845	14000	1155
Murray Springs	5515	26890	21375
Ommen	10395	13990	3595
Pilauco	**10272**	**15991**	**5719**
Santa Maira	5330	17405	12075
Sheriden Cave	9845	14555	4710
Talega	10335	19530	9195
Topper	3255	15305	12050
MEAN SPAN			**7016**
MAX SPAN			**21375**

Table S2. Sedimentology. Textural parameters of units PB-7, PB-8 and PB-9 exposed in grid 14AD. Weight percentages of sand (sieved from 2000 to 62.5 μm), mud (<62.5 μm) and organic matter (whole sample, from LOI) for units PB-7, PB-8 and PB-9, grid AD14. The percentages were calculated with the exclusion of gravel (see main manuscript).

Percentage		PB-7	PB-8	PB-9
Thickness	cm	10 to 75	25 to 100	25 to 150
Color	Munsell	2.5Y 3/2	2.5Y 4/2	2.5Y 2/0
Sand	mean %	70.7	63.9	74.4
Range:	S.D. %	10.6	13.2	11.6
62.5 to	max %	93.6	84.6	90.3
2000 μm	min %	25.6	34.9	21.4
Mud	mean %	16.3	23.6	16.2
Range:	S.D. %	8.2	12.3	10.3
<62.5 μm	max %	55.0	50.5	61.6
	min %	1.0	3.1	3.6
Organics	mean %	12.9	12.6	9.4
Based on	S.D. %	5.7	3.2	2.4
LOI	max %	62.3	21.7	17.1
	min %	1.9	2.7	4.1

Table S3. Granulometry for Lenses A-F. See legend in **Figure 2** in main manuscript.

Lens	Sand (%)	Mud (%)	Gravel (%)	Rock (%)
A	63	37	--	--
B	58	42	--	--
C	60	40	--	--
D	11	8	66	15
E	10	90	--	--
F	4	96	--	--

Table S4. Radiocarbon dates from Pilauco. Calibrated using Southern Hemisphere curve, SHCal13, within OxCal, version 4.3.2.

Lab #	Material	Elev. (cm)	^{14}C Age	Err	SHCal13	SHCal13	Layer	Grid #	Source
UCIAMS110206	seed	639	9135	20	10240	22	PB-9	14AD	This paper
AA108167	charcoal	542	10416	38	12221	112	PB-9	10AC	This paper
AA81809	charcoal	560	10517	150	12310	228	PB-9	6E	Pino 2013
AA81805	wood	550	10630	124	12469	178	PB-9	E9	Pino 2013
UCIAMS101668	charcoal	576	10660	30	12603	44	PB-9	14AD	This paper
UCIAMS101684	wood	576	10710	30	12643	41	PB-9	14AD	This paper
UCIAMS101669	plant remains	560	10950	30	12764	34	PB-9	14AD	This paper
AA81806	wood	545	10739	128	12591	147	PB-8	E9	Pino 2013
AA81812	coprolite	505	11004	186	12876	163	PB-8	7AC	Pino 2013
AA108168	plant remains	505	11079	40	12899	72	PB-8	14AD	This paper
AA81804	wood	467	11122	178	12958	156	PB-8	E9	Pino 2013
AA81810	tooth	446	11457	140	13265	132	PB-8	7G	Pino 2013
AA81807	wood	430	11665	136	13460	142	PB-8	E9	Pino 2013
AA81808	wood/charcoal	426	11834	186	13655	213	PB-8	E9	Pino 2013
AA108170	plant remains	420	12173	42	13995	87	PB-7	14AD	This paper
TO11477	bone	357	12540	90	14684	242	PB-7	11H	Pino 2013
UCIAMS101771	seed	352	12735	40	15109	98	PB-7	14AD	This paper
UCIAMS101830	bone	416	12760	50	15142	101	PB-7	15AD	This paper
UCIAMS101670dup	bone	416	12725	40	15142	101	PB-7	15AD	This paper
UCIAMS101672	wood	352	12860	35	15277	88	PB-7	14AD	This paper
UCIAMS101685	bone	401	12905	40	15352	106	PB-7	15AD	This paper
UCIAMS110204	wood	403	12935	25	15393	98	PB-7	14AD	This paper
UCIAMS101768	bone	401	13010	35	15501	110	PB-7	15AD	This paper
UCIAMS101770	seed	353	13045	30	15552	111	PB-7	14AD	This paper
UCIAMS101673	charcoal	352	13145	35	15723	105	PB-7	14AD	This paper
UCIAMS101832	bone	318	13165	55	15750	123	PB-7	15AC	This paper
UCIAMS101769	seed	352	13175	40	15772	103	PB-7	14AD	This paper
UCIAMS101674	wood	351	13195	35	15804	94	PB-7	14AD	This paper
UCIAMS101831	bone	400	13220	60	15834	116	PB-7	15AD	This paper
UCIAMS102087	bone	318	13220	40	15838	95	PB-7	15AC	This paper
AA91450	wood	340	13332	72	15979	122	PB-7	12F	This paper
UCIAMS101671	sediment	353	13470	35	16154	85	PB-7	14AD	This paper
UCIAMS110203	seed	339	13570	70	16299	128	PB-7	14AD	This paper
UCIAMS110205	seed	417	13650	70	16410	133	PB-7	14AD	This paper
UCIAMS101675	wood	330	14195	40	17233	103	PB-6	12F	This paper
UCIAMS101676	wood	328	14300	40	17362	99	PB-6	12F	This paper

Table S5. Bayesian age calculations. Green line represents YDB at PB-8/PB-9 boundary at ~12,770 cal yr BP. Calculated using OxCal 4.3.3. with SHCal13 calibration curve.

	Unmodelled (BP)							Modelled (BP)		Indices: Amodel 95.5; Aoverall 96.1				
Depth_Model	mu	sigma	68% from	68% to	95% from	95% to	%	68% from	68% to	95% from	95% to	mu	sigma	A
Outlier_Model Charcoal								-384	212	-1117	303	-221	415	
Exp(1,-10,0.5)	-0.5532	0.9981	-0.655	0.4475	-2.6815	0.4475	95.4					-0.51586	0.959	
U(0,3)	1.515	0.866	2.21E-17	3	2.21E-17	3	95.4	2.538	2.82	2.391	2.931	2.65971	0.135	100
P_Sequence Pilauco														
Boundary								10508	10059	10508	9965	10272	150	
R_Date UCIAMS110206	10240	22	10250	10225	10277	10198	95.4	10508	10059	10508	9965	10272	150	98.3
R_Date UCIAMS101684	12643	41	12687	12570	12706	12560	95.4	12813	12543	12906	12194	12637	168	99.6
R_Date UCIAMS101668	12603	44	12653	12560	12675	12451	95.4	12831	12573	12917	12252	12664	152	100.9
R_Date UCIAMS101669	12764	34	12788	12725	12828	12706	95.4	12868	12620	13019	12255	12703	154	101.5
R_Date AA108168	12899	72	12978	12825	13039	12761	95.4	13071	12746	13219	12488	12890	168	100.6
R_Date AA108170	13995	87	14105	13930	14150	13815	95.4	14258	13746	14391	13107	13901	308	101.4
R_Date UCIAMS110205	16410	133	16522	16264	16683	16155	95.4	15463	14989	15554	13861	15047	414	100.6
R_Date UCIAMS110204	15393	98	15473	15274	15591	15223	95.4	15451	15143	15555	14597	15223	219	102.4
R_Date UCIAMS101672	15277	88	15336	15179	15474	15111	95.4	15437	15253	15555	15148	15344	99	104.8
R_Date UCIAMS101671	16154	85	16242	16076	16321	15977	95.4	15439	15255	15556	15164	15353	90	98.3
R_Date UCIAMS101770	15552	111	15680	15445	15750	15332	95.4	15440	15260	15556	15164	15355	90	97
R_Date UCIAMS101769	15772	103	15871	15674	15989	15572	95.4	15440	15258	15556	15163	15356	90	98.6
R_Date UCIAMS101673	15723	105	15825	15630	15945	15505	95.4	15442	15259	15566	15164	15359	89	96.7
R_Date UCIAMS101771	15109	98	15218	15046	15290	14890	95.4	15445	15277	15567	15164	15360	89	84.5
R_Date UCIAMS101674	15804	94	15894	15709	16001	15626	95.4	15877	15254	16027	15214	15568	234	99.7
R_Date UCIAMS110203	16299	128	16410	16159	16562	16048	95.4	16326	15668	16494	15668	15991	263	100.3
Boundary								16326	15668	16494	15668	15991	263	

Table S6. Pilauco spherule groups. Elevations and abundances of five groups of spherules. Group 6, detrital grains, is not shown.

Layer	Bottom (cm)	Group 1 MSp/kg	Group 2 Cr-rich/kg	Group 3 Volc/kg	Group 4 Framboids	Group 5 Anthro
PB9	651	0	0	0	0	440
PB9	572	0	0	0	0	0
PB9	564	0	0	0	0	0
PB9	558	10	0	10	0	0
PB9	554	120	0	0	80	0
PB9	552	520	115	0	30	0
PB9	551	20	0	0	0	0
PB9	550	60	0	0	0	0
PB9/8	549.5	0	0	0	0	0
PB8	549	0	0	0	0	0
PB8	548	0	0	10	0	0
PB8	546	0	0	0	0	0
PB8	544	0	0	10	0	0
PB8	540	0	0	10	0	0
PB8	532	0	0	0	0	0
PB8	524	0	0	0	0	0
PB8	513	0	0	10	0	0

Table S7. SEM-EDS analyses of Pilauco spherules. "Y" represents Group 1 YDB spherules; "C" are Group 2 Cr-rich spherules; "B" are Group 3 volcanic spherules; and "A" series represent Group 5 anthropogenic spherules. Composition of Group 4 framboids are discussed in the main manuscript.

Group	Name	#	DIAM	Na2O	MgO	Al2O3	SiO2	P2O5	SO3	K2O	CaO	TiO2	Cr2O3	MnO	FeO
Group 1	Y1	552c 6-40 µm	40	0.00	0.00	0.00	7.60	0.00	0.00	0.00	0.00	0.00	0.00	0.00	92.40
	Y2	552c 5-29 µm	29	0.00	0.00	0.00	10.74	0.00	0.00	0.00	0.00	0.00	0.00	0.00	89.26
	Y3	552c 2-34 µm	34	0.00	0.00	0.00	13.42	0.00	0.00	0.00	0.00	0.00	0.00	0.00	86.58
	Y4	552b 1-40 µm	40	0.00	0.00	0.00	1.24	0.00	0.00	0.00	0.00	0.00	0.00	0.00	98.76
	Y5	552a 5-56 µm	56	0.00	0.00	0.00	2.24	0.00	0.00	0.00	0.00	0.00	0.00	0.00	97.76
	Y6	552a 4-95 µm	95	0.00	0.00	0.00	1.11	0.00	0.00	0.00	0.00	0.00	0.00	0.00	98.89
	Y7	552a 3-76 µm	76	0.00	0.00	0.00	2.64	0.00	0.00	0.00	0.00	0.00	0.00	0.00	97.36
	Y8	552a 1-40 µm	40	0.00	0.00	0.00	0.00	0.00	0.00	0.00	0.00	0.00	0.00	0.00	100.00
	Y9	550 2-38b µm	38	0.00	0.00	0.00	9.52	0.00	0.00	0.00	0.00	0.00	0.00	0.00	90.48
	Y10	550 2-38a µm	38	0.00	0.00	0.00	9.63	0.00	0.00	0.00	0.00	0.00	0.00	0.00	90.37
	Y11	550 1-28 µm	28	0.00	0.00	0.00	11.23	0.00	0.00	0.00	0.00	0.00	0.00	0.00	88.78
Group 2	C1	552c 4-45d µm	45	0.00	0.00	0.00	14.27	0.00	0.00	0.00	0.00	6.19	3.92	0.00	75.62
	C2	552c 4-45c µm	45	0.00	0.00	0.00	9.61	0.00	0.00	0.00	0.00	7.38	3.97	0.00	79.03
	C3	552c 4-45b µm	45	5.09	3.13	4.49	11.52	0.00	0.00	0.00	0.00	8.10	4.45	0.00	63.22
	C4	552c 4-45a µm	45	0.00	3.47	8.20	9.87	0.00	0.00	0.00	0.00	8.58	4.45	0.00	65.43
	C5	552c 3-42 µm	42	0.00	0.00	0.00	11.43	0.00	0.00	0.00	0.00	0.00	14.30	0.00	74.27
Group 3	B1	544 1-34 µm	34	5.16	0.70	20.13	60.97	0.00	1.47	0.31	7.68	0.70	0.00	0.00	2.88
	B2	540 2-27 µm	27	1.08	0.86	2.94	16.96	0.00	1.14	0.34	1.17	19.84	0.00	0.00	55.67
	B3	513b 1-300 µm	300	0.74	3.06	2.24	24.28	3.54	31.35	0.00	34.79	0.00	0.00	0.00	0.00
Group 5	A1	651 9-29 µm	29	0.46	0.00	0.40	5.72	0.00	0.00	0.00	0.45	0.00	0.00	0.25	92.73
	A2	651 8-31 µm	31	0.30	0.00	0.00	6.86	0.00	0.00	0.00	0.42	0.00	0.00	0.61	91.81
	A3	651 7-37 µm	37	0.79	0.00	0.00	8.84	0.00	0.00	0.00	0.00	0.00	0.00	0.20	90.16
	A4	651 6-39 µm	39	0.82	0.00	0.00	11.56	0.00	0.00	0.00	0.00	0.00	0.00	0.30	87.32
	A5	651 5-38 µm	38	0.81	0.00	0.00	9.73	0.00	0.00	0.00	0.43	0.00	0.00	0.26	88.77
	A6	651 4-36 µm	36	0.85	0.00	0.00	6.85	0.00	0.00	0.00	0.60	0.00	0.00	0.04	91.66
	A7	651 3-33 µm	33	1.05	0.00	0.00	7.13	0.00	0.00	0.00	0.38	0.00	0.00	0.17	91.27
	A8	651 2-34 µm	34	1.08	0.00	0.00	11.03	0.00	0.00	0.00	0.41	0.00	0.00	0.09	87.40
	A9	651 1-27 µm	27	0.99	0.00	0.00	9.19	0.00	0.00	0.00	0.51	0.00	0.00	0.56	88.76
	A10	651 10-39 µm	39	1.31	0.00	0.19	11.30	0.00	0.00	0.00	0.36	0.00	0.00	0.37	86.47
	A11	550 3-32 µm	32	0.50	0.00	0.00	11.75	0.00	0.00	0.00	0.57	0.00	0.00	0.88	86.30
	A12	540 1-19 µm	19	0.61	0.00	0.59	12.53	0.00	0.00	0.00	0.48	0.00	0.00	0.12	85.69
	A13	532 1-34 µm	34	1.30	0.00	1.11	4.44	0.00	0.00	0.00	0.56	0.00	0.00	0.41	92.17

Table S8. Characteristics of spherulitic particles. Categorized by geochemistry, morphology, texture, and level. Gold highlighted areas indicate some characteristics used to differentiate types.

Type of Object	Comp.	Geochemistry	Morphology	Texture	Level
Anthropogenic	Iron	FeO w/ 0.4-0.8 wt.% Mn	Round-subround	Dendritic	Surficial
Anthropogenic	Glass	Mostly SiO_2	Round-subround	Smooth/vesicular	Surficial
Cosmic	Glass	>10% MgO	Round-subround	Dendritic	Any level
Cosmic	Iron	>5 wt.% Ni	Round-angular	Smooth/vesicular	Any level
Detrital magnetite	Iron	Fe_3O_4, often +Ti, Mg	Subround-angular	Often flat/concave facets	Any level
Detrital quartz	Glass	100 wt.% SiO_2	Subround-angular	Lunate fractures	Any level
Framboidal	Iron	Usually FeS_2	Round-subround	Blocky crystals	~Lacustrine
Volcanic	Glass	>9 wt.% CaO; >2 wt.% Na_2O	Round-subround	Smooth/vesicular	Any level
YDB impact	Iron	FeO + minor elements	Round-subround	Dendritic	~12,800 cal BP
YDB impact	Glass	SiO_2 +minor elements	Round-subround	Often vesicular	~12,800 cal BP

Table S9. Platinum (Pt), palladium (Pd), and gold (Au) concentrations by unit and elevation (cm).

Layer	Elev. (cm)	Au ppb	Pt ppb	Pd ppb
PB9	651.0	7.0	4.4	<0.1
PB9	572.0	5.0	3.6	<0.1
PB9	564.0	7.0	4.7	<0.1
PB9	558.0	7.0	5.1	<0.1
PB9	554.0	7.0	5.4	<0.1
PB9	554.0	<1	<0.1	<0.1
PB9	552.0	<1	<0.1	<0.1
PB9	552.0	4.0	0.5	1.0
PB9	552.0	1.0	1.0	0.1
PB9	552.0	1.0	1.0	<0.1
PB9	551.0	3.0	0.7	0.6
PB9	551.0	4.0	0.8	1.5
PB9	551.0	14.0	9.9	<0.1
PB9	550.0	7.0	5.1	<0.1
PB9	549.5	5.0	3.5	<0.1
PB8	549.0	5.0	3.9	<0.1
PB8	548.0	5.0	3.3	<0.1
PB8	548.0	1.0	1.0	<0.1
PB8	546.0	<1	1.0	<0.1
PB8	546.0	5.0	4.4	<0.1
PB8	544.0	5.0	3.7	<0.1
PB8	540.0	5.0	3.1	<0.1
PB8	532.0	5.0	3.7	<0.1
PB8	524.0	7.0	4.5	<0.1
PB8	513.0	5.0	3.3	<0.1

Table S10. Distribution of seeds and cuticles. Categorized by whether abundances were higher pre-YDB (blue), higher post-YDB (orange), or remained mostly the same throughout the profile. Red line represents PB-8/PRB-9 YDB boundary.

	LAYER:	--	PB9	PB9	PB9	PB9	PB9	PB9	PB9	PB9	PB9	PB9	PB8	PB8	PB8	PB8	PB8	PB8	PB8	PB8	PB8	PB8	--
Higher Pre-YDB		651	572	568	564	560	558	556	554	552	551	550	549	548	546	544	542	540	536	532	528	524	513
A. chilensis	Seeds	1	0	0	0	0	0	0	0	1	0	0	0	2	1	1	0	2	6	0	0	4	1
Cyperaceae-1	Seeds	0	0	0	0	0	0	0	0	0	0	1	1	0	9	3	2	0	1	0	2	2	1
Cyperaceae-2	Seeds	0	0	0	0	0	0	0	0	0	0	0	1	2	0	2	5	0	5	0	3	3	8
Cyperaceae-3	Seeds	0	0	0	0	0	0	0	0	0	0	1	4	1	59	5	8	4	9	0	8	7	7
M. fontana	Seeds	0	0	0	0	0	0	0	0	0	4	0	33	29	43	33	41	47	65	0	79	80	150
P. andina	Seeds	0	0	0	0	1	0	0	0	0	0	0	0	1	2	0	0	0	1	2	0	3	1
Poaceae glumas	Seeds	0	0	0	0	0	0	0	0	0	0	2	40	13	1	42	32	20	42	0	65	74	160
Portucalaceae-3	Seeds	0	0	0	0	0	0	0	0	0	0	0	3	2	0	5	2	0	0	0	5	3	6
Portucalaceae-4	Seeds	0	0	0	0	0	0	0	0	0	0	0	0	0	0	0	2	0	0	0	0	0	0
T. stipularis	Seeds	0	0	0	0	0	0	0	0	0	0	0	0	0	1	0	1	0	0	0	1	0	0
E. coccineum	Cuticles	--	--	--	--	--	--	--	--	--	--	--	Y	Y	--	Y	Y	Y	Y	Y	Y	--	--
L. hirsuta	Cuticles	--	--	--	--	--	--	--	--	--	--	--	--	--	Y	--	Y	Y	Y	--	Y	Y	Y
TOTALS		**1**	**0**	**0**	**0**	**1**	**0**	**0**	**0**	**1**	**4**	**4**	**82**	**50**	**116**	**91**	**91**	**73**	**129**	**2**	**163**	**176**	**334**
Higher Post-YDB		651	572	568	564	560	558	556	554	552	551	550	549	548	546	544	542	540	536	532	528	524	513
Portucalaceae-1	Seeds	0	0	21	0	16	0	14	0	0	0	0	0	0	0	0	0	0	2	0	0	0	0
Portucalaceae-2	Seeds	0	0	61	0	0	5	0	5	0	0	35	0	0	0	0	0	0	0	0	0	1	0
Cyperaceae4	Seeds	0	0	0	0	0	0	0	0	0	0	1	0	0	0	0	0	0	0	0	0	0	0
TOTALS		**0**	**0**	**82**	**0**	**16**	**5**	**14**	**5**	**0**	**0**	**35**	**0**	**0**	**0**	**0**	**0**	**0**	**2**	**0**	**0**	**1**	**0**
Throughout		651	572	568	564	560	558	556	554	552	551	550	549	548	546	544	542	540	536	532	528	524	513
Uncinia	Seeds	0	0	1	0	0	3	2	1	1	4	0	10	3	0	0	1	0	1	0	0	0	1
G.tinctoria	Seeds	0	0	1	0	1	0	1	0	0	2	1	8	3	1	4	0	1	1	0	3	0	1

Table S11. Negative binomial generalised regression models calculated using the number of seeds present in units PB-8 and PB-9 at the Pilauco site. Model 1 refers to the complete model including an interaction term between the explanatory variables layer and sample size (model with the highest Akaike information criterion (AIC)); Model 2 is the additive model without the interaction term; Model 3 is the reduced model containing only the seed source ("Layer") as the explanatory variable, and it was the best model based on lower AIC.

	Dependent variable: Number of seeds		
Variables	**Model 1**	**Model 2**	**Model 3**
Layer	2.619*	2.390*	2.380*
	-0.909	-0.381	-0.383
Sample thickness	0.113	0.071	--
	-0.226	-0.159	--
Layer thickness	-0.088	--	--
	-0.317	--	--
Constant	3.229*	3.340*	3.532*
	-0.65	-0.495	-0.273
Observations	22	22	22
Log Likelihood	-129.028	-129.07	-129.176
Theta	1.411*	1.406*	1.393*
	-0.43	-0.428	-0.423
AIC	270.056	268.139	266.351
Significance values:	*p<0.01	**p<0.05	***p<0.1

Table S12. Distribution of pollen from grid 10AD. Columns marked on blue are pre-YDB pollen samples (548-550 cm); columns marked in red are post-YDB (550-557 cm). Red line indicates PB-8/PB-9 boundary. Post/Pre-YDB Ratio is the relation between Post-YDB and Pre-YDB mean pollen/spores abundances (%). Ratios > 1 mean the increase of the taxa after YDB. Ratios <1 means the decrease of the taxa after YDB. Ratios ~1 mean non-change. Shannon diversity index (H) and species richness (S) are based on raw data of all pollen and fern taxa, indicating lower richness and diversity after YDB. Vegetation turnover index is computed using the difference between contiguous samples scores of DCA Axis 1 of all pollen samples; values = 0 means no changes on vegetation, whereas values > 0 indicate a species turnover. At the YDB the vegetation turnover index increase from 0 to 0,4 supporting the vegetation change. The climatic inference based on selected taxa marked on black, indicate the dominance of open landscape during the whole section under wet/cold-temperate conditions before the YDB and the increase in seasonality of precipitation and warmer conditions after the YDB.

10AD grid	Group	548	549	550	551	552	553	554	555	556	557	Pre-YDB	Post-YDB	Post-/Pre-YDB	Climate
Taxa name	taxa		Pre-YDB					Post-YDB				avg.	avg.	Ratio	
	Ht. (cm)														
Azara	tree	0.9	0.5	1.5	0	0	0	0	0	0	0	0.97	0.00	0.0	**Wet and**
Nothofagus obliqua-type	tree	0	0	0.2	0	0	0	0	0	0	0	0.07	0.00	0.0	**cold**
Tepuallia stipularis	tree	0.6	1.7	1.1	0	0	0	0	0	0	0	1.13	0.00	0.0	
Podocarpus nubigena	tree	0.3	0.7	0	0	0	0	0	0	0	0	0.33	0.00	0.0	
Pilgerodendron/Fitzroya	tree	2.6	1.2	1.1	1.4	0	1.7	1.3	1.6	0	0	1.63	0.86	0.5	
Raukaua latervirens	vine	3.4	0.5	1.5	0	0	0	0	0	0	1.1	1.80	0.16	0.1	
Maytenus	tree	14	12.7	5.6	4.3	1.8	1.7	7.9	0	1.3	4.3	10.77	3.04	0.3	
Nothofagus dombeyi-type	tree	2.6	3.1	1.9	1.4	0	1.7	0	0	0	3.3	2.53	0.91	0.4	
Gesneriaceae	vine	0.9	0	1.7	0	0	0	0	1.6	0	1.1	0.87	0.39	0.4	
Escallonia	tree	1.1	0.7	1.7	0	0	0	2.6	0	0	1.1	1.17	0.53	0.5	
Myrtaceae	tree	10.6	14.4	19.3	17.4	1.8	5.1	5.3	6.5	10.4	4.3	14.77	7.26	0.5	
Apiaceae	herb	2.3	3.8	6	0	1.8	1.7	1.3	1.6	0	1.1	4.03	1.07	0.3	
Adenocaulon	herb	3.4	2.2	0.6	0	0	0	1.3	0	0	0	2.07	0.19	0.1	
Cyperaceae	aquatic	1.3	5.1	1	1.2	1.3	1	0	1	0	0.7	2.47	0.74	0.3	
Isoetes	fern	0.3	1.2	0.2	0	0	0	0	0	0	0	0.57	0.00	0.0	
Terrestrial pollen conc.		58595	90106	57731	7084	5243	5322	6539	4821	7172	8422	68811	6372	0.1	
Hydrangea	tree	1.4	1.9	0.4	0	0	0	0	1.6	2.6	4.3	1.23	1.21	1.0	**Non-**
Tree sum	tree	51.7	50.4	55.2	56.5	33.9	44.1	43.4	50	37.7	39.1	52.43	43.53	0.8	**Change**
Brassicaceae	herb	1.4	0.7	0.6	1.4	1.8	0	0	0	0	1.1	0.90	0.61	0.7	**Taxa**
Poaceae	herb	32.9	34.8	25.8	30.4	50	33.9	30.3	25.8	37.7	48.9	31.17	36.71	1.2	**Season-**
Herb sum	herb	48.3	49.6	44.8	43.5	66.1	55.9	56.6	50	62.3	60.9	47.57	56.47	1.2	**ality of**
Aextoxicon	tree	2.6	1.9	3.6	2.9	3.6	3.4	2.6	6.5	3.9	2.2	2.70	3.59	1.3	**precipi-**
Eucryphia/Caldcluvia	tree	0.6	0.7	0.6	2.9	1.8	0	0	1.6	0	0	0.63	0.90	1.4	**tation**
Gunnera	shrub	0.3	0	0.2	0	0	0	0	1.6	0	0	0.17	0.23	1.4	**and**
Weinmannia trichosperma	tree	1.1	2.9	2.6	7.2	3.6	3.4	3.9	4.8	3.9	1.1	2.20	3.99	1.8	**warmer**
Saxegothaea conspicua	tree	2	3.4	2.4	2.9	5.4	3.4	3.9	12.9	5.2	4.3	2.60	5.43	2.1	**temper-**
Prumnopitys andina	tree	0.6	0.2	0	1.4	0	3.4	3.9	1.6	2.6	1.1	0.27	2.00	7.5	**atures**
Laureliopsis	tree	0.9	0	0	0	0	3.4	0	0	0	1.1	0.30	0.64	2.1	
Drymis	tree	0	0	0	0	0	1.7	0	4.8	0	0	0.00	0.93	>1.5	
Aristotelia	tree	0.9	1	4.9	14.5	12.5	10.2	7.9	3.2	5.2	6.5	2.27	8.57	3.8	
Asteroideae subfam	herb	1.1	0.7	3	8.7	7.1	5.1	7.9	12.9	13	4.3	1.60	8.43	5.3	
Triglochin type	aquatic	0.5	1	1.6	7.1	10.4	19.2	25.5	17.5	9.9	7.9	1.03	13.93	13.5	
Aquatic sum	aquatic	4.7	7.6	2.6	12.9	14.3	20.2	25.5	20.6	10.7	10.8	4.97	16.43	3.3	
Polypodium fullei	fern	2.9	2.1	0.4	1.2	2.6	3	1.5	3.1	5.8	4.3	1.80	3.07	1.7	
Blechnum type	fern	0	1	2.2	3.5	10.4	11.1	12.4	12.4	15.7	18	1.07	11.93	11.2	
Fern sum	fern	3.9	6.8	3.6	5.9	13	20.2	19	15.5	25.6	23	4.77	17.46	3.7	
Shannon diversity (H)		2.9	2.8	2.9	2.5	2.2	2.8	2.7	2.7	2.6	2.5	2.9	2.6	0.9	
Species richness (S)		47	49	48	22	18	26	26	25	23	29	48	24	0.5	
DCA Axis 1		-0.65080	-0.65300	-0.63718	-0.32445	0.06801	-0.07171	-0.00313	-0.11007	0.07199	0.12226				
Vegetation turnover index		0.0	0.0	0.0	0.3	0.4	0.1	0.1	0.1	0.2	0.1				

Table S13. Summary of regional vegetation assemblages and environmental/climatic interpretation.

Site (proxy)	Location	Pollen Zone & thickness	^{14}C kyr B.P.	Cal kyr B.P	Vegetation assemblage	Environmental conditions and interpretation
Huelmo mire (pollen, microscopic charcoal) [Hajdas 2003; Moreno & Leon 2003; Moreno 2001]	41°31 S/73° W (~10 m a.s.l.)		13-12.4	15.8-14.2	From 12.4 ^{14}C kyr BP Expansion of *Podocarpus nubigena* element of the North Patagonian evergreen rainforest.	At 13 ^{14}C kyr BP near modern climate conditions followed by down valley movement of vegetation belts in response to cooling.
		"Final cooling phase" (794-722 cm depth)	11.4-9.8	13.4-12.6	11.4-10.8 ^{14}C kyr BP expansion *N. dombeyi*-type, and increase in *P. nubigena*. After the increase of cold resistant species, between 11.4-10.8 ^{14}C yr BP, opportunistic plant species and colonizers of disturbed soil are recorded.	Sub-centennial variability in precipitation values, together with stand-replacing fires.
Lake Mascardi (pollen, grain size, TOC, and HI) [Hajdas 2003; Ariztequi 1997]	41°08 S/71°34 W (800 m a.s.l.)	Phase 2	12.4-11.5	14.2-13.3	*N. dombeyi*- type and open ground taxa: Poaceae, Asteraceae, *Pernettya/Gaultheria*.	Near modern? Max values of grain size, TOC and HI. Retreat of Tronador ice cap.
		Phase 3: "Final cooling phase" (820-752 cm)	11.5-10.2	13.5-11.7	Expansion of Chenopodiaceae-Amaranthaceae pollen, upland herbs, and *Isoetes*. Decreased pollen influx, *N. dombeyi*-type pollen abundance, and reversal in HI.	Increased erosion and glacier advance under lower temperature and precipitation (Ariztegui et al 1997).
Lake Lepué (pollen, charcoal)[Pesce 2014]	42°48 S/73°42 W (124 m a.s.l.)	Zone LL3 (1074-1026 cm depth)		15.8-14.6	*Nothofagus*-Myrtaceae-*Fitzroya/Pilgerodendron* assemblage. *R.laetevirens*, Myrtaceae and *Drimys* reach max. representation, while Poaceae, *Fitzroya/Pilgerodendron,* Ericaceae, *Blechnum, L. magellanicum* and *Isoetes* almost disappear.	Rapid establishment of closed-canopy North Patagonian rainforests, warmer conditions between 16-14.6 cal yr BP.
		Zone LL4 (1026-949 cm depth)		14.6-12.9	*Nothofagus*-Myrtaceae-*P.nubigena*. Rapid/large- magnitude increase of the cold-resistant hygrophilous conifer *P. nubigena* max abundance (35%). between 14.6-12.7 cal kyr BP along with the vine Hydrangea. Other trees and climbers (*Fitzroya /Pilgerodendron*, *Nothofagus*, *R. laetevirens* and *Drimys*) declined, including the thermophilous Myrtaceae.	Reversal toward cooler, and wetter climate. Lowlands of Isla Grande de Chiloé dominated by closed-canopy evergreen temperate rainforests composed by cold tolerant North Patagonian trees and epiphytic ferns (Hymenophyllaceae, *Polypodium feullei*).
.		Zone LL5 (949-890 cm depth)		12.9-11.6	Dominated by *P. nubigena*-*Nothofagus*-Myrtaceae. 50% drop of *P. nubigena* by 11.7 cal kyr BP. Myrtaceae, *Hydrangea,* and *Tepualia stipularis* increased. All other terrestrial taxa below 4%. Microscopic CHAR peaks between 12.9-12.5. Peak in organic density in mid and deep sectors of the lake.	From 14.6-11.5 cal yr BP, reversal toward cooler and wetter conditions. Two phases: i) 14.6-12.7 largest decline in temperature and increase in precipitation. Higher level of the lake. ii) 12.7-11.5 cal yr BP, cold seasonally dry climate or high frequency of summer drought. Higher repre-sentation of *T. stipularis* and Myrtaceae indicative of a slight lowering in lake level.
Canal de la Puntilla and Lake Condorito (pollen and charcoal) [Moreno 2001]	40°56 S/72°54W (120 m a.s.l.). 41°45 S/73°07 W (100 m a.s.l.)		13-12.2		13-12.2 ^{14}C cal kyr BP trees, vines and forest ferns (*Nothofagus*-Myrtaceae, *W. trichosperma*). Expansion of *Podocarpus* at ~12.2 ^{14}C cal kyr BP and persistence of rainforest vegetation	Near modern conditions between ~13-12.2 1^{4}C kyr BP. Predominance of closed-canopy NPRF under temperate and humid conditions. At ~12.2 1^{4}C kyr BP onset of cooling.
			12.2-11.4		Transition from basal peat to gyttja. From ~11.4 ^{14}C cal kyr BP decline in thermophilous taxa and increase in hygrophilous NPRF taxa (*Podocarpus* and *Nothofagus*) persisting until 9.8 ^{14}C cal kyr BP (arboreal pollen 90%), suggesting similar conditions to modern climate at mid-to-high elevations in the mountain ranges 41° S. 11.2 ^{14}C kyr BP expansion of *Tepualia* and *Weinmania* (shade-intolerant emergent tree, long-lived pioneer species tolerant of infertile and poorly drained soils). Prominent increase in charcoal particles at ~11 ^{14}C kyr BP.	Reversal and two cooling events at 12.2 and 11.4^{14}C cal kyr BP. Cooling and increase in precipitation/effective moisture. Pollen assemblages between 11.4 and 9.8 ^{14}C kyr BP indicate change from a closed-canopy rainforest to woodland dominated by species favored by local disturbance by fire. High climate variability between ~11.2 and 9.9 ^{14}C kyr BP. warming starting at ~9.8 ^{14}C cal kyr BP. 11.2-9.8 ^{14}C cal kyr BP temperature was ~ 3° C below modern.
Lago Melli (Charcoal) [Abarzua 2008]	42°46 S/73°33 W (70 m a.s.l)			16-11	Establishment of a *W. trichosperma* woodland with Poaceae and the shrub *Ugni* sp. between 11.7-9.3 cal kyr BP. The expansion of *W. trichosperma* near-synchronous with fire activity, but ~1000 yr before Lago Condorito and Huelmo site.	Dominance of NPRF under cold and humid conditions. Likely, as a consequence of northward shift and/or intensification of the southern westerly winds. Max. fire occurrence between ~11-8.5 cal kyr BP.
Laguan Tahui [Abarzua 2004]	42°50'S/73°30' W (70 m a.s.l)	Zone Ta-1b (987–975 cm depth)	13.4-12.2	16-14.5	Expansion and diversification of closed-canopy rainforest by ~13.4 ^{14}C kyr BP. Pollen assemblage dominated by Myrtaceae–*N. dombeyi*-type–*Escallonia/Aextoxicon* (77% of pollen sum), along with *Lomatia/Gevuina*, Poaceae, *Empetrum* /Ericaceae, and *Donatia* (total representation of these taxa 5-2%). Peak abundance of the aquatic fern Isoetes (44%), and major decline of *N. dombeyi*-type (from 61% to 9%) and Blechnum-type (from 47% to 11%). *Amomyrtus*-type (Myrtaceae) reach max. representation at ~12.5 ^{14}C kyr BP	Low temperature, and high precipitation regime between 14-10 ^{14}C kyr BP
		Zone Ta-1c (975–960 cm depth)	12.2-11.2	14.5-13	Expansion of *S. conspicua*, *P. nubigena*, and *H. serratifolia* between ~12.2-10 ^{14}C kyr BP. Presence of Magellanic Moorland communities, and the aquatic fern *Isoetes savatieri*. Pollen assemblage dominated by Myrtaceae – *Escallonia/Aextoxicon* – *Saxegothaea conspicua* (73% of representation) along with *Lomatia/Gevuina*, *Pseudopanax laetevirens*, *Hydrangea serratifolia*, and *Podocarpus nubigena*. Peak abundance of *Hymenophyllum* and *Lycopodium.* The hygrophilous *Isoetes* and *M. nummularia* reach peak abundance during this zone.	Low temperatures and high-precipitation regimes between ~14-10 ^{14}C kyr BP.
		Zone Ta-1d (960–938 cm depth)	11.2-10	13-11.5	Pollen assemblage dominated by *H. serratifolia*–Myrtaceae–*P. laetevirens* assemblage (63% of representation). Increase of *H. serratifolia* (2% to 30%), *Laurelia* (2% to 6%), *Podocarpus nubigena*, the fern *Polypodium feullei*. Prominent decline of Myrtaceae (*Amomyrtus*-type, *Myrceugenia*-type, *M. nummularia*). Trace percentages of *Eucryphia/Caldcluvia*, *N. dombeyi*-type, *E. coccineum*, *D. winteri*, *Lomatia/Gevuina*, *Fuchsia*, *T. stipularis*. Expansion of *W. trichosperma* at ~10 ^{14}C kyr BP, and decline of NPRF taxa. The abrupt vegetation change coincides with a transition from lacustrine to boggy/swampy environments	~10 ^{14}C kyr BP possibly warmer and drier conditions and/or local disturbance regimens

REFERENCES

1 Firestone, R. B. *et al.* Evidence for an extraterrestrial impact 12,900 years ago that contributed to the megafaunal extinctions and the Younger Dryas cooling. *Proc Nat Acad Sci* **104**, 16016-16021 (2007).

2 Baker, D., Miranda, P. & Gibbs, K. in *Montana evidence for extra-terrestrial impact event that caused ice-age mammal die-off in Montana evidence for extra-terrestrial impact event that caused ice-age mammal die-off in AGU Spring Meeting Abstracts, abstract P41A-05.*

3 Fayek, M., Anovitz, L. M., Allard, L. F. & Hull, S. Framboidal iron oxide: Chondrite-like material from the black mat, Murray Springs, Arizona. *E&PSL* **319**, 251-258 (2012).

4 Ge, T., Courty, M. & Guichard, F. in *Field-Analytical approach of land-sea records for elucidating the Younger Dryas Boundary syndrome in AGU Fall Meeting Abstracts, abstract PP31D-1390.* (AGU).

5 Surovell, T. A. *et al.* An independent evaluation of the Younger Dryas extraterrestrial impact hypothesis. *Proc Nat Acad Sci* **106**, 18155-18158 (2009).

6 Laub, R. Observations from the Hiscock site (New York) bearing on a possible late-Pleistocene extraterrestrial impact event. *Curr Res Pleistoc* **27**, 168-171 (2010).

7 Mahaney, W. C. Evidence from the northwestern Venezuelan Andes for extraterrestrial impact: The black mat enigma. *Geomorphology* **116**, 48-57 (2010).

8 Mahaney, W. C., Krinsley, D. & Kalm, V. Evidence for a cosmogenic origin of fired glaciofluvial beds in the northwestern Andes: Correlation with experimentally heated quartz and feldspar. *Sediment Geol* **231**, 31-40 (2010).

9 Haynes, C. V. *et al.* The Murray Springs Clovis site, Pleistocene extinction, and the question of extraterrestrial impact. *Proc Nat Acad Sci* **107**, 4010-4015 (2010).

10 Pinter, N. *et al.* The Younger Dryas impact hypothesis: A requiem. *Earth Sci Rev* **106**, 247-264 (2011).

11 Wu, Y., Sharma, M., LeCompte, M. A., Demitroff, M. N. & Landis, J. D. Origin and provenance of spherules and magnetic grains at the Younger Dryas boundary. *Proc Nat Acad Sci* **110**, E3557-3566 (2013).

12 Pigati, J. S. *et al.* Accumulation of impact markers in desert wetlands and implications for the Younger Dryas impact hypothesis. *Proc Nat Acad Sci* **109**, 7208-7212 (2012).

13 Wright, F. W. & Hodge, P. W. Studies of particles for extraterrestrial origin: 4. Microscopic spherules from recent volcanic eruptions. *J Geophys Res* **70**, 3889-3898 (1965).

14 LeCompte, M. A. *et al.* Independent evaluation of conflicting microspherule results from different investigations of the Younger Dryas impact hypothesis. *Proc Nat Acad Sci* **109**, E2960-2969 (2012).

15 Holliday, V., Surovell, T. & Johnson, E. A blind test of the Younger Dryas impact hypothesis. *PloS One* **11**, e0155470 (2016).

16 Andronikov, A. V. *et al.* Implications from chemical, structural and mineralogical studies of magnetic microspherules from around the lower Younger Dryas boundary (New Mexico, USA). *Geogr Ann A* **98**, 39-59 (2016).

17 Luebert, F. & Pliscoff, P. *Sinopsis bioclimática y vegetacional de Chile*. 316 (Editorial Universitaria, 2006).

18 Schmithusen, J. Die raumliche Ordnung der chilenischen Vegetation. *Bonner Geogr Abh* **17** (1956).

19 Moreno, P. I., Jacobson, G. L., Lowell, T. V. & Denton, G. H. Interhemispheric climate links revealed by late-glacial cooling episode in southern Chile. *Nature* **409**, 804-808 (2001).

20 Di Castri, F. & Hajek, E. *Bioclimatología de Chile*. (Vicerrectora Acadmica, Universidad Catlica de Chile, 1976).

21 Denton, G. H. & Seno, D. Geomorphology, stratigraphy, and radiocarbon chronology of Llanquihue Drift in the area of the southern Lake , and Isla Grande de Chiloé, Chile. . *Geogr Ann A* **81**, 167-229 (1999).

22 Heusser, C. J., Heusser, L. E. & Lowell, T. V. Paleoecology of the southern Chilean Lake District-Isla Grande de Chiloé during middle-late Llanquihue glaciation and deglaciation. *Geogr Ann A* **81**, 231-284 (1999).

23 Villagrán, C. Un modelo de la historia de la vegetación de la Cordillera de La Costa de Chile central-sur: la hipótesis glacial de Darwin. *Rev Chil Hist Nat* **74**, 793-803 (2001).

24 Lamy, F. *et al.* Antarctic timing of surface water changes off Chile and Patagonian ice sheet response. *Science* **304**, 1959-1962 (2004).
25 Rojas, M., Moreno, P., Kageyama, M., Crucifix, M. & Hewitt, C. The Southern Westerlies during the last glacial maximum in PMIP2 simulations. *Clim Dyn* **32**, 525-548 (2009).
26 Moreno, P. I., Lowell, T. V., Jacobson Jr, G. L. & Denton, G. H. Abrupt vegetation and climate changes during the last glacial maximumand last termination in the chilean lake district: a case study from canal de la puntilla (41° s). *J Quat Sci* **81**, 285-311 (1999).
27 Villagrán, C. Late quaternary vegetation of southern Isla Grande de Chiloé, Chile. . *Quat Res* **29**, 294-306 (1988).
28 Villagrán, C. Expansion of Magellanic moorland during the late Pleistocene: palynological evidence from northern Isla de Chiloe, Chile. . *Quat Res* **30**, 304-314 (1988).
29 Labarca, R., Recabarren, O. P., Canales-Brellenthin, P. & Pino, M. The gomphotheres (proboscidea: Gomphotheriidae) from Pilauco site: Scavenging evidence in the Late Pleistocene of the Chilean Patagonia. *Quat Int* **352**, 75-84 (2014).
30 Moreno, P. I., Abarzúa, A. M. & Villagrán, C. Deglacial and postglacial climate history in east-central Isla Grande de Chiloé, southern Chile (43°S). *Quat Res* **62**, 49-59 (2004).
31 Hajdas, I., Bonani, G., Moreno, P. I. & Ariztegui, D. Precise radiocarbon dating of Late-Glacial cooling in mid-latitude South America. *Quat Res* **59**, 70-78 (2003).
32 Pesce, O. & Moreno, P. Vegetation, fire and climate change in central-east Isla Grande de Chiloé (43 S) since the Last Glacial Maximum, northwestern Patagonia. *Quat Sci Rev* **90**, 143-157 (2014).
33 Jara, I. A. & Moreno, P. I. Climatic and disturbance influences on the temperate rainforests of northwestern Patagonia (40° S) since∼ 14,500 cal yr BP. *Quat Sci Rev* **90**, 217-228 (2014).
34 Moreno, P. I. *et al.* Radiocarbon chronology of the last glacial maximum and its termination in northwestern Patagonia. *Quat Sci Rev* **122**, 233-249 (2015).
35 Moreno, P. I. & Videla, J. Centennial and millennial-scale hydroclimate changes in northwestern Patagonia since 16,000 yr BP. *Quat Sci Rev* **149**, 326-337 (2016).
36 Abarzúa, A. M. & Moreno, P. I. Changing fire regimes in the temperate rainforest region of southern Chile over the last 16,000 yr. *Quat Res* **69**, 62-71 (2008).
37 Schilling, D. H. & Hollin, J. T. in *Numerical reconstructions of valley glaciers and small ice caps in The Last Great Ice Sheets.* Vol. 207 220 (Wiley, 1981).
38 Villagrán, C. Análisis palinológico de los cambios vegetacionales durante el Tardiglacial y Postglacial en Chiloé, Chile. *Rev Chil Hist Nat* **58**, 57-69 (1985).
39 Moreno, P. I. & León, A. L. Abrupt vegetation changes during the last glacial to Holocene transition in mid-latitude South America. *J Quat Sci* **18**, 787-800 (2003).
40 Ariztegui, D., Bianchi, M. M., Masaferro, J., Lafargue, E. & Niessen, F. Interhemispheric synchrony of Late-glacial climatic instability as recorded in proglacial Lake Mascardi, Argentina. . *J Quat Sci* **12**, 333-338 (1997).
41 Ashworth, A. C. & Markgraf, V. Climate of the Chilean channels between 000 to 10,000 yr BP based on fossil beetle and pollen analyses *Rev Chil Hist Nat* **62**, 61-74 (1989).
42 Moreno, P. I. Climate, Fire, and Vegetation between About 13,000 and 9200 14 C yr B.P. in the Chilean Lake District. *Quat Res* **54**, 81-89 (2000).
43 Heusser, C. J. Late-glacial-Holocene climate of the Lake District of Chile. *Quat Res* **22**, 77-90 (1984).
44 Batist, M. D., Fagel, N., Loutre, M. & Chapron, E. A 17,900-year multi-proxy lacustrine record of Lago Puyehue (Chilean Lake District): introduction. . *J Paleolimnol* **39**, 151-161 (2008).
45 Vargas-Ramirez, L., Roche, E., Gerrienne, P. & Hooghiemstra, H. A pollen-based record of late glacial-Holocene climatic variability in the southern Lake District, Chile. *J Paleolimnol* **39**, 197-217 (2008).
46 Pino, M., Chávez-Hoffmeister, M., Navarro-Harris, X. & Labarca, R. The late Pleistocene Pilauco site, Osorno, south-central Chile. *Quat Int* **299**, 3-12 (2013).
47 Pino, M., Martel-Cea, A., Vega, R., Fritte, D. & Soto-Bollmann, K. in *Geología y geomorfología del sitio Pilauco in El Sitio Pilauco. Osorno, Patagonia Noroccidental de Chile.* 12-46 (Universidad Austral de Chile Valdivia, Chile, 2016).

48 Tello, F., Elgueta, M., Torres, F. & Pino, M. Abarzúa, A. M., Fossil beetles from Pilauco, south-central Chile: An Upper Pleistocene paleoenvironmental reconstruction. *Quat Int* **449**, 58-66 (2017).
49 Bryan, A. L. & Gruhn, R. Some difficulties in modeling the original peopling of the Americas. *Quat Int* **109**, 175-179 (2003).
50 Gnecco, C. & Aceituno, J. Poblamiento temprano y espacios antropogénicos en el norte de Suramérica. *Complutum* **15**, 151-164 (2004).
51 Mazz, J. M. L. Early human occupation of Uruguay: Radiocarbon database and archaeological implications. *Quat Int* **301**, 94-103 (2013).
52 Nami, H. G. Archaelogy, Paleoindian Research and Lithic Technology in the Middle Negro River, Central Uruguay. *Archaeological Discovery* **1**, 1-22 (2013).
53 Boëda, E. *et al.* The late-Pleistocene industries of Piauí, Brazil: new data. *Paleoamerican Odyssey*, 445-465 (2013).
54 Dillehay, T. D. Entangled knowledge: Old trends and new thoughts in first South American studies. *Paleoamerican odyssey*, 377-395 (2013).
55 Aceituno, F. J., Loaiza, N., Delgado-Burbano, M. E. & Barrientos, G. The initial human settlement of Northwest South America during the Pleistocene/Holocene transition: Synthesis and perspectives. *Quat Int* **301**, 23-33 (2013).
56 Schulte, P. *et al.* The Chicxulub asteroid impact and mass extinction at the Cretaceous-Paleogene boundary. *Science* **327**, 1214-1218 (2010).
57 Schultz, Zarate, Hames, Camilion & King. A 3.3-Ma impact in argentina and possible consequences. *Science* **282**, 2061-2063 (1998).
58 Vizcaíno, S. F., Fariña, R. A., Zárate, M. A., Bargo, M. S. & Schultz, P. Palaeoecological implications of the mid-Pliocene faunal turnover in the Pampean Region (Argentina). *Palaeogeogr Palaeoclimatol Palaeoecol* **213**, 101-113 (2004).